8-2022

Hierarchically Structured Photoelectrodes via Atomic Layer Deposition

Justin Rowan Reed DeMoulpied
University of Arkansas, Fayetteville

Hierarchically Structured Photoelectrodes via Atomic Layer Deposition

A dissertation submitted in partial fulfillment
of the requirements for the degree of
Doctor of Philosophy in Chemistry

by

Justin Rowan Reed DeMoulpied
University of Arkansas
Bachelor of Science in Biology and Chemistry/Biochemistry, 2015

August 2022
University of Arkansas

This dissertation is approved for recommendation to the Graduate Council

_____
Robert H. Coridan, Ph.D.
Dissertation Director

_____
Jingyi Chen, Ph.D.
Committee Member

_____
Colin Heyes, Ph.D.
Committee Member

_____
Stefan Kilyanek, Ph.D.
Committee Member

_____
Julie Stenken, Ph.D.
Committee Member

Abstract

In the search for a sustainable method to meet increasing energy needs, solar energy emerges as an underutilized, plentiful resource. Solar intermittency and requirements for transportation necessitate storing solar energy in the form of chemical bonds via artificial photosynthesis. Photoelectrochemical (PEC) water splitting generates hydrogen fuel from solar energy and water. A semiconducting material that successfully meets the complex requirements for building an industrially scalable PEC device has yet to emerge. This is leading to a reevaluation of materials previously overlooked within PEC research, mainly materials with limitations such as minimal charge carrier mobility and propensity to corrosion under illumination in aqueous environments. Cupric oxide (CuO) is one such candidate semiconductor, energetically suitable as a photocathode for PEC water splitting, and possesses both limitations mentioned above. Hierarchical three-dimensional structuring can circumvent the charge mobility limitations of CuO while maintaining its ability to absorb maximal incident solar illumination. Our proposed method of hierarchical structuring is coating nanometer-thick layers of CuO across a three-dimensional conductive scaffold of silica spheres, which maintains the path length of illumination through the semiconductor. Atomic Layer Deposition (ALD) can be used throughout construction of a PEC device based on this scaffold. In this work, the transparent conducting oxide (TCO) Al:ZnO (AZO) deposited using ALD is proposed as a conductive layer in hierarchical structuring of a PEC device. AZO is soluble in the extreme pH environments often present in current PEC water splitting research. An ultra-thin film of ALD-TiO_2 is evaluated as a protection layer for AZO from chemical dissolution. This protection layer work is further applied to intervening in CuO photocorrosion. Additionally, we studied the impact the work function of a back contact in the PEC performance of protected CuO electrodes. We conclude with a discussion on the viability of CuO as a material for three-dimensional structuring in the proposed scaffold.

Acknowledgements

I first give my unending thanks to my husband, Jason, for his patience during the last five hard years, even while he was also completing his dissertation. I cannot properly put into words the positive impact he has upon me daily, whether corralling my wandering thoughts, encouraging me to keep going, and soothing my anxieties. Thank you from the bottom of my heart for the love, family, home, and my last name. My dogs, Druzy and Rose, calmed me with cuddles and kept me company through the late nights, while encouraging me to take breaks to play when it was needed. I give thanks to the people around me that I call family that have been influential in keeping me here and positively shaping me as the person I am today: Mom, Dad, Harrison, Chris, Jordan, Alia, Corey, Grace, Linda, Freeman, and little Joshua. To my Dungeons and Dragons parties and comrades, you have provided relaxation and escape that have brought me unending joy throughout the oft bleak reality of graduate school.

To my lab mates who also became my friends, the sense of camaraderie and joy brought to the lab, even when science seemed to fail that day, kept me trying and moving forward. And finally, to Rob: you have been a blessing to have a boss. I would not still be here with a man less patient and kind than you are. Through the trials and tribulations of two floods, a plague, constant current historical events, and my own unique circumstances, you have been resilient, understanding, and a great mentor. May you be able to have a brief break after your first batch of students have spread their wings to their next opportunities knowing that you have made a substantial impact in our lives.

Table of Contents

List of Figures

List of Tables

List of Published Papers

Reed, P. J.; Mehrabi, H.; Schichtl, Z. G.; Coridan, R. H., Enhanced Electrochemical Stability of TiO2-Protected, Al-doped ZnO Transparent Conducting Oxide Synthesized by Atomic Layer Deposition. *ACS applied materials & interfaces* **2018,** *10* (50), 43691-43698.

Chapter 1. Introduction

1.1 Motivations

The rate of energy consumed by humanity continues to rise, with current models predicting the current rate of 19TW will rise to over 24TW by 2040; an increase largely driven by the modernization of emerging economies.[1,2] Fossil fuel combustion as an energy source cannot meet this increased demand due to finite limitations of supply and the environmental impact that will cause irreversible damage to the planet.[3] The energy of sunlight incident to the planet's surface is nearly 90,000TW; assuming complete collection and conversion into consumable energy. Accounting for technical and spatial limitations, primarily collection efficiency and land allocation, solar electricity can still theoretically provide over 7,000TW at peak production.[4]

Barring a world-wide electrical network, solar energy generation is intermittent due to earth's rotation. Peak energy demand (that occurs in the evening and night) does not correspond with peak energy generation from sunlight (mid-day).[5] Additionally, transportation undeniably requires storable energy sources. Batteries are the most familiar modern method of storing electrical energy, utilized in small electronics and hybrid cars. However, batteries suffer from low energy density both by mass and volume; to utilize them for storage on the scale of a commercial electrical grid would require insurmountable quantities of expensive, limited, and environmentally harmful materials.[6] The conversion of solar energy into chemical fuels is not a novel concept; photosynthetic bacteria and plants have arguably mastered the process.[3] Light absorption excites electrons within complex photosystems which are then quickly transported away from the source of the excitation, preventing loss of energy due to recombination. The high energy electron catalyzes unfavorable reactions that store energy,

eventually leading to the fixation of carbon in the atmosphere into the form of carbohydrates.

Utilizing biomass as a direct fuel source is a carbon-neutral process ideally. Typical species of plants convert 3.5-4.3% of incident solar energy into fuel for the organism.[7] Much of this absorbed light is utilized for plant and root growth. Even when using energy dense plants such as sugar cane, processing plant matter into biofuels such as ethanol results in a solar-to-fuel conversion efficiency of around 0.3%. Due to the processing necessary to convert biomass into ethanol or long-chain carbons for use in vehicles, the carbon cycle becomes far from neutral, though the impact on CO_2 emissions is less than a comparable quantity of fossil fuels.[8]

1.2 Proposed Solution

Inspired by the biological model of photosynthesis, materials scientist and chemists attempt to improve on evolutionary design. Employing photocatalytic semiconductor metal oxides to produce directly collectable and usable fuels from sunlight is known as artificial photosynthesis (AP).[3] Water splitting to generate H_2 (HER) and reduction of CO_2 (Carbon fixation) to methanol are both feasible paths for AP to replace fuels.[9-11] Materials that convert sunlight to fuels with efficiencies greater than 10% are considered to be the industrially viable benchmark, set by the US Department of Energy.[12] Engineering the structure and layering of materials to reach this benchmark is the driving force behind the research presented in this dissertation. Externalities of input must be considered for realistic designs, including material cost and abundance, energy consumed in fabrication, and scalability of fabrication. Beyond initial manufacture, any device must have a lifetime on the order of years or decades, be stable in structure and conversion efficiency, and materials used should have little to no

impact upon the environment upon degradation and disposal at the end of the device's lifetime.

Materials that meet these high demands have yet to emerge, leading to reconsideration of metal oxides with limitations that could be avoided by three-dimensional structuring. CuO (tenorite, copper(II) oxide, cupric oxide) is an earth abundant semiconductor, with the capability to absorb a large portion of the energy of the solar spectrum. However, this material faces a unique challenge: the material must be several hundred nanometers think to absorb all the incident light possible, but energy from electron excitation due to light is lost to recombination within a few nanometers of generation. To use this material for AP, it paradoxically needs to simultaneously behave like a thick-film light absorber but a thin-film electronic material.

The proposed solution to the paradox relies on 3-dimensional structuring. A scaffold of silica spheres with diameter of 100-300nm is self-assembled in a colloidal crystal with polystyrene spheres (PS) with diameter of 1-2μm. Atomic layer deposition (ALD) is employed to selectively bind the silica spheres together and upon removal of the PS an ordered guest-host lattice is formed.[13] Thin layers (10-100nm) of a transparent conducting oxide (TCO) is coated over the scaffold utilizing ALD, followed by deposition of the semiconducting photoabsorber (Figure 1.1). Therefore, an excited charge carrier is required to only travel a few nanometers to either the surface, to catalyze chemical reactions, or to the conductive backing, to freely move to a counter-electrode. Simultaneously a scaffold of this structure ensures the incoming photons travel through the necessary several microns of photoactive layer needed to be completely absorbed. Additionally, the scaffold advantageously utilizes silica spheres with tunable size for scattering light, the 3-D structure greatly increases surface area available for catalysis, and the holes in the lattice left by PS are tunable limit mass-transfer within the tortuous structure.[14-19] These tunable scaffolds hypothetically are

promising for storing solar energy as chemical bonds; the focus of this work was to develop methods toward the construction of such a device.

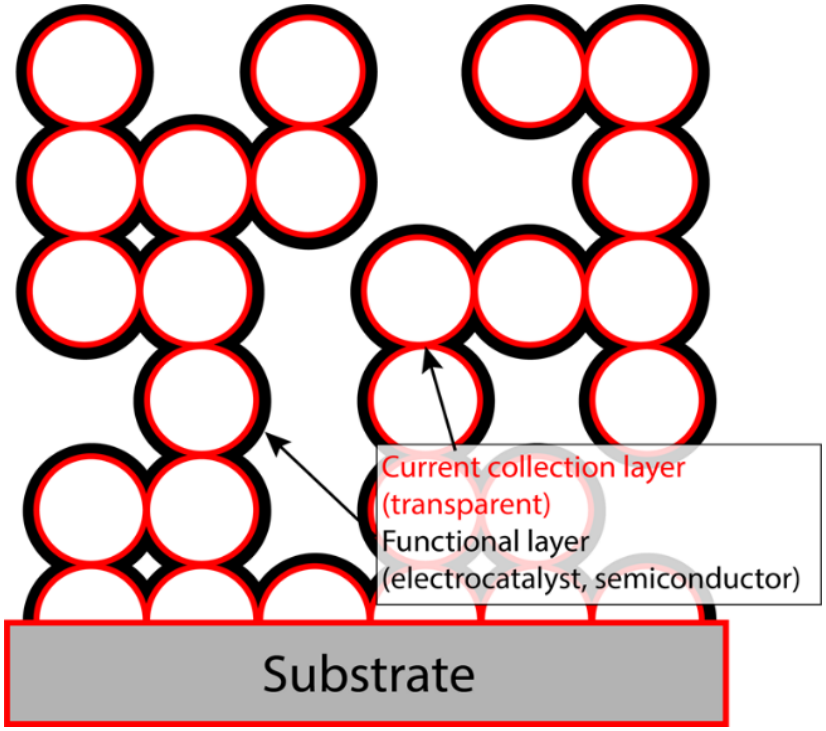

Figure 1.1 Hierarchical Structuring of Semiconductors. Scaffold of Silica beads (white) on a conductive substrate (grey) allows for deposition of a transparent conducting oxide (red) and an ultra-thin layer of a light collector (black). This allows for the decoupling of the absorption length and the minority carrier diffusion length.

1.3 Atomic Layer Deposition

Atomic layer deposition is a chemical vapor deposition technique developed in the 1970's that is used to create conformal, thin films, even in tortuous structures, with predictable and controllable layer thicknesses of the deposited material to the nanometer or angstrom scale.[20] Two complimentary reactions between an oxidizer, often water vapor, and organometallic precursors sequentially pulsed into the reaction chamber builds the film one atomic layer at time, in a self-limiting nature due to finite reaction centers on the film

(Figure 1.2). The organometallic precursor selectively binds to hydroxide functional groups present on the substrate forming covalently bound monolayers. The reaction chambers are generally under a light vacuum (0.1-1 Torr) and are temperature controlled, with most ALD reactions taking place at 150-250°C, though some precursor can deposit films at significantly lower temperatures. Ideally each cycle of the reaction fully coats all active sites, but due to the reality of kinetics experimentally fewer than half of the active sites react. The oxidizer species in ALD can be adjusted to make oxides, nitrides, sulfides, and metals.[20] The library of ALD precursors and recipes is constantly expanding, making ALD a powerful tool in deposition of thin films within the proposed hierarchical structure.

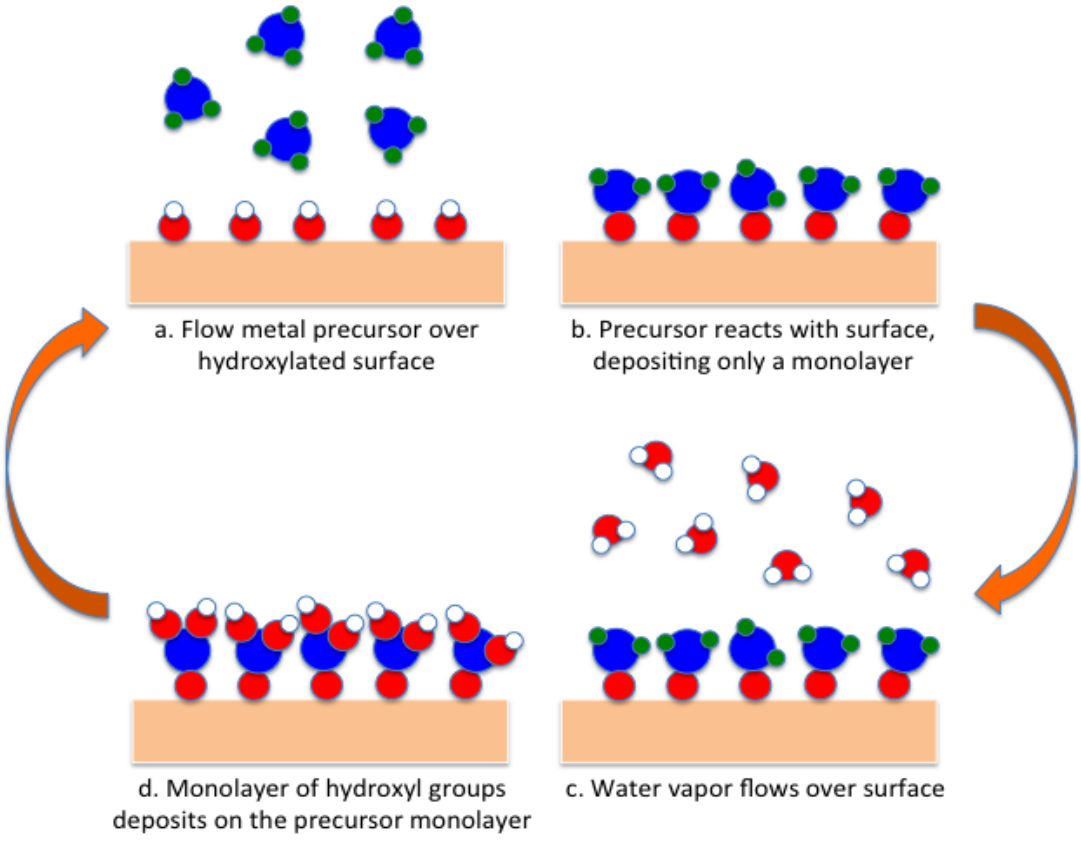

Figure 1.2. Schematic of Atomic Layer Deposition Reaction Sequence. A. Organometallic precursors pumped into chamber. B. Organometallic precursors react with all exposed hydroxylated surfaces, unreacted precursors removed. C. Water vapor pumped into chamber. D. Water reacts with exposed metal centers, reforming hydroxylated surface, and excess water is removed. This cycle is repeated until the desired thickness is reached.

The surface-specific nature of ALD reactions, with organometallic precursors often only binding to hydroxide functional groups present on a surface, is advantageous to the construction of the proposed scaffold. The deposition will take place on the silica spheres, as their surface is terminated with hydroxide functional groups, while not depositing upon the polystyrene. In this manner, ALD is utilized to bind the silica scaffold before the removal of polystyrene and subsequent functionalization.

1.4 Solid-State Physics of Semiconductors

In a solid crystal, the electronic orbital energy levels that are initially discrete for a single atom or molecule interact amongst themselves, to form continuous bands of available energy states, as prescribed by band theory. Metals are materials whose highest occupied molecular orbitals (HOMO) and lowest unoccupied molecular orbitals (LUMO) overlap, thus the frontier valence band is partially filled, and electrons can move freely through the band making the material conductive. In both a semiconductor and an insulator, the HOMO band is fully filled and is designated the valence band (VB), while the LUMO is empty and designated the conduction band (CB). The energy difference between the upper edge of the VB and the lower edge of the CV is defined as the band gap (E_g). A semiconductor is a material that is only conductive at high temperatures or when a voltage is applied across the material, generally defined as a E_g of less the 4.0eV (Figure 1.3).[21]

A photon can interact with a semiconductor to form an excited electron and an electron hole. These high energy excitons can be used to catalyze chemical reactions once the electron is separated from its hole. The band gap of a material defines the minimum energy a photon must possess to excite an electron within the crystal. Materials with a smaller bandgap will be able to absorb a larger fraction of the solar spectrum; each photon with the minimum energy or higher will be converted into one excited, mobile electron. Excess energy in the photon beyond necessary E_g is lost to thermal relaxation in a few

femtoseconds; to completely transform the solar energy to chemical bonds, the wavelength of light would be exactly the band gap and no smaller, though this is entirely impractical. The Shockley-Queisser limit defines the maximum energy efficiency of solar conversion, at a band gap of 1.34eV, where the device could have a theoretical solar conversion efficiency of 33.7%.[22] The band gap is indicative only of the relative positions of the CB and VB, not their absolute energies; which is crucial information that determines its ability to drive reactions forward. Additionally, small band gap semiconductors that approach the Shockley-Queisser limit are generally less stable in any solution used for photoelectrochemistry, imposing a frequent tradeoff between device lifetime and device efficiency.

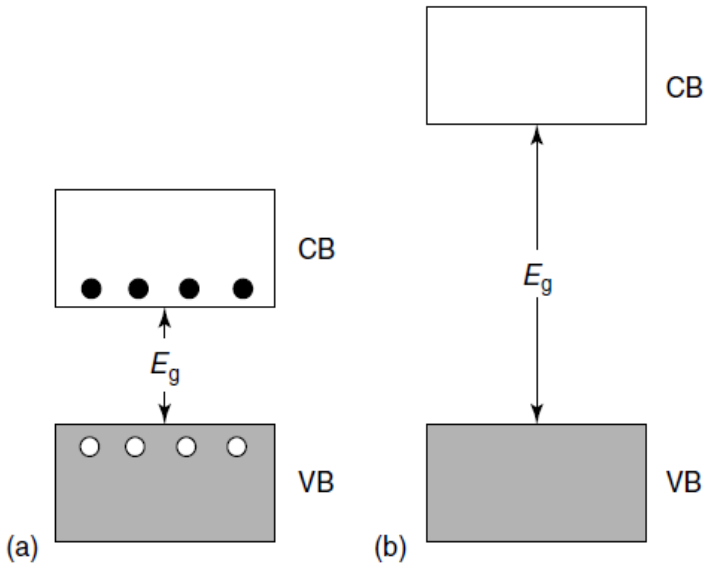

Figure 1.3. Semiconductor and Insulator Bang Gap. In both a semiconductor (a) and an insulator (b), the fully filled valence band (VB) and the empty conduction band (CB), are separated by an energy gap called the optical band gap (E_g). A band gap of less than 4eV makes the material a semiconductor, values much greater than 4eV are insulating materials. Semiconductors can have electrons excited to the CB at high temperatures or an applied voltage.

The Fermi level of a material is an intrinsic thermodynamic quantity (often abbreviated as E_f or ε_f). It is the electrochemical potential of electrons in the material. In a metallic material, it is more commonly referred to as the work function of the metal. A semiconductor has a Fermi energy level within the band gap of the semiconductor, between the valence band and conduction band. Should the Fermi energy be directly in the middle of the conduction band edge and the valence band edge, the semiconductor is intrinsically

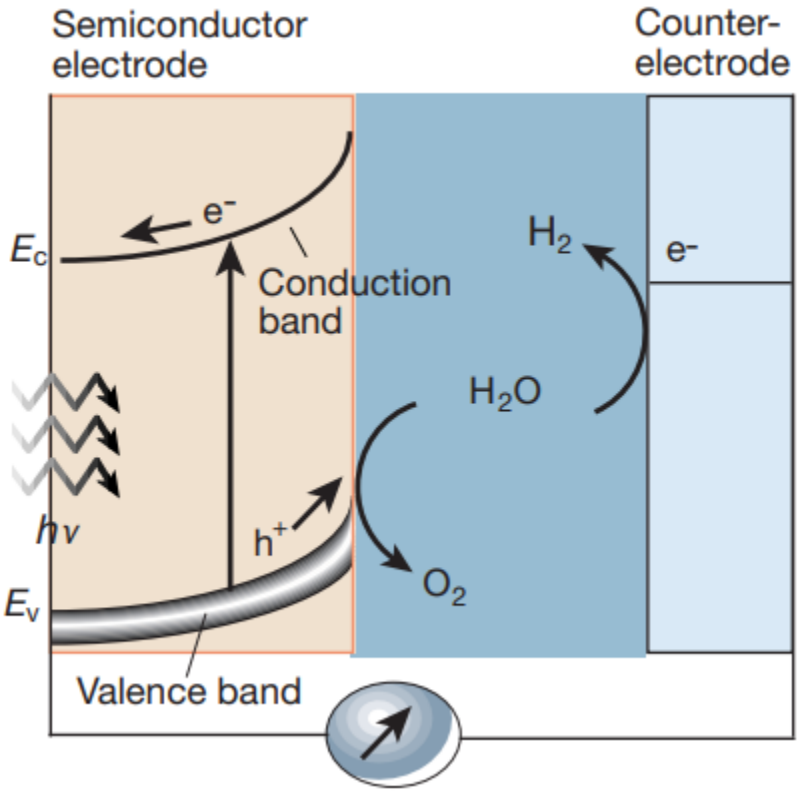

Figure 1.4 Semiconductor-Solution Interface. An n-type semiconductor working electrode in solution. The electrochemical potential of the solution is lower than the fermi energy of the semiconductor. Because of charge transfer equilibration, an electric field is generated in the semiconductor, in a phenomenon known as band bending. Photoexcited electron-hole pairs are separated, with holes going to the surface to oxidize water, while electrons are transported to the counter electrode to reduce hydrogen. A p-type semiconductor behaves in an analogous manner, with a reverse electric field pushing electrons to the surface and holes to the counter electrode.

undoped. Through the addition of electron-poor atoms or through intrinsic electron deficiencies in the crystal structure of the solid, the Fermi level will be closer to the valence band edge, and the semiconductor is considered p-type. A Fermi energy level that is closer to the conduction band edge due to excess electrons is considered n-type.

When an interface between a semiconductor and solution is formed, the fermi energy of the semiconductor at the surface equilibrates with the electrochemical potential of the solution. This causes a collection of excess charge near the surface of the semiconductor, effecting the position of the VB and CB edge; a phenomenon known as band bending (Figure 1.4).[23] Band bending in a semiconductor induces charge separation of photogenerated high energy electron-hole pairs, due to the resulting electric field. When electrons are accelerated toward the surface, in the case of a p-type semiconductor, the electrode is a photocathode; an n-type semiconductor forms a photoanode in a similar manner. An analogous junction can form between solid metal and a semiconductor if there is a difference between their Fermi energies. Again, the fermi energy of the semiconductor equilibrates with the work function of the metal by charge transfer, which induces band bending in the resulting electric field. Both interfaces are referred to as a Schottky junctions. If the electrochemical difference between the materials is small, the contact is considered Ohmic: electrons and holes can flow unimpeded through the junction regardless of direction.

The work function of the metal in a back contact defines the electrical potential the semiconductor will equilibrate to. The depth of the workfunction for the back contact is just as important to consider when constructing photoelectrodes as the choice of semiconductor. Workfunctions are generally reported as negative values based the energy needed to remove an electron from the material to vacuum. A shallow or more positive workfunction metal when in contact with an n-type semiconductor will induce band bending that pulls electrons to the back contact, while pushing holes to toward the solution-semiconductor interface,

which is advantageous for a photoanode (Figure 1.5a). Similar band bending is detrimental to a p-type semiconductor, as hole are trapped in the semiconductor, which will greatly increase recombination (Figure 1.5b). High energy electrons used for reduction on the semiconductor surface are pulled away from the reaction center and energetically lost to recombination from excess holes.

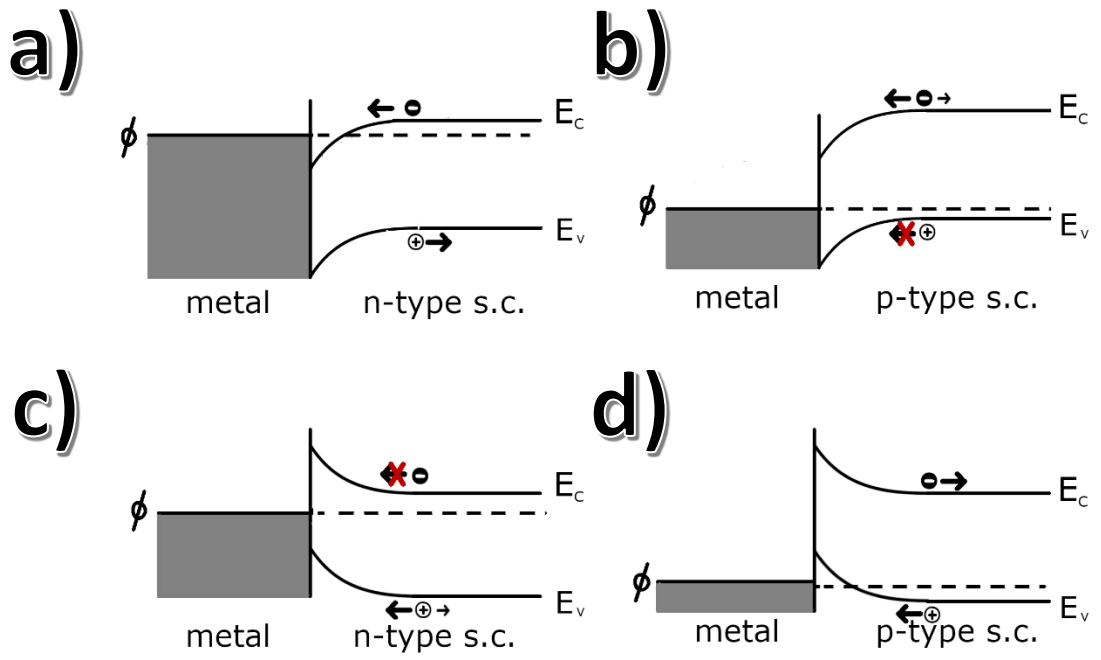

Figure 1.5 Back Contact Workfunction Effect on Electric Field in a Semiconductor. Schematic of band bending at a semiconductor-back contact interface. The workfunction of the metal is denoted by Φ, the valence band edge by E_V, the conduction band edge by E_C, and electrons and holes represented as negative and positive charges, respectively. A back contact current collector with a shallow or more positive workfunction is advantageous to the anodic potential of a n-type semiconductor (a). The same current collector will be detrimental to a p-type semiconductor's performance as a photocathode (b) by creating a hole-trapping electric field, increasing recombination events. A deep or more negative workfunction current collector creates analogous electron trap states in n-type semiconductors (c), while advantageously encouraging charge separation in a p-type semiconductor (d).

Inversely, a deep or more negative workfunction metal is detrimental to n-type semiconductor photoanodes by creating an electron trapping electric field, again increasing recombination (Figure 1.5c). The same deep workfunction is advantageous to a p-type

photocathode, forming a charge-separating electric field, encouraging electrons to travel toward the surface while pulling holes through to the counter electrode (Figure 1.5d). Based on these principles, for the innate p-type semiconductor CuO, deeper back contact workfunctions increase the solar conversion efficiency of a constructed photocathode by reducing the rate of recombination events. This is especially crucial in a Mott Insulator such a CuO. Without an appropriate electric field, charge carriers will not travel far by diffusion.

1.5 Overview

Chapter 2 begins with providing literature evidence for the viability and necessary considerations when constructing a PEC device for water splitting. A brief history of ALD is reviewed, followed by some applications and current direction in the field. The use ALD in protection layers, specifically for PEC devices, is also addressed. In chapter 3, work on ALD protection layers begins. A study of ALD-TiO_2 and its efficacy as a protection layer of Al:ZnO, a transparent conducting oxide typically unstable outside of near-neutral pH. Mechanisms of failure were observed in pinhole aberrations in TiO_2 deposition.

An extensive study of CuO as a photocathode is shown in Chapter 4, examining photocorrosion and the choice of back contact influencing device performance. Protection layers via ALD are examined as a potential solution for the problem of photocorrosion. In a CuO photocathode, various conductive back contacts are compared, based on the hypothesis the work function of the current collector will influence the performance of a CuO photocathode. The common transparent conducting oxide F:SnO_2 (FTO), was compared to silver and nickel as the back contact via cyclic voltammetry under illumination. FTO and silver, both metallic materials with workfunctions significantly above the fermi energy of CuO, caused a CuO photocathode to demonstrate significantly lower photoeffects in current density than electrodes upon a Ni substrate, a metal with a workfunction nearly equal to the

fermi energy of CuO. Chapter 5 serves as a conclusion and outlook on future directions of this research.

Chapter 2. Literature Review

2.1 Photoelectrochemical Water Splitting

Solar energy conversion is motivated by the desire to mitigate intermittency of incident solar energy and to provide a sustainable alternative to fossil fuels. Hydrogen evolution from water is one of the proposed alternatives to fossil fuels, utilizing abundant sunlight and water.[24] First demonstrated by Fujishima and Honda in 1972 using TiO_2, PEC water splitting has emerged as a method for storing solar energy in chemical bonds.[25,26] To compete financially with hydrogen generation from natural gas, a minimum solar-to-hydrogen (STH) conversion efficiency of a PEC device needs to be maintained for several years.[27,28] Arguably more importantly, the energy output of a PEC device needs to significantly exceed the energy needed to construct it.[29,30]

Splitting a single molecule of water to H_2 and O_2 requires four electrons to be excited by photon absorption, each with enough energy to overcome thermodynamic losses and catalyze OER and HER.[31] A single light collection material to reasonably drive water splitting would need to have a minimum gap of 1.8eV, with appropriate band edge positions, to reach a theoretical STH of 23%.[32] Inspired by the Z-scheme of photosynthesis, which uses two photosystems to successively excite charge carriers, a tandem PEC system is needed to achieve water splitting with high STH conversion efficiencies.[7,33] An example two light collector system composed of materials with band gaps of 0.9eV and 1.6eV increases the STH efficiency to 32%; when using earth abundant catalysts is considered the STH drops to 28.7% (Figure 2.1).[32,33] The Hu et al. computational study additionally found there is no significant effect on STH when choosing between a separate photocathode and photoanode system or a tandem stacked absorber system (Figure 2.2).[33,34]

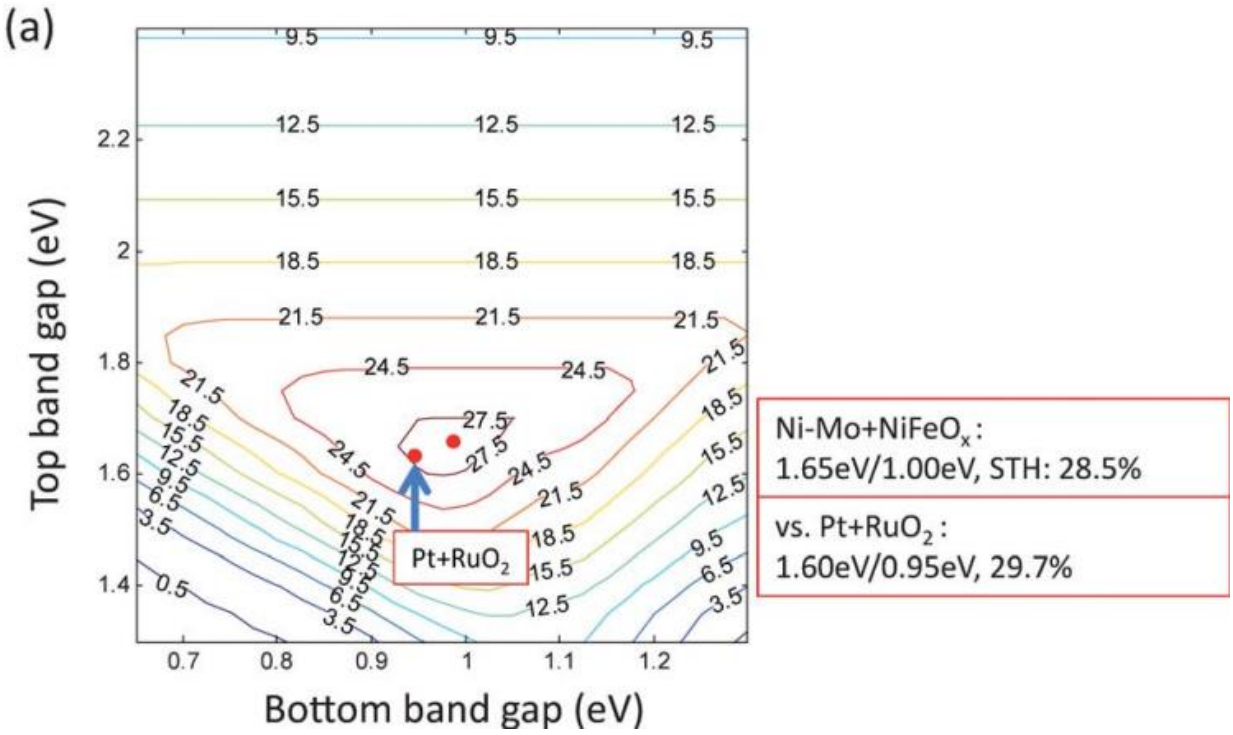

Figure 2.1 Solar-to-Hydrogen Efficiency of a Tandem PEC Device as a Function of Band Gap. The band gap of the semiconductor on top in a tandem should be wider that the band gap of the semiconductor beneath it. Maximal STH efficiency is theoretically found at a 1.6eV band gap for the top semiconductor and 0.95eV for the bottom when accounting for state-of-the-art catalysts for HER and OER (Pt and RuO_2). When using earth abundant catalysts, the maximal band gap is slightly higher for both layers, because of needing higher overpotentials to catalyze HER and OER.

Adapted with permission from Hu, S., et al., An analysis of the optimal band gaps of light absorbers in integrated tandem photoelectrochemical water-splitting systems. *Energy & Environmental Science* **2013, *6*, 2984-2993**; copyright RSC Publishing

A benchmark tandem photocathode of GaInP/GaInAs (with band gaps of 1.8eV and 1.2eV) in a PEC device reached a STH efficiency of 16%, up to 19% with the addition of several protection, separation, and catalytic layers.[35,36] These materials, though able to reach some of the highest STH efficiencies for a PEC device to date, are prohibitively expensive both monetarily and energetically to acquire and manufacture. Other III-V semiconductors such as GaN, GaP, GaAs, InP share similar drawbacks as the scarcity of indium and gallium make scaling these materials to industrial scale infeasible.[34] No photoanode system or material has emerged to meet the requirements of being high efficiency, low cost fabrication, and intrinsic stability.[26] Most n-type metal oxides have 2.5eV or larger band gaps that make efficient

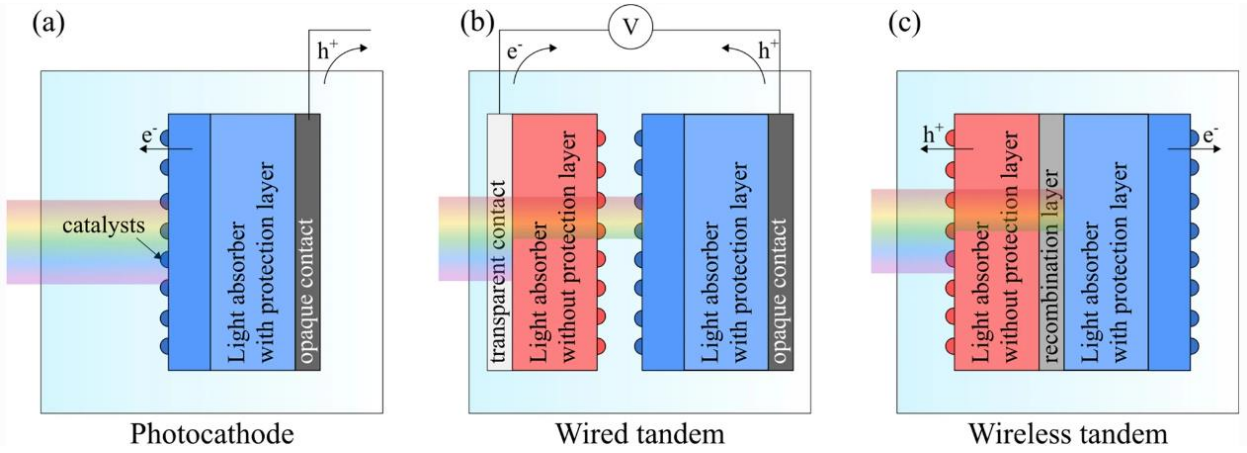

Figure 2.2 Structuring a Photoelectrochemical Device. A single photocathode (a) with a separate counter anode catalyst. A separated tandem PEC device (b) with a photoanode (red) and a photocathode (blue) connected by wiring. A type layered tandem PEC device (c) with a photoanode (red) and a photocathode (blue) layered in one electrode. Another type of layered device would have two light absorbers on a photoanode, with a catalyst on the cathode. Inversely, the two light absorbers would be on the photocathode, with only a catalyst on the anode. In all the tandem models, the illumination path passes through the two light absorbers sequentially. Thus, the large band gap semiconductor must be placed before the small band gap semiconductor in the illumination path.

Adapted from Moon, C., and Shin, B., Review on light absorbing materials for unassisted photoelectrochemical water splitting and systematic classifications of device architectures. *Discover Materials* **2022**, **2,** Article 5; Copyright Springer

capture of incident solar energy.[37] Hematite (α-Fe_2O_3) has been evaluated as an n-type candidate for PEC, with its band gap of 2.0eV, but is a Mott insulator: electron transport takes place via polaron hopping, resulting in photoexcited holes being lost to recombination within a few nm of generation.[38-40] The importance of band gap and band edge position in STH efficiency and limited earth abundant materials that meet those requirements, has resulted in a need for methods of enhancing the stability of semiconductors in aqueous solution.[37,41] Atomic Layer Deposition has emerged as a method for achieving this goal.[42]

2.2 Atomic Layer Deposition

Atomic layer deposition was first described in the west in 1980 under the name of atomic layer epitaxy, reporting the deposition of a ZnTe film.[43] The technique was also developed independently in the 1960s in the Soviet Union under the name molecular layering, though this history is less well known, primarily due to geopolitical isolation and a lack of translation. A concerted effort within the ALD research committee is underway to shed light on both origins of ALD.[44] The technique was renamed ALD as most films deposited were not epitaxial to their substrates and frequently amorphous films are desired in some electronic applications of ALD.[20]

Deposition of Al_2O_3 was documented as early as 1983 in patents describing ALD reaction chambers, though this chemistry relied on $AlCl_3$ as a precursor.[45] Additional reactions proposed in the patent included deposition of ZnS, SnO_2, GaP, and Ta_2O_5. Halide based precursors are the oldest ALD reactants, however they have the distinct disadvantage of forming gaseous strong acid as a byproduct, which can etch the reaction chamber and even etch the substrate of the film deposition. One instance of this etching phenomenon is seen in ALD of Ta_2O_5 films using $TaCl_5$ or TaI_5, especially when the dose of the precursor is not tightly controlled.[46,47]

Alkyl precursors are now primarily used as reactants, especially for aluminum and zinc films deposited from trimethylaluminum (TMA) and diethylzinc (DEZ).[48,49] These alkyl precursors are extremely reactive with water to form oxides, but have also been reported to form nitride, sulfide, and phosphide films with the appropriate oxidizing precursor.[49] The high reactivity of TMA and DEZ allow for deposition of films at low temperatures, necessary for applications on thermally fragile samples, such as organics, polymers, biologics, and perovskite solar cells, without significant decreases in deposition rates.[50-54]

The transparent conducting oxide Al:ZnO can be manufactured with ALD to provide a conductive film in tortuous structures. We can deposit AZO at temperatures below the melting point of the PS, present in the structural scaffold proposed previously, using TMA and DEZ.[55] It is well documented that there is a non-linear relationship between cycle ratio and final atomic ratio of dopants in ternary oxides deposited with ALD, due largely in part to the unequal binding energies of precursors to the surface.[54,56] Through adjusting recipe construction, the atomic ratio of dopants can be measured in relation to cycle ratio, which can be used to reliably predict future film composition.[54,57,58] Generally the Al doping percentage in ALD studies is reported based on the ratio of cycles of DEZ and TMA, not elemental analysis.[48] Nonetheless, doping ZnO ALD films with Al for 2-5% of cycles provides the lowest resistance in AZO films. Upon annealing of ALD AZO films in air at 350°C the film becomes resistive; annealing under Ar and N_2 at the same temperature still dramatically increases the resistivity of the film.[59] Annealing of AZO films DC sputtering annealed at the same temperature in air decreases resistivity of the film, as expected.[60] The cause of annealing negatively affecting AZO only when deposited with ALD is unknown.

ALD can also be used for the deposition of light absorbing semiconductors. CuO has been deposited at traditional ALD temperatures using copper (II) acetylacetonate and ozone.[61] Further research has shown bis-(dimethyl-2-propoxide) copper and ozone can be used to deposit CuO at 80°C.[62] Fe_2O_3 can also be deposited via ALD: traditionally ferrocene and ozone are used as precursors, but other amine-based iron precursors have been developed to varying success.[63,64] ALD films of Al_2O_3, TiO_2, and Ta_2O_5 have been deployed as protection layers for various applications, which will be discussed further below.[42] ALD has also been used to deposit other metal oxides including: SnO_2,[65-67] WO_3,[68-71] Co_2O_3,[72-74] and various vanadium oxides.[75-78] ALD can also be used to deposit unoxidized metals, often with the aid of plasma, including deposition of sporadic Pt nanoclusters.[79-81] The materials

mentioned here are by no means an exhaustive list of possible film depositions via ALD, with a plethora of new research developing precursors continuing at present.

2.3 Protection Layers for PEC with ALD

Thin protection layers are necessary to prevent dissolution of PEC materials from air or aqueous environments, while not impeding the photoactive properties of the protected material. Thus, materials used for protection layers in PEC need to have very wide band gaps to minimize parasitic absorption. Hematite has been protected with ALD-Ta_2O_5 to increase stability is extremely basic (pH=13) conditions, but depositing more than 2nm of the protection layer was found to decrease the conductivity of a PEC device.[82] Researchers protected a silicon photoanode from self-oxidation by the addition of ultra-thin layers of TiO_2, but thicknesses greater than 2nm of TiO_2 linearly increased the overpotential needed for water oxidation.[83] Stability of the silicon anodes was increased during CV sweeping, but no long-term stability experiment was performed during the study.

Parachhino et al. in 2011 revitalized interest in Cu_2O in PEC by significantly increasing device lifetime and limiting photocorrosion with ALD protection layers.[84] A film of 11nm of TiO_2 did not increase stability of electrodes unless 20nm buffer layer of ZnO was first deposited. The ZnO had to be doped with Al to increase stability without drastically reducing the conductivity of the electrode. At this point Cu_2O device lifetimes had been increases from a few seconds to about an hour before complete failure. Further work with this system determined increasing the deposition temperature of the TiO_2 layer to 200^{o}C, improving the stability of the protection layer, increased device lifetimes to 10-12 hours.[85]

The trend of protection layer thickness having a positive correlation with device lifetimes and a negative correlation with device conductivity and photocurrent density becomes apparent from the previously mentioned studies and across the literature.

Protection layers are often electronically insulating, the charge carriers generated in the semiconductor must tunnel through to catalytic sites at the solution interface. The likelihood of such tunneling events decreases as insulator thickness is increased past a few nanometers. Conversely, the likelihood of pinhole defects leading to device failure decreases as film thickness is increased into the 100nm range. Few studies have been done to identify the cause of ALD pinhole defects, though some methods for combating defects have been suggested.

To decrease pinhole defects in 2-10nm layers of Al_2O_3 on Ni substrates, Zhang et al. first deposited a 15nm ALD tungsten seed layer.[86] This approach encouraged effective nucleation to decrease the density of defects by 1000-fold. Instead of adding additional layers, Gertsch et al. used atomic layer etching to reduce defects in Al_2O_3. A 24nm of ALD Al_2O_3 was grown to allow holes to be filled as the film thickness increased, afterwhich the layer was etched back to the desired 5nm.[87] This approach halved the failure rate of the devices the researchers constructed, which were $Ag/Al_2O_3/Al$ capacitors. An investigation of TiO_2 protection layers on GaAs anodes showed a reduction in pinhole density if the entire deposition was performed in a cleanroom. However even 45nm ALD-TiO_2 films made in a cleanroom were not good enough to eliminate pinholes entirely, the thickness had to be increased to greater than 112nm.[88] Even with cleanroom conditions, there was still uneven deposition of the film, indicating that contamination is not the sole cause of defects in ALD.

Chapter 3. Enhanced Electrochemical Stability of TiO_2-Protected, Al-doped ZnO Transparent Conducting Oxide Synthesized by Atomic Layer Deposition

P. Justin Reed, Hamed Mehrabi, Zebulon G. Schichtl, and Robert H. Coridan*

Department of Chemistry and Biochemistry, University of Arkansas, 345 North Campus Drive, Fayetteville, Arkansas 72701, United States

Corresponding author: Robert H. Coridan; email: rcoridan@uark.edu

3.1 Abstract

Transparent, conductive coatings on porous, three-dimensional materials are often used as the current collector for photoelectrode designs in photoelectrochemical applications. These structures allow for improved light trapping and absorption in chemically-synthesized, photoactive overlayers while minimizing parasitic absorption in the current collecting layer. Atomic layer deposition (ALD) is particularly useful for fabricating transparent conducting oxides (TCOs) like Sn-doped In_2O_3 (ITO) and Al-doped ZnO (AZO) for structured materials because the deposition is specific to exposed surfaces. Unlike line-of-site deposition methods (evaporation, spray pyrolysis, sputtering), ALD can access the entire complex interface to make a conformal transparent conductive layer. While ITO and AZO can be grown by ALD, they are intrinsically soluble in the acidic and basic environments common for electrochemical applications like water splitting. To take advantage of the unique characteristics of ALD in these applications, is important to develop strategies for fabricating TCO layers with enhanced chemical stability. Ultra-thin coatings of stable materials can be used to protect otherwise unstable electrochemical interfaces while maintaining the desired function. Here, we describe experiments to characterize the chemical and electrochemical stability of ALD-deposited AZO TCO thin films protected by a 10nm TiO_2 overlayer. The addition of a TiO_2 protection layer is demonstrated to improve the chemical stability of AZO by orders of magnitude compared to unprotected, yet otherwise identically prepared AZO films. The electrochemical stability is enhanced accordingly in both acidic and basic environments. We demonstrate that TiO_2-protected AZO can be used as a TCO for both the cathodic hydrogen evolution (HER) and anodic water oxidation (OER) half-reactions of electrochemical water splitting in base and for HER in acid when the appropriate electrocatalysts are added. As a result, we show that ALD can be used to synthesize a

chemically stable TCO heterostructure, expanding the range of materials and electrochemical environments available for building complex photoelectrode architectures.

3.2 Introduction

Transparent conductive oxides (TCO) are wide band gap semiconductors that can be extrinsically doped to induce low resistivity while maintaining high optical transmissivity. They are important components for a wide range of optoelectronic technologies, including photovoltaics, photodiodes, touch screen interfaces, and light emitting diodes.[89,90] TCOs can also be used as a transparent electron or hole collection layer in complex, three-dimensional structured electrodes for water splitting electrolysis, CO_2 reduction, or other photoelectrochemical (PEC) applications. Hierarchically structured materials are often used for these applications to increase surface area, to generate dielectric contrast in structures engineered to improve light absorption via increased light trapping or optical resonances, or to decouple disparate functional length scales of the material in order to improve the effective properties of semiconductor photoelectrodes.[14-19] The use of a TCO in these structures minimizes efficiency losses due to parasitic absorption in the non-photoactive current collector layers. Common TCOs such as Sn-doped In_2O_3 (ITO), F-doped SnO_2 (FTO), and Al-doped ZnO (AZO) are used widely as conductive back contacts for chemically synthesized electrodes for use in dye-sensitized solar cells, chemically-synthesized photovoltaics, electrocatalysts, and multijunction semiconductor architectures.[91]

Atomic layer deposition (ALD) is a powerful method to synthesize conformal thin films in high-aspect ratio or complex, three-dimensional substrates.[20] The gas-phase precursors can diffuse through nanoscale porosity to react over the entire surface. Additionally, the self-limiting nature of ALD allows for precise film thickness and composition even in tortuous electrodes. In principle, ALD should be nearly ideal for depositing the TCO current collector

in a hierarchically structured photoelectrode. However, issues with each of the common TCO materials have prevented the ALD-derived films from general adoption for PEC applications. ALD precursors and recipes for the depositing ITO and AZO are readily available, but these oxides dissolve in the acidic or basic solutions that are desirable for many PEC applications.[16] FTO is generally more stable but is prepared by non-surface specific, line-of-sight methods like chemical vapor deposition or ultrasonic spray pyrolysis. To this point, we are not aware of any ALD routes for the synthesis of FTO, likely due to the corrosive and poisonous nature of fluorine precursors like HF or NH_3F.[92] Therefore, identifying a new strategy for preparing an ALD-derived, chemically stable TCO will improve the range of materials that can be integrated into hierarchically structured photoelectrodes and electrolyte conditions for their use.

One approach for protecting an electrochemical interface from corrosion is to coat it with an ultra-thin layer of a material that is chemically stable under the conditions of interest.[93] If the protection layer is sufficiently thin, it can still maintain the conductivity of the interface even if the coating material is nominally insulating as a bulk material. This is especially useful for protection of photoelectrodes from dissolving or passivating in the extremely acidic or basic electrolytes common for PEC water splitting applications. The strategy has been effective for protecting a variety of semiconductors with ALD-derived protection layers of MnOx,[94,95] TiO_2,[96-98] and Al_2O_3.[99-101] Ta_2O_5 thin films have been used to protect ZnO photoanodes for several hours in 0.1 M KOH.[102] ALD-derived ultra-thin (< 5 nm) layers of AZO/TiO_2 have been used as a protection layer for Cu_2O photocathodes.[84,85] The addition of ALD-derived TiO_2 layers have been identified as a useful protection for conventionally deposited FTO TCO electrodes in harsh electrochemical conditions.[103,104]

Here, we characterize the chemical and electrochemical stability of TiO_2-protected, ALD-deposited AZO TCO thin films. The addition of a TiO_2 protection layer can improve the

stability of ALD synthesized AZO thin films for virtually the entire pH range of interest for aqueous PEC applications. Specifically, we show that a 10 nm TiO_2 protection layer is capable of increasing the chemical stability of AZO by orders of magnitude compared to unprotected, yet otherwise identically prepared AZO films while maintaining low resistivity. We demonstrate that TiO_2-protected AZO is accordingly stable as a TCO for both the cathodic hydrogen evolution (HER) and anodic water oxidation (OER) half-reactions of electrochemical water splitting in 1 M NaOH and for HER in 1 N H_2SO_4 when decorated with the appropriate electrocatalysts. The result of this strategy is that a conformal and chemically stable TCO can be deposited via surface-specific chemical reactions rather than line-of-sight physical deposition methods. This expands the possible combinations of synthetic methods, materials, and electrochemical environments available for fabricating electrodes with complex, three-dimensional structures.

3.3 Experimental

3.3.1 Materials

Acetone (99.5%; EMD Millipore Corp), methanol (high-performance liquid chromatography (HPLC) grade; VWR Analytical), isopropanol (HPLC grade; VWR Analytical), and water (HPLC grade; VWR Analytical) were used as received. Sodium hydroxide (50%w/w; VWR Analytical) was diluted to 1 N aqueous solutions (pH 13.5), sulfuric acid (95-98%; VWR Analytical) was also diluted to 1 N (pH 0.5). A 1 N stock solution of aqueous hydrochloric acid was used as received (VWR Chemicals). Potassium hexachloroplatinate (IV) (≥99.99%, Sigma-Aldrich) was used as received.

n^+-Si wafers (As-doped, single-side polished, <0.001 Ω cm; Silicon Materials Inc.) were used as electrode substrates for electrochemical experiments. p-Si wafers with an insulating 300 nm wet thermal oxide (p-type, 0.01-0.02 Ω cm; University Wafer) were used for

measuring resistivity for ALD-deposited films. Si wafers were diced into 2 cm × 2 cm square substrates, then used as received. Plain, soda lime glass microscope slides (25 mm x 75 mm; VWR International LLC) were used as received.

3.3.2 Characterization Methods

Scanning electron microscopy (SEM) images were taken with a FEI Nova Nanolab SEM equipped with an energy-dispersive x-ray (EDX) spectrometer (Bruker XFlash 5010). X-ray photoelectron spectroscopy (XPS) measurements were performed on a PHI Versaprobe instrument with a monochromated Al Kα source (1486.6 eV). X-ray diffraction (XRD) measurements were taken using a Mini-Flex II by Rigaku using Cu-Kα radiation (λ = 1.54 Å). Resistivity measurements were performed using a Veeco 4-Point Resistivity Meter equipped with tungsten carbide tips (50 μm radius). Transmission UV-Vis spectroscopy was performed on a Jasco V-780 spectrometer equipped with an integrating sphere. All electrochemical measurements and electrodeposition procedures were performed using a potentiostat (BioLogic SP-50).

3.3.3 ALD Growth of Thin Films

ALD films were deposited on whole glass slides (25 mm x 75 mm), n^+-Si substrates, and thermal-oxide coated p-Si substrates. Prior to the ALD process, each substrate was cleaned by rinsing sequentially in acetone, methanol, and isopropanol followed by 30 minutes in UV-ozone cleaner. The underside of each glass slide substrate was masked from ALD growth by a layer of Kapton tape. Substrates were transferred into the ALD reaction chamber immediately after cleaning.

AZO thin films were synthesized from diethylzinc (abbreviated DEZ, 95%; Strem, Inc.), trimethylaluminum (TMA, 98%; Strem, Inc), and H_2O (HPLC grade; VWR Analytical) precursors in an atomic layer deposition reactor (GEMStar XT; Arradience, Inc.). Ultra-high purity N_2

(99.999%; Airgas) was used as the carrier gas in the reactor and controlled by an automated mass flow controller. Each AZO film described here was synthesized with the following ALD procedure. The substrate of interest was placed in the reaction chamber and held at 175 °C. Each cycle of the AZO process included sequential exposures to DEZ and H_2O precursors from room-temperature cylinders. Each DEZ exposure consisted of a precursor pulse (22 ms under 40 sccm N_2 carrier gas flow), a precursor soaking step to maximize the exposure of the high-aspect ratio substrates to the reactants (1 s, 40 sccm N_2 with the pump valve closed), and a purge step to evacuate the chamber of precursor (15 s, 100 sccm N_2). Each H_2O exposure consisted of a precursor pulse (22 ms, 40 sccm N_2), a soaking step (1 s, 40 sccm N_2 with the pump valve closed), and a purge step (15 s, 90 sccm N_2). After the deposition of 24 cycles of DEZ and H_2O, a single doping cycle was run following the same recipe, though replacing DEZ with TMA in the process. This sequence (24 cycles with DEZ, one cycle with TMA) was continued until the desired number of cycles was achieved.

The ALD synthesis of a protective layer of TiO_2 was at a reactor temperature of 150 °C. TiO_2 was synthesized using tetrakis(dimethylamido)titanium (TDMAT, 99%; Strem, Inc) and H_2O. The TDMAT precursor cylinder was heated to 80 °C during the process. The H_2O precursor cylinder was kept at room temperature. The mass flow control of the nitrogen carrier gas was set to 20 sccm for the entire deposition. Each cycle consisted of a precursor pulse of TDMAT (100 ms), a purge of 15 s, a H_2O exposure of 15 ms, and a second purge of 25 s. This sequence was repeated until desired number of cycles was reached.

3.3.4 Electrode Fabrication for Electrochemical Stability Experiments

Electrocatalytic cathodes for the hydrogen evolution reaction (HER) were prepared by the electrodeposition of Pt on ALD films prepared on n^+-Si substrates. The electrodeposition solution was a 1.0 mM potassium hexachloroplatinate (IV) in 0.1 M hydrochloric acid.[105] Each

electrodeposition was run for 10 minutes at a current density of 100 μA cm^{-2} in a three-electrode electrochemical cell with a platinum wire counter electrode and a Ag/AgCl (saturated KCl) reference electrode (Bioanalytical Systems, Inc.). Each electrodeposition was carried out in an electrochemical cell with the active area of the working electrode (1 cm^2) defined by a viton o-ring. n^+-Si wafers coated with ALD films were prepared for electrodeposition of platinum or electrochemical stability measurements by scribing the back of the substrate and applying a layer of conductive gallium-indium (Ga-In) eutectic (≥99.99%; Sigma-Aldrich).

Electrocatalytic anodes for the oxygen evolution reaction (OER) in 1 M NaOH were prepared by the electron-beam evaporation of Ni (99.995%; Kurt J. Lesker Co.) onto ALD films prepared on n^+-Si substrates. The deposition rate (0.1 Å s^{-1}) and total thickness were measured by a quartz crystal monitor in the evaporation chamber.

3.3.5 Chemical and Electrochemical Stability Characterization

Samples for stability experiments were cut from whole glass slides (15 mm x 25 mm). Each sample was submerged in the solution of interest and removed periodically for UV-vis transmission measurements. The solution was left still and covered for the period of each exposure. The noted times denote cumulative exposure.

All electrochemical measurements were performed in an HDPE electrochemical cell with the active area of the working electrode (0.5 cm^2) defined by a viton o-ring. The electrodes were oriented in the cell so that the entire working area was uniformly coated with the electrocatalyst of interest. All cyclic voltammetry (CV) measurements were performed at a scan rate of 20 mV s^{-1} using a three-electrode configuration with a Pt wire counter electrode and an Ag/AgCl (sat. KCl) reference electrode. We additionally observed that the Vycor frit on the reference electrode dissolved when left in 1 M NaOH for 24 hours.

To avoid this deterioration of the reference electrode, chronopotentiometery (CP) measurements of electrochemical stability in 1 M NaOH were performed in a two-electrode configuration with a Pt wire counter electrode.

3.4. Results

3.4.1 Structural and Electrical Characterization of ALD-deposited Thin Films:

1000 cycles of ALD-deposited AZO (abbreviated 1000c AZO) grown on n^+-Si resulted in a film thickness of 170 nm, as measured by cross-sectional SEM (Figure 3.1a). The observed growth rate was consistent with previous measurements (0.17 nm $cycle^{-1}$) for ZnO ALD under similar conditions.[106,107] A 300c TiO_2 film on 1000c AZO was roughly 10 nm thick from an EDX line scan measurement (Figure 3.1b). XRD measurements showed that the as-deposited ZnO was crystalline (Figure 3.1c). No significant change to the diffraction pattern was observed after the addition of TiO_2, indicating that the TiO_2 deposition was either too thin to generate Bragg reflections or that the as-deposited TiO_2 was amorphous. Measurements of the Zn $2p_{3/2}$ (Figure 3.2a) and Ti 2p (Figure 3.2b) confirmed the TiO_2 chemical state of the deposited overlayer and that the deposition was conformal.[108] ZnO XPS features were not observed on samples with 100c or 300c TiO_2, indicating that the deposited TiO_2 was conformal and thicker than the sampling depth of the XPS measurement.

We measured the sheet resistance of ALD-deposited films with a four-point probe station. To isolate the electrical properties of the AZO-based films, they were deposited either on glass microscope slides or on polished Si substrates prepared with a 300 nm thermal oxide layer (Table 3.1). The as-deposited, 1000c AZO film had a sheet resistance of 83 Ω sq^{-1} on the thermal oxide substrate and 85 Ω sq^{-1} on the glass substrate. The roughness of the glass slide did not have a significant effect on the sheet resistance of AZO. Measurements of 100c and 300c TiO_2 films were out of range of the instrument, indicating a sheet high lateral

resistance. 1000c AZO+300c TiO_2 layered films had sheet resistances of 79 Ω sq^{-1} and 71 Ω sq^{-1} on glass and thermal oxide, respectively, which was slightly lower than the AZO alone.

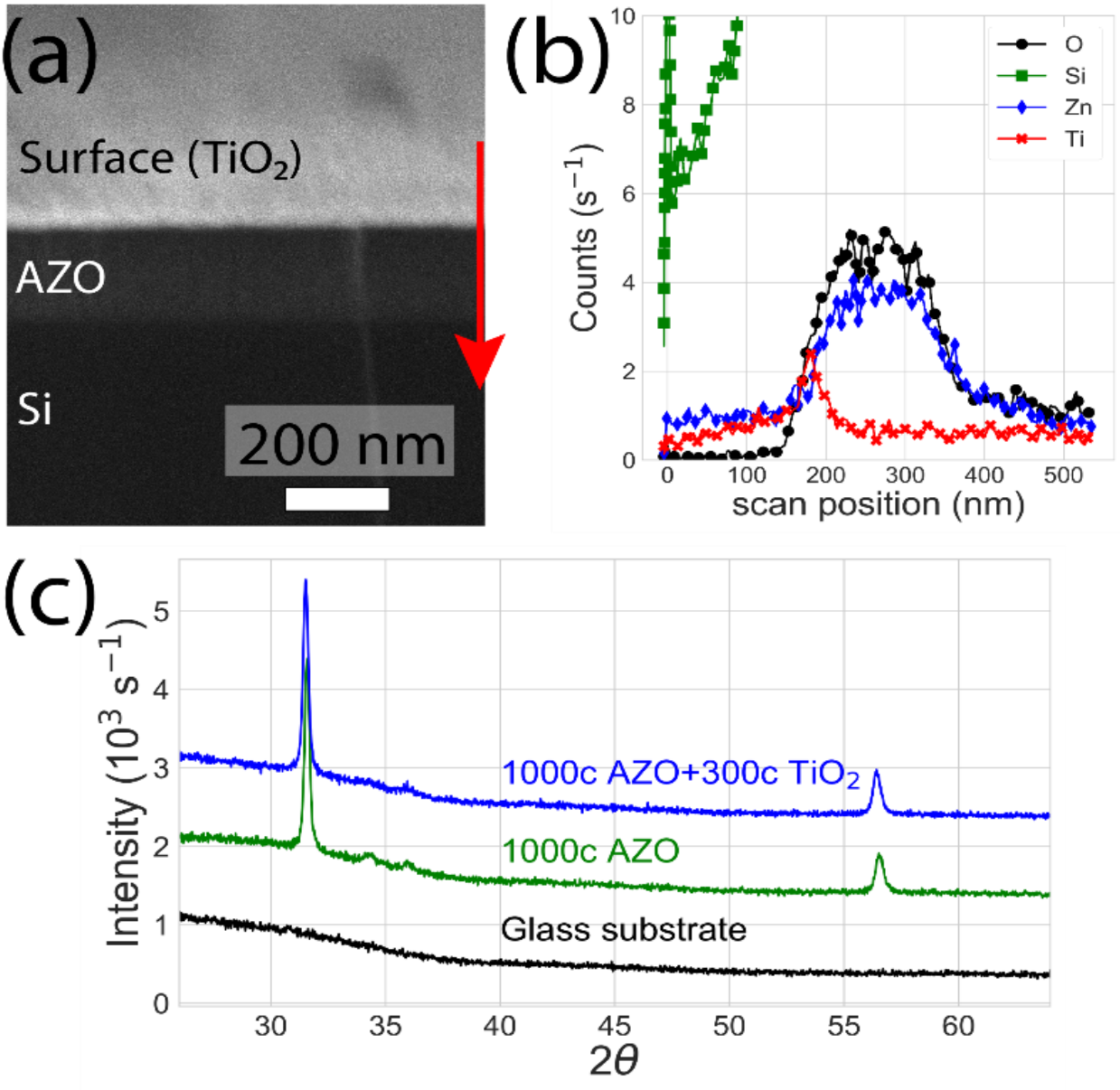

Figure 3.1 - (**a**) A cross-sectional SEM image of an ALD-deposited 1000c AZO+300c TiO_2 film on an n^+-Si substrate. (**b**) An EDX line scan (along red arrow) of the edge of the electrode shown in (a). (**c**) Powder x-ray diffraction spectra of as-deposited 1000c AZO and 1000c AZO+300c TiO_2 grown on glass substrates.

Table 3.1 – Sheet resistance measurements of ALD-deposited AZO, TiO_2, and layered films. 'OOR' signifies measurements that out of the range of the four-point probe measurement (> 5 kΩ sq^{-1}). Variance in measurements on the same film was roughly ±1 Ω sq^{-1}. The slight reduction of resistivity of the 1000c AZO after adding a 300c TiO_2 layer may be related to improved contact resistance between the interface and the probe tips.

Film Composition	*R_s on Glass (Ω sq^{-1})*	*R_s on Thermal Oxide (Ω sq^{-1})*
250c ZnO (undoped)	*1200*	-
250c AZO	*648*	-
1000c AZO	*85*	*83*
100c TiO_2	*OOR*	-
300c TiO_2	*OOR*	*OOR*
1000c AZO+100c TiO_2	*89*	-
1000c AZO+300c TiO_2	*79*	*71*

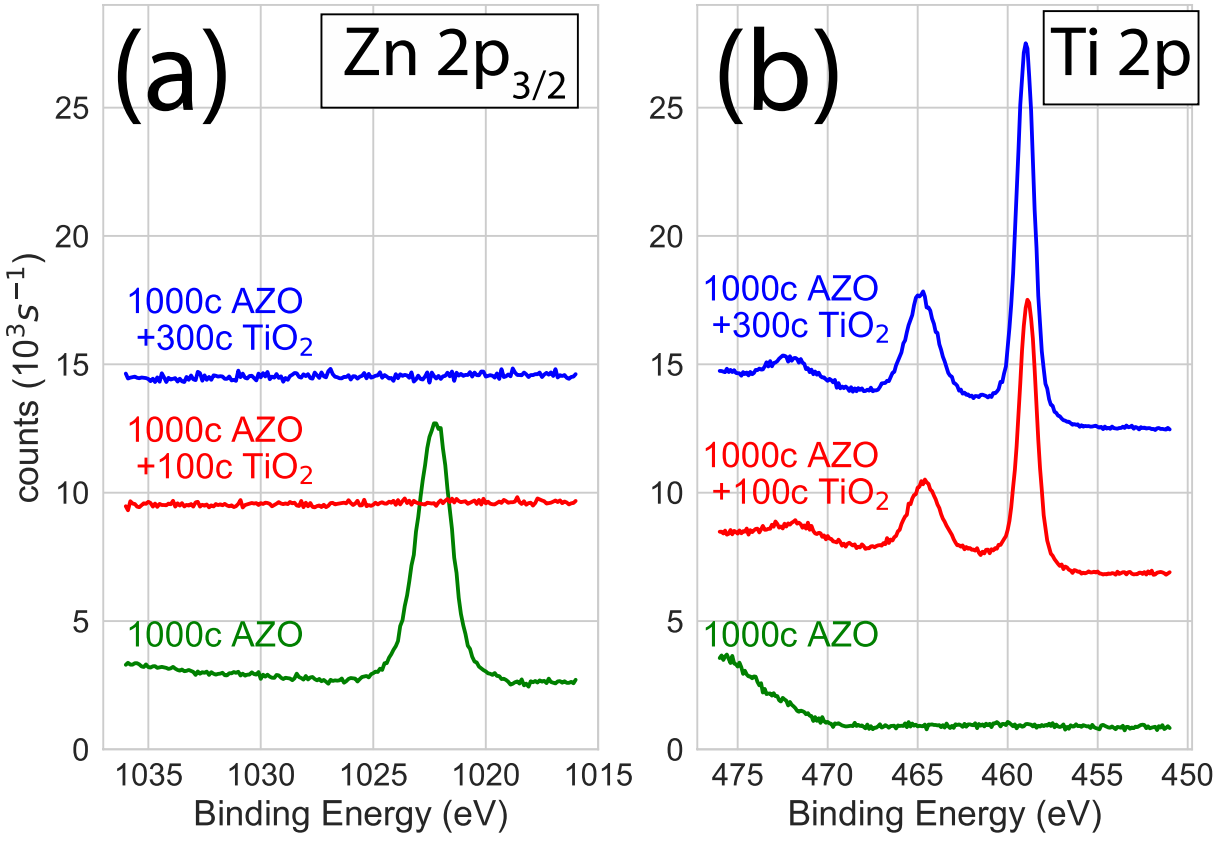

Figure 3.2 – (**a**) Zn $2p_{3/2}$ and (**b**) Ti 2p XPS spectra for ALD-grown 1000c AZO, 1000c AZO+100c TiO_2, and 1000c AZO+300c TiO_2 films on n^+-Si substrates.

3.4.2 Chemical Stability of TiO_2-protected AZO:

We measured the acid- and base-stability of AZO as a function of the thickness of the TiO_2 protection layer by transmission UV-Vis spectroscopy. The spectra clearly show the difference between slides coated with the ALD ZnO layer and ones where the ALD layer had dissolved, based on the fact that the ZnO has a pronounced and well-defined band gap at lower energy than the glass substrate. This transformation can be used to monitor the dynamics of the dissolution of the ALD-deposited film. Figure 3 shows the UV-vis transmission spectra for AZO+TiO_2 films on glass slides under increasing cumulative exposure to 1 M NaOH solution (pH 13.5). Each series of measurements was performed in triplicate on identically prepared slides, though only one series for each electrode construction is shown in Figure 3.3. The others are shown for comparison in Figure A1. Transmission measurements on an unprotected 1000c AZO-coated substrate (Figure 3.3a) showed that the AZO film had noticeably dissolved within 5 min. The spectrum was virtually identical to the transmission spectrum of an uncoated glass substrate within 15 min, indicating that the AZO film had completely dissolved within that period. The transmission measurements for a 1000c AZO+100c TiO_2 film began to change significantly between 15 min and 30 min (Figure 3.3b), and the film was completely dissolved within 60 min. Measured spectra for a 1000c AZO+300c TiO_2 film showed almost no change even after 24 hours of submersion (Figure 3.3c). The 300c TiO_2-protected films survived more than 288 times longer than the unprotected AZO in the NaOH solution. Photographs of 1000c AZO+300c TiO_2 protected films after a 24 hour NaOH exposure is shown in Figure A2, where the films appear to etch from the edges of the sample. This suggests that the slight dissolution observed in the transmission measurements could be caused by underetching of the glass substrate rather than failure of the protection layer.

Figure 3.4 shows the UV-vis transmission spectra time series for 1000c AZO films with varying thickness of TiO_2 protection layers on glass slides under increasing cumulative

exposure to aqueous 1 N H_2SO_4 (pH 0.5). Each film construction was measured in triplicate, and additional series are shown in Figure A3. Each unprotected 1000c AZO film dissolved within 30 s of acid exposure (Figure 3.4a). The transmission spectrum for a 1000c AZO+100c TiO_2 film (Figure 3.4b) shows that the dissolution is slightly slowed but complete within 60 s. The transmission spectra for 1000c AZO+300c TiO_2 films (Figure 3.4c) began to show slight changes indicating some dissolution after 120 minutes. The 1000c AZO+300c TiO_2 films were dissolved after 240 minutes (not shown). However, the 300c TiO_2-protected films survived more than 240 times longer than the unprotected AZO at pH 0.5.

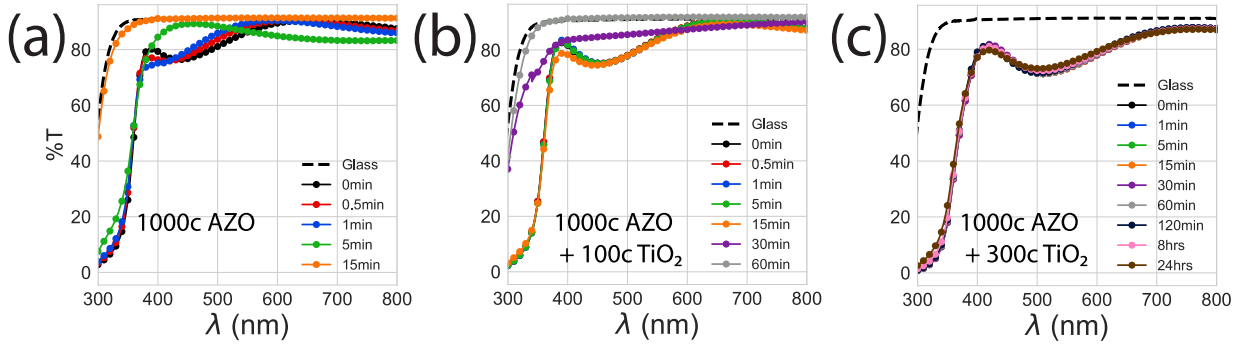

Figure 3.3 – Series of UV-Vis transmission spectra of (**a**) 1000c AZO, (**b**) 1000c AZO+100c TiO_2, and (**c**) 1000c AZO+300c TiO_2 as a function of total exposure to 1 M NaOH (pH 13.5). The dissolution of the film is evident by the convergence of the measured spectrum to the substrate spectrum (a glass slide without ALD coating). Duplicates for the spectral series for each film construction are shown in Figure A1.

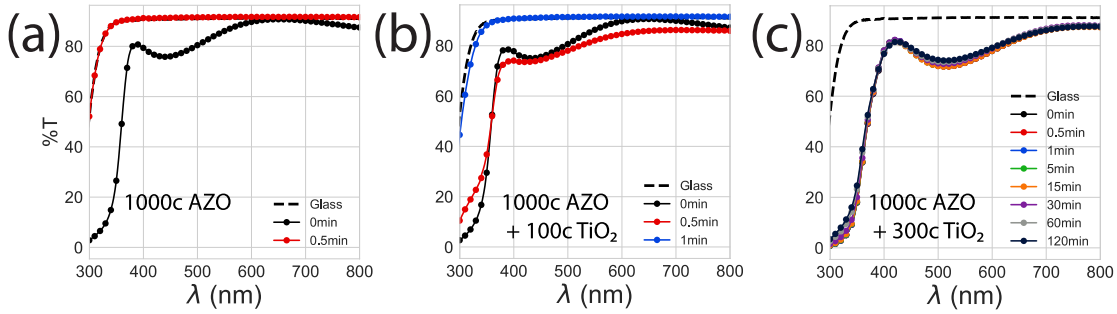

Figure 3.4 – Series of UV-Vis transmission spectra of (**a**) 1000c AZO, (**b**) 1000c AZO+100c TiO_2, and (**c**) 1000c AZO+300c TiO_2 as a function of total exposure to 1 N H_2SO_4 (pH 0.5). The dissolution of the film is evident by the convergence of the measured spectrum to the substrate spectrum (a glass slide without ALD coating). Duplicates for the spectral series for each film construction are shown in Figure A1.

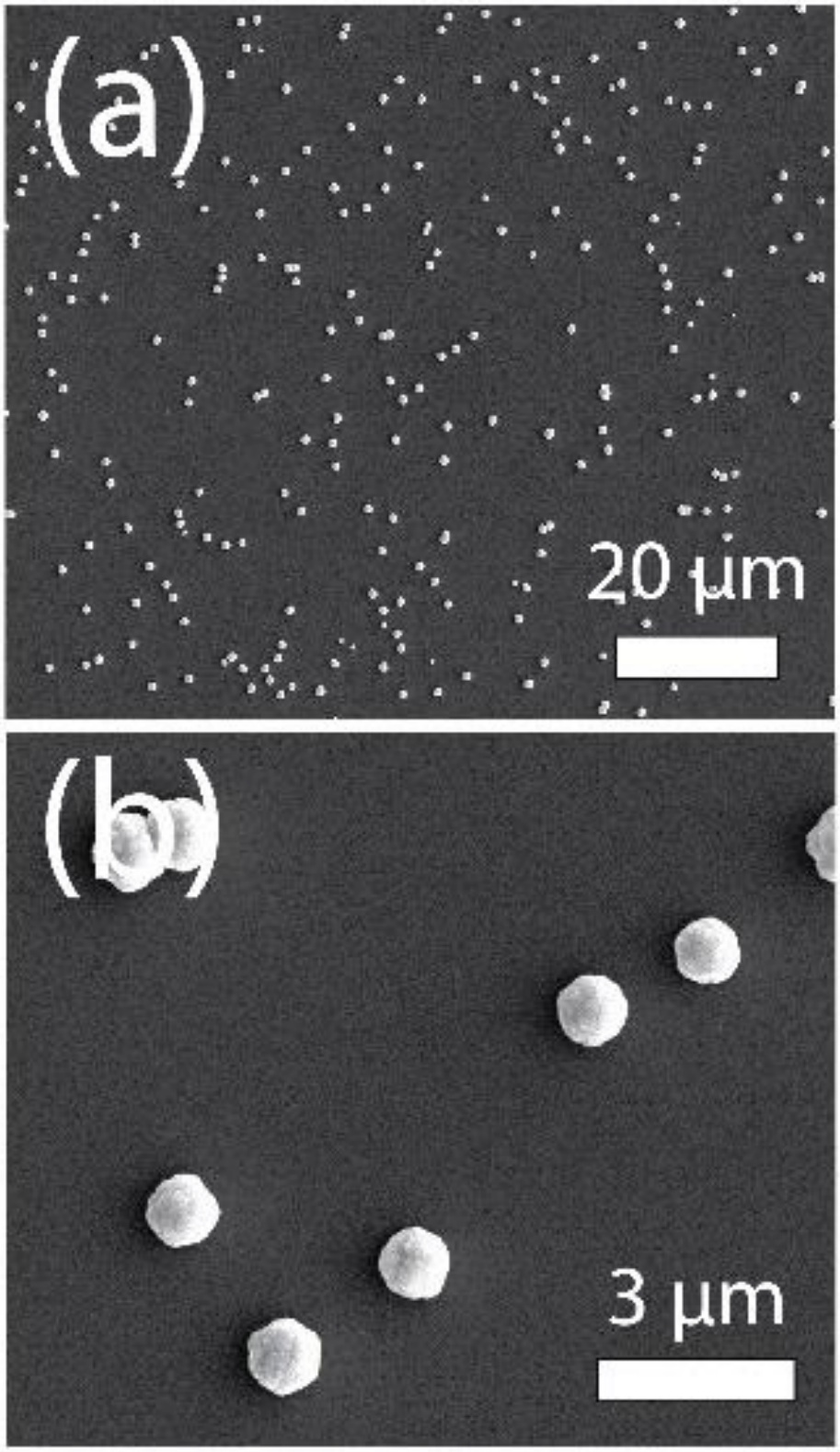

Figure 3.5 – (**a**) Wide-field and (**b**) high-magnification SEM images of electrodeposited Pt nanoparticles on a 1000c AZO+300c TiO_2 electrode.

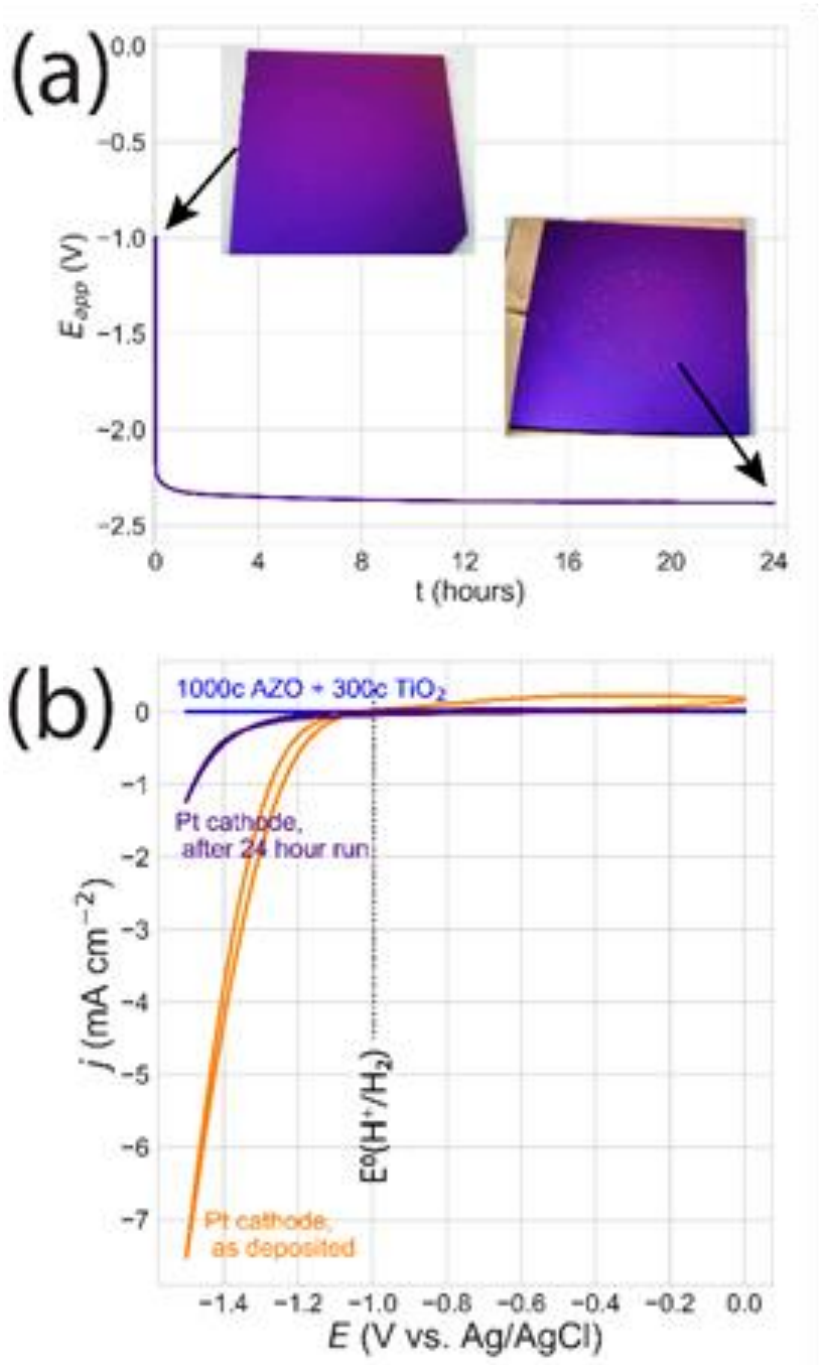

Figure 3.6 – (**a**) Two-electrode chronopotentiometry measurements of the applied potential (E_{app}) of a Pt nanoparticle-coated, 1000c AZO+300c TiO_2 cathode, run at -2 mA cm^{-2} in 1 M NaOH. After 24 hours, the electrode was still operational and showed no significant dissolution of the ALD-deposited layers. *Inset*: as grown electrode (left), after Pt electrodeposition and run for 24 hours (right). (**b**) Cyclic voltammograms of 1000c AZO+300c TiO_2 with electrodeposited Pt at the beginning (orange) and end of the cathodic CP measurements in (a) (purple). For comparison, the current passed by an identical electrode without added Pt (blue) was indistinguishable from zero at this scale.

3.4.3 Electrochemical Stability of TiO_2-Protected AZO:

Chemical stability tests showed that the addition of a 300c TiO_2 protection layer improved the passive chemical stability of the AZO films. The film must also be stable under active, electrochemical conditions to be used as a TCO. To demonstrate that these films can be used in the applications of interest, we fabricated cathodes and anodes based on 1000c AZO films with varying degrees of TiO_2 protection. The ALD film acted as the conducting electrode layer and an added co-catalyst for the appropriate half-reaction for electrolytic water splitting. These experiments are intended to demonstrate the facile electron transfer from electrode to catalyst required for the ALD films to operate as a current collector.

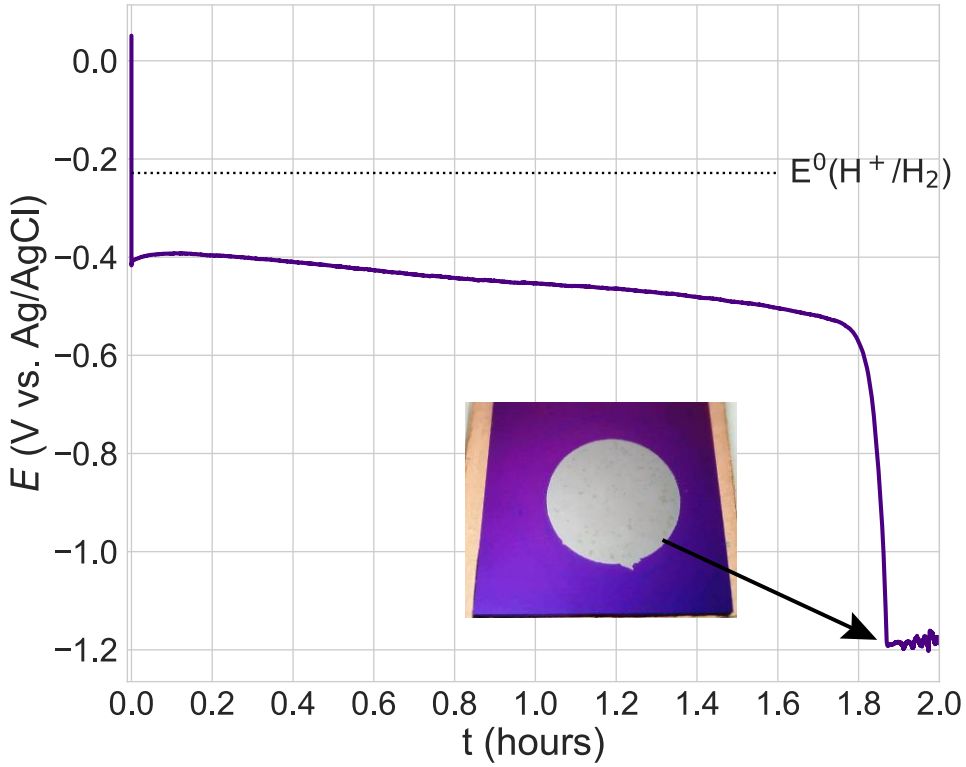

Figure 3.7 – Three-electrode chronopotentiometry measurements of a Pt nanoparticle-coated, 1000c AZO+300c TiO_2 cathode run at -2 mA cm^{-2} in 1 N H_2SO_4 (Ag/AgCl in saturated KCl reference electrode). After roughly 105 minutes, the TiO_2 protection layer failed and the ALD-deposited film dissolved (inset), as noted by the rapid cathodic shift in the working electrode potential. After this point, cathodic current is driven by HER on the exposed Si substrate.

Cathode electrodes for the hydrogen evolution reaction (HER) were prepared by electrodepositing Pt onto n^+-Si electrodes coated with a 1000c AZO+300c TiO_2 TCO layer as a current collector. The electrodeposition resulted in a sparse distribution of nanoparticles with an average diameter of roughly 800 nm (Figure 3.5). AZO films without the 300c TiO_2 layer dissolved immediately in the acidic electrodeposition solution. CP measurements of a Pt-coated cathode were run for longer than 24 hours at -2 mA cm^{-2} in a two-electrode configuration with a platinum counter electrode in 1 M NaOH (pH 13.5) electrolyte (Figure 3.6a). CV measurements (Figure 3.6b) for the protected cathode and related constructions were measured in the same electrolyte. The CVs for the as-prepared protected cathode showed Tafel kinetics for hydrogen evolution as expected for low electrocatalyst mass loading (-4 mA cm^{-2} at -400 mV vs. RHE, normalized to the geometric area of the electrode).[109] The current was significantly reduced after 24 hours (-0.4 mA cm^{-2} at -400 mV vs. RHE), though without significant visible loss of the AZO+TiO_2 coating (Figure 3.6a, inset). The reduction is likely due to the loss of Pt over time. Negligible current was observed for CV measurements of a 1000c AZO+300c TiO_2 electrode without electrodeposited Pt or for a Pt-coated n^+-Si electrode without TCO layer over the range of measured potentials. A three-electrode CP of a Pt-coated 1000c AZO+300c TiO_2 cathode in 1 N H_2SO_4 (pH 0.5) showed that the electrode maintained -2 mA cm^{-2} for nearly two hours before the AZO and protection layer failed (Figure 3.7). The ALD-deposited film was completely dissolved after two hours (Figure 3.7, inset). These measurements of cathodic electrochemical stability are consistent with the chemical stability enhancement provided by the TiO_2 protection layer as observed in Figure 3.3.

Anode electrodes for water oxidation in 1 M NaOH were prepared by electron-beam evaporation of 1 nm or 3 nm of Ni onto electrodes coated with 1000c AZO with various degrees of TiO_2 protection. CV measurements (Figure 3.8a) of the *j-E* behavior for electrodes with 1000c AZO without a protection layer, with a 100c TiO_2 protection layer, or with a 300c

TiO_2 protection layer each showed significant current densities for water oxidation compared to a bare n^+-Si electrode when coated with a 1 nm Ni electrocatalyst layer. At these potentials, Si in contact with the electrolyte forms an insulating anodic oxide layer.[110] The unprotected AZO-coated electrode had the highest current densities of all of the anodes (42 mA cm^{-2} at 1.5 V vs. Ag/AgCl). An unprotected AZO electrode generated less than 0.1 mA cm^{-2} at 1.5 V vs. Ag/AgCl without the addition of the Ni electrocatalyst. TiO_2-protected AZO anodes passed virtually no current without the addition of the Ni electrocatalyst, even at significantly more anodic potentials than those measured in Figure 3.8a. This has been observed elsewhere for ALD-deposited TiO_2 protection layers.[96] To characterize the anodic stability of each electrode, CP measurements of each anode construction were performed in a two-electrode configuration at 2 mA cm^{-2} with a Pt wire counter electrode (Figure 3.8b). The 1000c AZO anode initially required 1.9 V to reach 2 mA cm^{-2}, but failed after 125 minutes. The 1000c AZO+100c TiO_2 anode stabilized at 4.6 V to reach 2 mA cm^{-2} within 15 minutes, though the potential monotonically increased before failing within 270 minutes. The 1000c AZO+300c TiO_2 anode initially needed 2.4 V to reach 2 mA cm^{-2}, though E_{app} slowly increased for the first 12 hours of operation to 3.3 V. After 12 hours, the bias began to increase more rapidly, though had still not failed completely after 20 hours. A 1000c AZO+300c TiO_2 anode and uniformity to protect the underlying layers from dissolution, negating the with a 3 nm layer of evaporated Ni showed significantly improved anodic stability for 24 hours. This anode construction had higher current densities (55-70 mA cm^{-2} at 1.5 V vs. Ag/AgCl) (Figure3.8c) that increased after 24 hours, which suggests that the oxidation of the Ni metal catalyst layer roughens the surface over the duration of the experiment. The enhanced stability of the electrode indicates that the 3 nm Ni layer is of sufficient thickness usefulness of the TiO_2 protection layer.

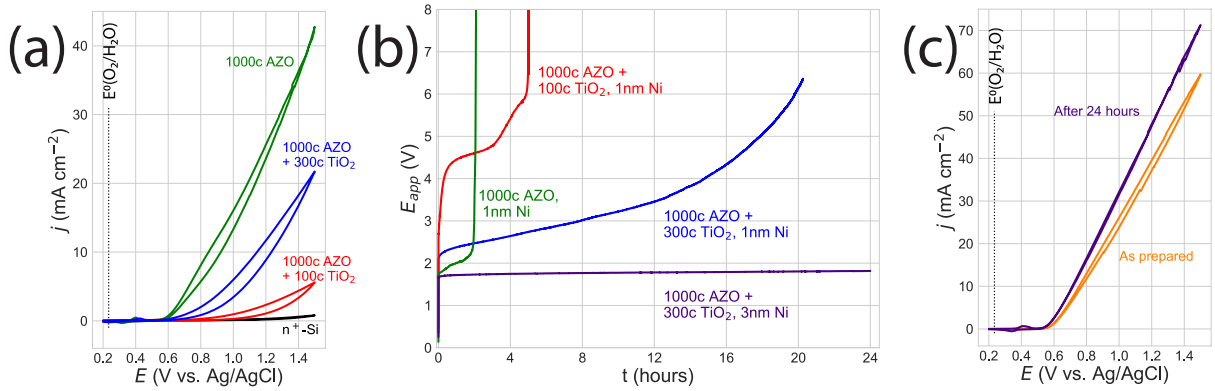

Figure 3.8 – (**a**) CV measurements of water oxidation on anodes prepared via the electron-beam evaporation of a 1 nm Ni layer on 1000c AZO (green), 1000c AZO+100c TiO_2 (red), 1000c AZO+300c TiO_2 (blue), and n^+-Si substrate (black) electrodes. (**b**) Two-electrode CP measurements of the ALD-deposited electrodes from (a) and a 1000c AZO+300c TiO_2 electrode with a 3 nm Ni electrocatalyst layer. Each electrode was run at 2 mA cm^{-2} in 1M NaOH until failure, as designated by the rapid increase in applied bias (E_{app}) required to maintain the targeted current density. (**c**) CV measurements of the 1000c AZO+300c TiO_2 electrode with 3 nm Ni as-prepared (orange) and after 24 hour anodic CP experiment in (b).

In the described experiments, the effect of the protection layer resulted in longer operation for electrodes in alkaline conditions compared to ones in acid. We imaged the 300c TiO_2-protected electrodes by post-*operando* SEM to understand the failure modes for electrodes run in the 1 M NaOH electrolyte. Pitting was observed in the ALD film for a Pt-coated cathode after running for 24 hours at -2 mA cm^{-2}. The pits were characteristically square and limited in size to less than 100 μm in diameter (Figure 3.9a). For the anode, the films were nearly completely etched under through pinholes in the TiO_2 film (Figure 3.9b). In some areas, the TiO_2 overlayer remains intact, suspended or laying on the Si substrate where the AZO had been etched from underneath (Figure 3.9c). A small fraction of the surface area remained intact and was able continue to pass anodic current during the run.

3.5 Discussion

The experiments described here show that the chemical and electrochemical stability of ALD-deposited AZO films can be significantly improved through the addition of a thin TiO_2 overlayer. The AZO remains conductive and functional as a TCO with the protection layer. As

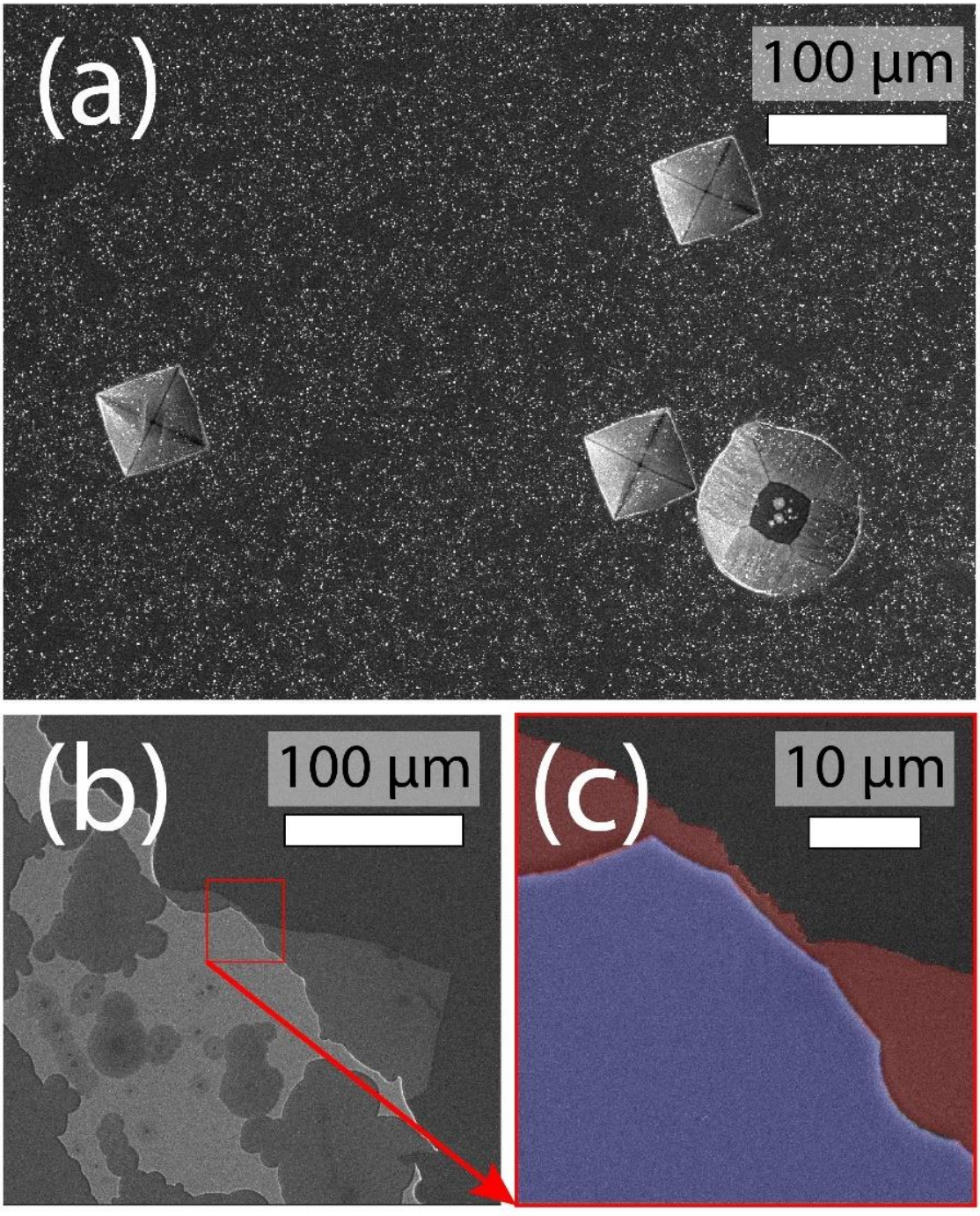

Figure 3.9 – Post operando SEM images of electrode failure in (**a**) 0.5 M H_2SO_4 (run for 24 hours at -2 mA cm^{-2}) and in (**b**,**c**) 1 M NaOH. In both cases, etching appeared to occur through pinholes in the protection layer. The film formed characteristically square pits in the acidic solution (a). The alkaline solutions etched AZO from underneath the TiO_2 layers (b) leaving TiO_2 suspended or laying on the Si surface. The composition of the AZO/TiO_2 film (blue) and TiO_2 only regions of the film (red) in the false-color SEM image (c) were confirmed by EDX.

ALD is a self-limiting and surface-specific method for growing thin films, this strategy can be extended to fabricate conductive layers on tortuous, hierarchically structured, or other high-aspect ratio substrates where a TCO cannot be deposited by line-of-sight deposition methods. As a result, visible light-absorbing, ultra-thin film semiconductors (Fe_2O_3, CuO) can be integrated into cost-effective hierarchical electrode designs that allow for solar energy conversion with potentially high power conversion efficiency.[13,19]

The results here are also not specific to the chemistry of AZO, as thin TiO_2 layers have been used to protect other substrates in similar environments. The longevity of the underlying films will require further improvement in order to be considered generalizable to a wide range of electrochemical applications. The failure of the layered AZO/TiO_2 TCO was the result of the dissolution of the AZO layer through pinholes or other defects that form in ultra-thin, ALD-deposited TiO_2 layers.[111] The most straightforward solution to this problem is to increase the thickness of the TiO_2 layer. Photoelectrode designs have been demonstrated for hundreds of hours of stable operation with protection layers of 100 nm or greater, roughly ten times the thickness used in this work.[96,112,113] This may improve the stability of AZO, though it could also increase the resistivity of the film and the efficiency of the resulting electrocatalytic reaction.[114] Identifying chemical methods to passivate pinholes in the TiO_2 layer can also solve this problem.

In some cases, the stability improvements shown here will be sufficient to prepare conformal, functional layers that will mitigate the negative effects of the pinholes. For example, a 10 nm TiO_2 layer provides sufficient protection for an AZO TCO to allow for the electrodeposition of a semiconductor like WO_3 or Fe_2O_3 from an acidic bath. The acidic Pt electrodeposition bath dissolved an unprotected AZO layer, yet was useful for fabricating a cathode for driving HER in a basic solution for more than 24 hours. Electrodeposited WO_3 or Fe_2O_3 films generally require a post-deposition annealing step to form the desired photoactive

phase. The high-temperature stability of the TCO must also be considered. Air annealing has been shown to increase the resistivity of ALD-deposited AZO films.[59,84] The relatively low sheet resistance of undoped, ALD-grown ZnO (Table 1) and the effects of annealing suggest that oxygen deficiencies or other intrinsic doping is responsible for the electrical conductivity of the films. The anisotropic, layered distribution of Al through the ZnO film has been proposed as the cause of the low Al doping efficiency in ALD-derived AZO.[115] Even if the chemical stability of ALD-derived AZO can be improved, a better understanding of the solid-state chemistry of the doping process is necessary to enable its general application as a TCO.

3.6 Conclusion

In conclusion, we have shown that the chemical stability of ALD-deposited AZO thin films can be enhanced by the addition of a 10 nm TiO_2 protection layer. The lateral conductivity of the film remains unchanged between as-prepared AZO and TiO_2-protected AZO films. Moreover, the thin protection layer increases the lifetime of AZO-based electrodes by more than a factor of 120. We showed that these films can be used as conductive substrates for catalysts driving the hydrogen evolution and water oxidation reactions at pH values of 0.5 and 13.5. Based on the stability of TiO_2 as inferred from its Pourbaix diagram, it is likely that the protected AZO layers are also stable for the range of pH values in between our measured extremes.[116] The general mode of failure on these electrodes was electrolyte penetration through pinholes in the substrate. The generality of the protection layer strategy and ALD as a thin-film coating technology suggests that this approach will be useful for preparing a unique range of hierarchically structured electrodes for electrochemical energy conversion applications.

Chapter 4. Building a CuO Photocathode for Photoelectrochemistry

4.1 Abstract

Cupric oxide (CuO) is a potentially desirable photocatalyst for industrial scale photoelectrochemistry (PEC): an earth abundant p-type semiconductor with a band gap of 1.2-1.7eV, enabling absorbing a large portion of the solar spectrum. Additionally, the position of the conduction band edge is appropriate for driving the hydrogen evolution half-reaction (HER) component of water splitting. However, like the other common oxidation state of copper, cuprous oxide (Cu_2O), a film of CuO dissolves during catalytic operation under illumination in water in the process of photocorrosion. We used Atomic Layer Deposition (ALD) to protect CuO with a layer of 20nm Al:ZnO (AZO) and 10nm TiO_2 in an attempt to mitigate photocorrosion. Additionally, the solid-state energetics of the back contact, or hole collecting layer, of a CuO photoelectrode is evaluated in the context of a photocathode. We hypothesize a work function difference between a semiconductor, specifically CuO, and the current collecting back contact, will affect the performance of the photoelectrode. Nickel (Φ = 5.35eV) consistently outperforms F:SnO_2 (FTO; Φ = 4.3eV) as a back contact for CuO during photoelectrochemical measurements. A thorough discussion of the viability of CuO as a photocathode material now, and in the future, was completed based on the results of this work as well as current literature.

4.2 Introduction

In the search for semiconducting materials for solar-to-photoexcited electron energy conversion (for PEC or photovoltaics), materials that are earth abundant and have inexpensive manufacturing methods, copper (II) oxide, or cupric oxide, emerges as a promising material. For a semiconductor material to convert solar energy with maximal efficiency into chemical bonds, several metrics must be met. The bandgap of the semiconductor should approach the Shockley-Queisser limit of 1.1eV for maximum energy collection in photovoltaic devices.[22] However, in solar energy driven hydrogen generation, an absolute minimum band gap of a single semiconducting material, 1.23eV, is set by the thermodynamic potential for water splitting. Kinetic and transport losses in a device further increase the minimum band gap needed for a single PEC device to split water.[32,117] Additionally, the ideal semiconducting material for the hydrogen evolution reaction (HER), would have a conduction band (CB) edge potential positive of the water reduction potential, while an ideal material for the oxygen evolution reaction (OER) would similarly have a valence band (VB) edge that is below the water oxidation potential.[118] Furthermore, the photoelectrode must be physically stable during operation; resistant to photocorrosion and environmental degradation. Lastly, availability of the light absorber and energy input of synthesizing a PEC device is a necessary externality for scaling to an industrial level.[41]

Copper (II) oxide is an intrinsically p-type semiconductor with a band gap of 1.2eV-1.7eV, varying upon method of preparation. The band gap approaches the ideal of the Shockley-Queisser limit.[119] The innate p-type nature of CuO lends itself to driving reduction reactions. The conduction band edge is just above the voltage of the hydrogen evolution half-reaction; making CuO a promising candidate as a semiconductor photocathode material for water splitting.[120] The absorption spectrum of CuO has been used to predict the max theoretical photocurrent density of a CuO photoelectode as 35 mA cm^{-2}, [121,122] which is well

above the minimum 5-10 mA cm^{-2} benchmark for commercial adoption estimated by the US Department of Energy.[12,28]

Several recent publications demonstrate a rising interest in CuO as a photocathode while repeatedly exposing the need for two improvements of high operational importance to a CuO based photocathode. Some publications address the inherent issue of photocorrosion; a process where CuO electrodes, when under a potential bias and illumination, quickly dissolve and no longer produce photocurrent. The exact mechanism of photocorrosion is unknown, with several proposed reaction pathways, while protection layers to isolate CuO from aqueous solution during photocatalysis mitigates this issue.[123-125] Other studies have highlighted the need for a majority carrier back contact that is Ohmic to CuO or have propensity for selecting holes in order to combat reductions in efficiency from recombination of excited electron-hole pairs.[126,127] A majority of laboratory solid-state electrochemical research is performed on the transparent conducting oxides of FTO or ITO; however these materials have a work function that does not provide such an Ohmic interface to a p-type semiconductor, while they are Ohmic to n-type semiconductors such as iron (III) oxide and tungsten (VI) oxide. However, publications that address corrosion rarely address energetics of the back contact for their device, and vice versa. The current work aims to marry these two concepts utilizing ALD protection layers, and in future, 3-dimensional structuring.

The disconnect may be in part to the standard methodologies used to evaluate PEC devices, mainly referencing the shortcomings of linear sweep voltammetry (LSV). The photocorrosion of CuO, in solution, occurs at applied potentials just positive of 0.0V vs RHE; the thermodynamic HER potential. The absorption of light provides energy in a p-type semiconductor such as CuO and shifts the onset potential of catalyzed reduction reactions in a positive direction. Since the corrosion of the CuO is drastically accelerated by illumination, this can result in a situation where an observer is expecting to see photoelectrochemical

effects, but instead, could easily be observing photocorrosion; the two are not easily resolved in LSV. However, a complete cyclic voltammogram, or long-form stability study, in the form of chronopotentiometry or chronoamperometery does reveal the difference. The anodic sweep of a CV, while a CuO photocathode is being tested as a PEC device, can be evaluated to determine whether corrosion or hydrogen evolution is dominate. An oxidation peak characteristic of hydrogen desorption is often present while HER is dominate. If photocorrosion is present, some oxidation peak will occur as part of the mechanism of dissolution, and in the case of the presence of protection layer, the current will increase in successive sweeps of a CV. To combat this issue, protection layers have been utilized on CuO, including TiO_2,[123] WO_3,[128] ZnO,[124,129] and Al_2O_3.[130]

For a back contact to maintain an Ohmic contact (or even one that generates a back surface field to reject the minority carriers) to a p-type semiconductor, the work function of the conductor must be lower than the fermi energy of the semiconductor. The initial work aimed to directly compare FTO, with a workfunction of 4.7eV, and nickel, with a workfunction of 5.35eV (Figure 4.1).[131-134] Cupric oxide has a reported fermi energy, and therefore, a workfunction of 5.3 eV, making nickel theoretically an Ohmic backing.[135] Another substrate was chosen to further compare the effect of the workfunction upon device performance: Ag, with a workfunction of 4.6eV, providing an unfavorably biased back contact.[133]

In this work, we fabricated electrodes using electrodeposition of cuprous oxide onto the substrate in a press cell which are then annealed to CuO. The cupric oxide layer was subsequently protected with 20nm of AZO, and 10nm of TiO_2, modelled after previous work protecting cuprous oxide and work presented in Chapter 3.[84] Finally, a sparse catalytic deposition of Pt was applied to assist in direct comparisons of the photoelectrical properties of the electrodes (Figure 4.2). Three methods of deposition for the Pt sites were considered

and compared: galvanic replacement of Cu^{+} with Pt, electrodeposition, and use of a benchtop sputter coater. Photoelectrochemical analysis using cyclic voltammetry was used to compare electrodes constructed on FTO, Ni, and Ag. An investigation into failure points in the ALD protection layers lead to a discussion in limitations of current technical knowledge necessary in the construction of a hierarchically structured CuO photocathode.

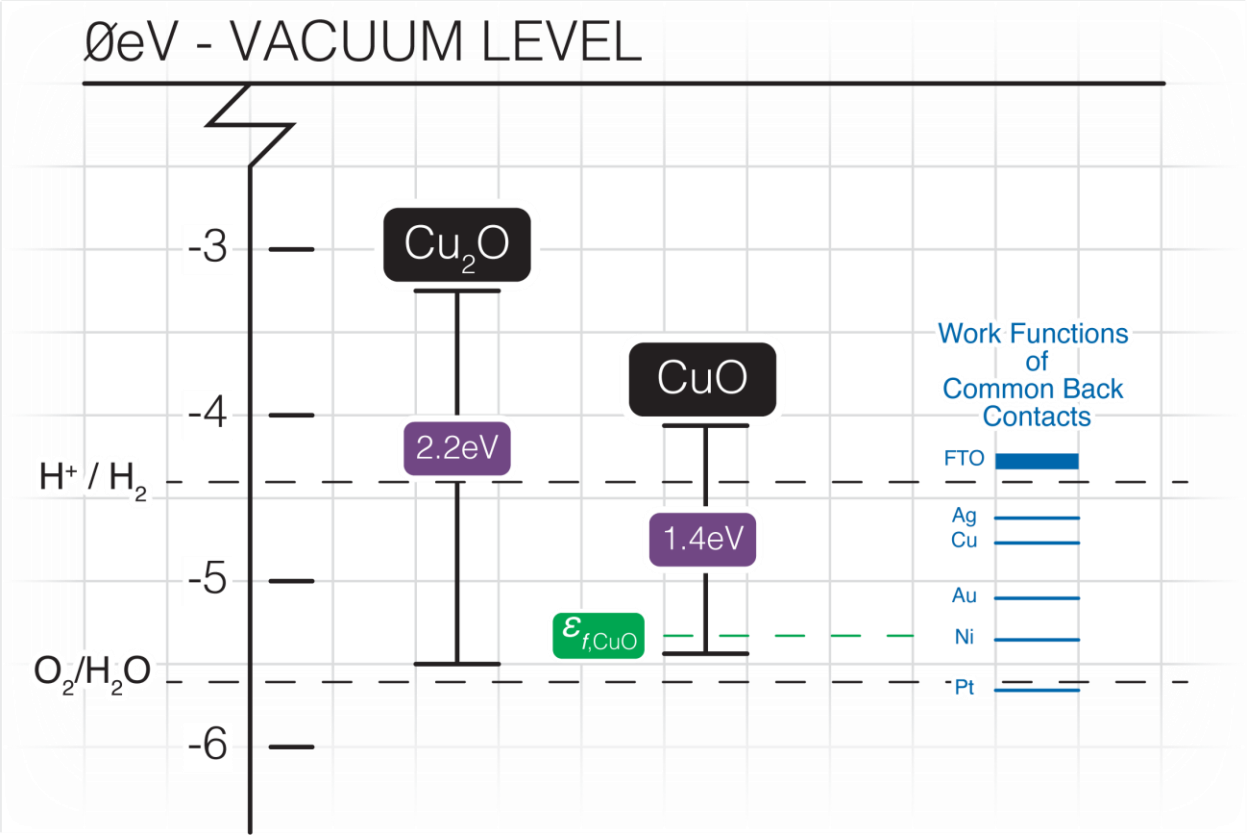

Figure 4.1 Energetics of Copper Oxides and the Choice of a Back Contact. Both cuprous oxide (Cu_2O) and cupric oxide (CuO) have a conduction band edge above potential of hydrogen reduction, making them capable of HER. The larger band gap and position of the conduction band of Cu_2O lowers the maximum theoretical solar conversion efficiency for HER when compared to CuO. The fermi energy of CuO ($\varepsilon_{f,CuO}$) is -5.3eV vs vacuum, as shown in green. Shown in blue are the work functions of several common back contacts. FTO and Ag, both substrates utilized in this work, possess work functions significantly above the fermi energy of CuO. Ni has a work function of 5.35eV, near equivalent to the fermi energy of CuO, theoretically forming an Ohmic contact.

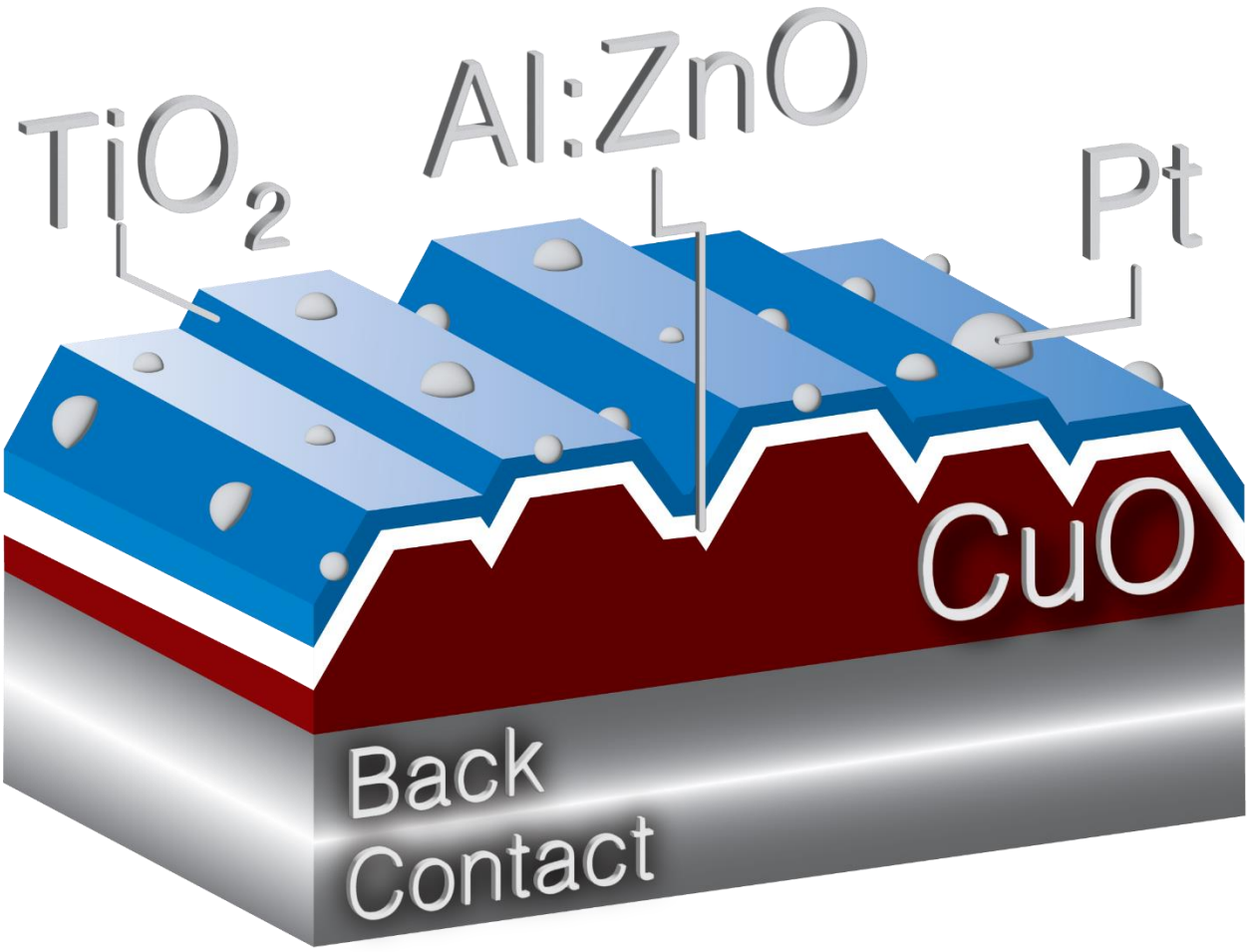

Figure 4.2 Schematic of CuO Photocathode construction. A 300-400nm layer of Cu_2O is electrodeposited on the back contact, either FTO, Ni, or Ag, and subsequently annealed to CuO in air. ALD is used to deposit 20nm of Al:ZnO and 10nm of TiO_2 as a protection layer to mitigate photocorrossion. Sites of Pt deposition are sparsely distributed across the surface to facilitate hydrogen reduction used for direct comparison of electrode constructions, while not interfering with light absorption of the photoactive layer.

4.3 Experimental

Acetone (99.5%; EMD Millipore Corp), methanol (high-performance liquid chromatography (HPLC) grade; VWR Analytical), isopropanol (HPLC grade; VWR Analytical), water (HPLC grade; VWR Analytical), Copper(II) sulfate hydrate (98%; Sigma-Aldrich), lactic acid solution (reagent grade, 85%; Sigma-Aldrich), sodium hydroxide solution (50% w/w; VWR)

were used as received. Potassium hexachloroplatinate(IV) (≥99.99%, Sigma-Aldrich) was used as received. Fluorine-doped tin oxide (FTO)-coated substrates (TEC-15, 12–14 U sq; MTI Corp) were diced and rinsed in acetone, methanol, and isopropanol. Nickel foil (0.5mm, 99.5%; BTC) and silver foil are diced, polished with 400 grit, 800 grit, 1000 grit, and 1500 grit sandpaper, rinsed in DI H2O, and dried in nitrogen.

4.3.1 Characterization

X-ray diffraction (XRD) measurements (Mini-Flex II, Rigaku) were performed using Cu-Ka radiation (l ¼ 1.54 A). Scanning electron microscopy (SEM) images were taken with a FEI Nova Nanolab SEM equipped with an energy-dispersive X-ray (EDX) spectrometer (Bruker XFlash 5010). X-ray photoelectron spectroscopy (XPS) measurements (Phi Versaprobe) were performed with a monochromated Al Ka source (1486.6 eV). Transmission UV−vis spectroscopy was performed on a Jasco V-780 spectrometer equipped with an integrating sphere. Electrodeposition, and photoelectrochemical characterization, were performed using a BioLogic SP-50 potentiostat, while electrochemical impedance spectroscopy measurements were completed using a Biologic SP-240.

4.3.2 Preparation of CuO

The electrodeposition solution was prepared by dissolving $CuSO_4$ in a 3.0 M lactic acid solution to a final $CuSO_4$ concentration of 400.0 mM.[136-138] The pH of the electrodeposition solution was adjusted to 10.0 by the slow addition of NaOH solution. Electrodeposition onto conductive substrates was carried out in a three-electrode configuration with a graphite rod counter electrode and an Ag/AgCl (saturated KCl) reference electrode (Bioanalytical Systems) with a potentiostat (Bio-Logic SP-50). Each electrodeposition was carried out in an electrochemical cell made of High-density polyethylene with the active area of the working electrode (1.77 cm^2) defined by a Viton O-ring. The films were synthesized by potentiostatic

electrodeposition at -0.4 V vs. Ag/AgCl while a circulator maintained a deposition solution temperature of 60ºC until a set charge density had passed (100mC/cm^2-400mC/cm^2). The films were then annealed at 500ºC for 3 hours in air.

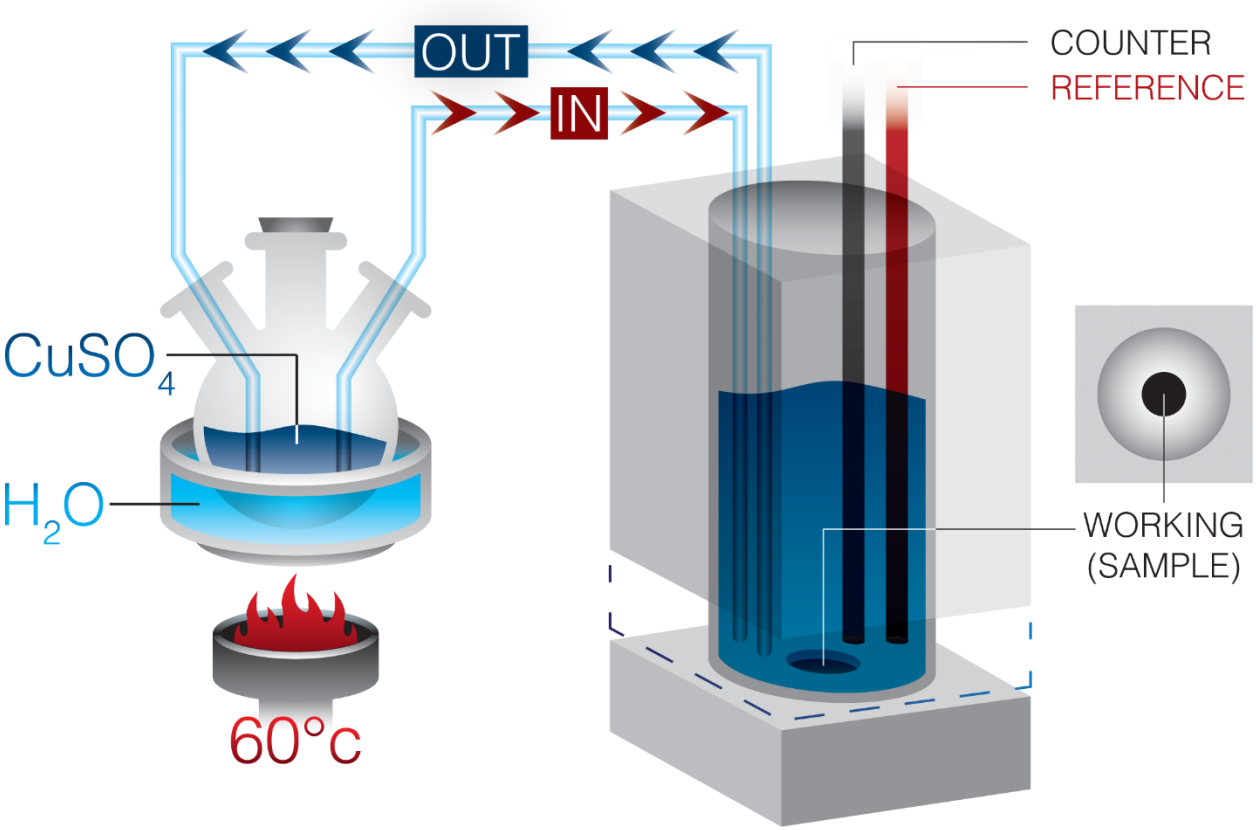

Figure 4.3 Electrodeposition of Cu_2O in a Press Cell. A HDPE cell with a vyton O-ring defined a consistent deposition area upon the substrate as the working electrode. A graphite rod counter and Ag/AgCl (sat'd) reference are used to complete the 3-electrode circuit for electrodeposition. To accelerate the deposition, a reservoir of $CuSO_4$ electrodeposition solution is circulated in a 60ºC water bath using a peristaltic pump to and from the reaction vessel.

To prevent electronic shunting through the ALD layer, Kapton tape was applied around the perimeter of the CuO deposition before samples were placed in the ALD. The ALD Growth of films is described previously, a copy of which can be found in chapter 3, but in summary, a reactor (GEMStar XT; Arradience, Inc.) was used to deposit 20nm of Al:ZnO [5x(20c ZnO, 1c

Al_2O_3)] and then 300-600 cycles (10-20nm) of TiO_2, both utilizing recipes presented previously.[139]

4.3.3 Deposition of Platinum Catalytic Sites

Platinum was deposited atop the protection layer to provide catalytic sites for HER. Three methods were used to deposit Pt and we compared their relevant PEC effects. The first method we used was galvanic replacement reaction of platinum for copper in the form of Cu_2O. The GR was performed after the deposition of the ALD layers onto Cu_2O, to try to use pinholes to our advantage, by submerging the sample in a 50mM potassium tetrachloroplatinate in 50mM sulfosalycilic acid (pH 1.36) for 1min-5mins. The sample was rinsed in DI H2O, and dried in N_2 rapidly after the allotted submerging time was met. Samples were then annealed to oxidize to CuO.

The second method employed electrodeposition in a 1mM potassium hexachloroplatinate, and 1mM hydrochloric acid, using three-electrode configuration with a graphite rod counter electrode and a Ag/AgCl (saturated KCl) reference with a potentiostat (BioLogic SP-50) which applied a constant current of -8.5μA/cm^2 for 15mins.[105,140] Platinum electrodeposition was done after annealing of copper to CuO and deposition of the ALD protection layer. The electrodeposition was performed in an electrochemical cell made of High-density polyethylene with the active area of the working electrode (1.00 cm2) defined by a Viton O-ring.

The third method, used in most photoelectrochemical measurements, utilized a benchtop sputter coater (Quorum SC7620) with a platinum sputtering target cathode (99.99%; VWR). Platinum was sputtered on CuO electrodes after ALD layers were deposited, using a deposition time of 60s, 120s, or 300s, with 120s being employed for most photoelectrochemical measurements.

4.3.4 Photoelectrochemical analysis

Measurements were made using a three-electrode configuration with a graphite rod counter electrode and an Ag/AgCl (saturated KCl) reference electrode (Bioanalytical Systems) with a potentiostat (Bio-Logic SP-50). All experiments were performed in an HDPE electrochemical cell with the active area of the working electrode (0.5 cm^2) defined by a Viton O-ring. The cell contained 60mL of 0.1M Na_2SO_4 (pH=5.8) during measurements. All cyclic voltammetry (CV) measurements were performed at a scan rate of 20 mV s^{-1}. PEC measurements were performed with an LED with a collimating lens (Thorlabs), either 565nm, 455nm, or 365nm, each with intensity adjusted to ~1.4E17 photons/sec, each calibrated with a photodiode (Thorlabs FDS101).

4.4 Results and Discussion

4.4.1 Constructing the 'Ideal' CuO Photocathode

An ideal CuO-based photocathode would be able to both produce ~10mA/cm^2 of photocurrent while reducing hydrogen and completely remain stable in its ability years. In practice, we merely want to stabilize a CuO long enough to characterize its operation. Overcoming photocorrosion and ensuring photocurrents originate from productive catalysis and not self-reduction requires an analysis of the likely mechanism of photocorrosion. Evidence shows that there is Cu_2O present on the surface as a part of the CuO photocorrosion mechanism.[123,141] Some have suggested that raising the pH reduces photocorrosion, though raising the pH also makes hydrogen reduction more difficult electrochemically.[125] The photogenerated electron-hole pair can more easily reduce CuO to Cu_2O than using that excited electron to reduce hydrogen ions, but water must participate in that mechanism in some manner at the surface of the electrode in a manner of the reaction below:[84,141]

$$2CuO(s) + H_2O(l) + 2e^- \rightleftharpoons Cu_2O(s) + 2OH^-(aq) \qquad E^o = +0.6V \text{ vs SHE}$$

As the photoelectrode is subjected to a voltage sufficient electrochemical bias to drive HER, unless isolated from water, CuO will be reduced to Cu_2O. If this were the only component of photocorrosion, the copper surface would not visibly be removed during electrochemical testing and cuprous oxide would not have the same photocorrosion problem. Additional steps in the photocorrosion mechanism must be present beyond conversion to Cu_2O. Examining cyclic voltammetry of corrosion process occurring as a protection layer fails points to an answer (Figure 4.4); features that would be impossible to observe in the standard LSV utilized to examine photoelectrodes. As the electrode is cycled multiple times in dark conditions and under illumination, the cathodic current from photocorrosion increases in successive cycles under illumination. An additional feature is present around 0.7V vs RHE at pH 5.8; an oxidation when sweeping anodically and a reduction when sweeping cathodically. Similar features have been seen on unprotected Cu_2O electrodes; XRD after cycling with these samples showed both CuO and Cu reflections.[84] Once a CuO electrode is reduced to Cu_2O there are several mechanisms that dissolve Cu_2O off of the surface.[124,142] All steps of any possible mechanism of CuO photodissolution requires the presence of water, thus an impenetrable protection layer is a necessity.

When considering a choice for a back contact of a CuO photocathode, the fermi energy of CuO and work function of the back contact must be compared. Cuprous oxide has been a material of interest for photocatalysis for significantly longer than CuO, and most work with Cu_2O utilizes thin layers of Au sputtered on FTO, though this standard did not translate to studies of CuO. For example, most CuO photoelectrochemical studies use back contacts including $Sn:In_2O_3$ (ITO; Φ = 4.7eV),[123,143-146] $F:SnO_2$ (FTO; Φ = 4.2eV),[124,129,147-154] copper films (Cu; Φ = 4.7eV),[125,155-157] and silicon wafers (Si; Φ = 4.60-4.85eV).[158] All of the back contact materials listed above possess a workfunction significantly higher than the fermi energy of CuO (ε_f = -5.3eV vs vacuum), which would create an electron selective, or hole trap state,

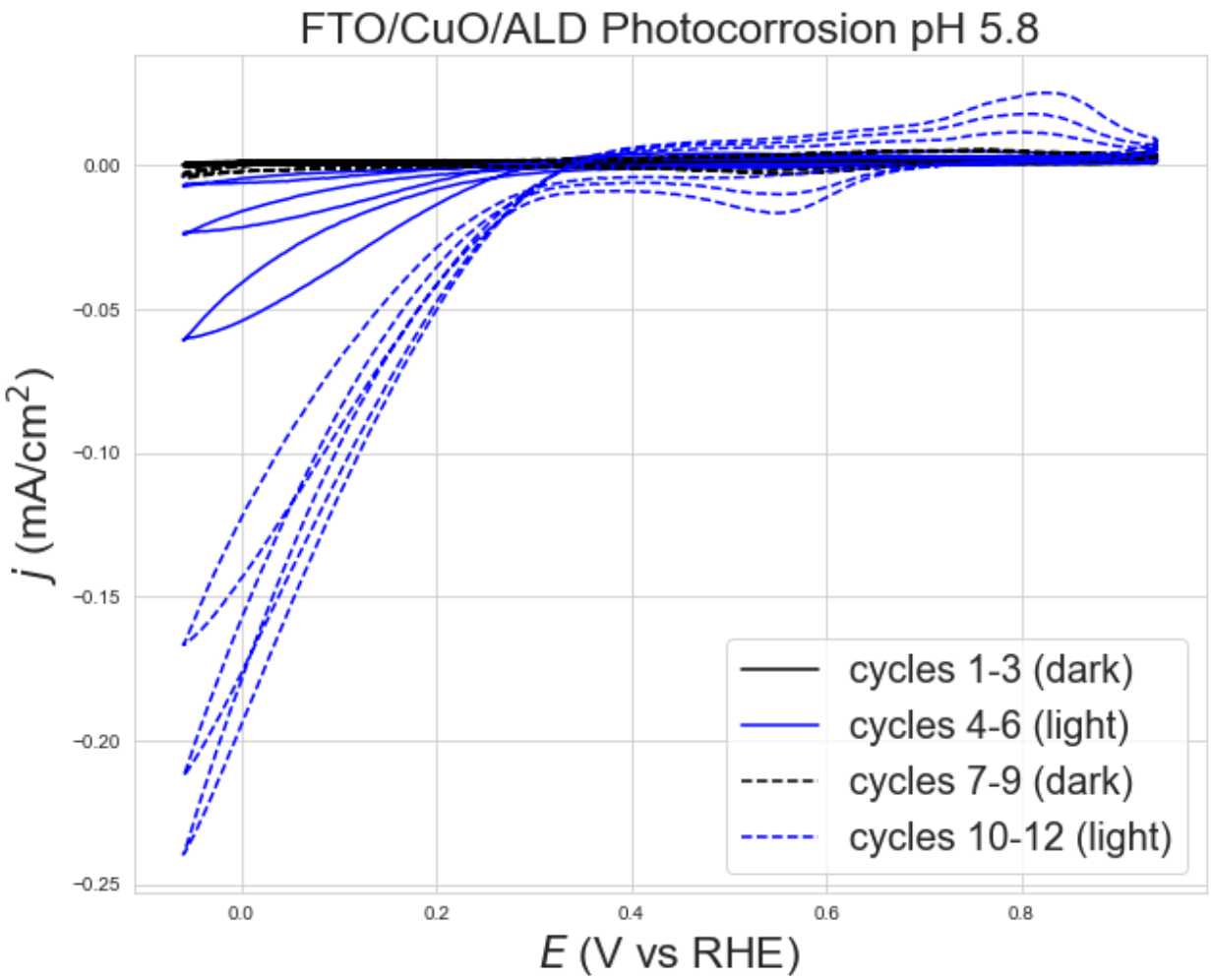

Figure 4.4. Photocorrosion not Photocatalysis: An electrode with 400nm CuO deposited with a 20nm AZO/10nm TiO2 protection layer deposited with ALD. Cyclic voltammetry sweeping cathodically first, beginning at open circuit voltage. As the electrode is cycled under illumination from a 565nm LED, current increases with successive cycles even without any catalytic assistance for performing HER. The protection layer is breaking down as cycles continue and the amount of CuO undergoing photocorrosion increases over time.

interface between CuO and the conductor intended to sweep holes to a counter electrode. Only one other study to our knowledge focuses on describing the effect of back contact workfuncton on photocatalytic performance of CuO, observing a relatively linear relationship between conductor work function and current generated, but completely neglects to mention the photocorrosion problem; thus it is uncertain if the effect encourages only photocorrosion of CuO and not HER.[126] A single study attempts to make a more complete approach by

utilizing NiO as a back contact hole collector and MoS_2 as an electron attracting catalytic and protection layer, demonstrating the importance of both in combination.[141]

4.4.2 Structural Characterization

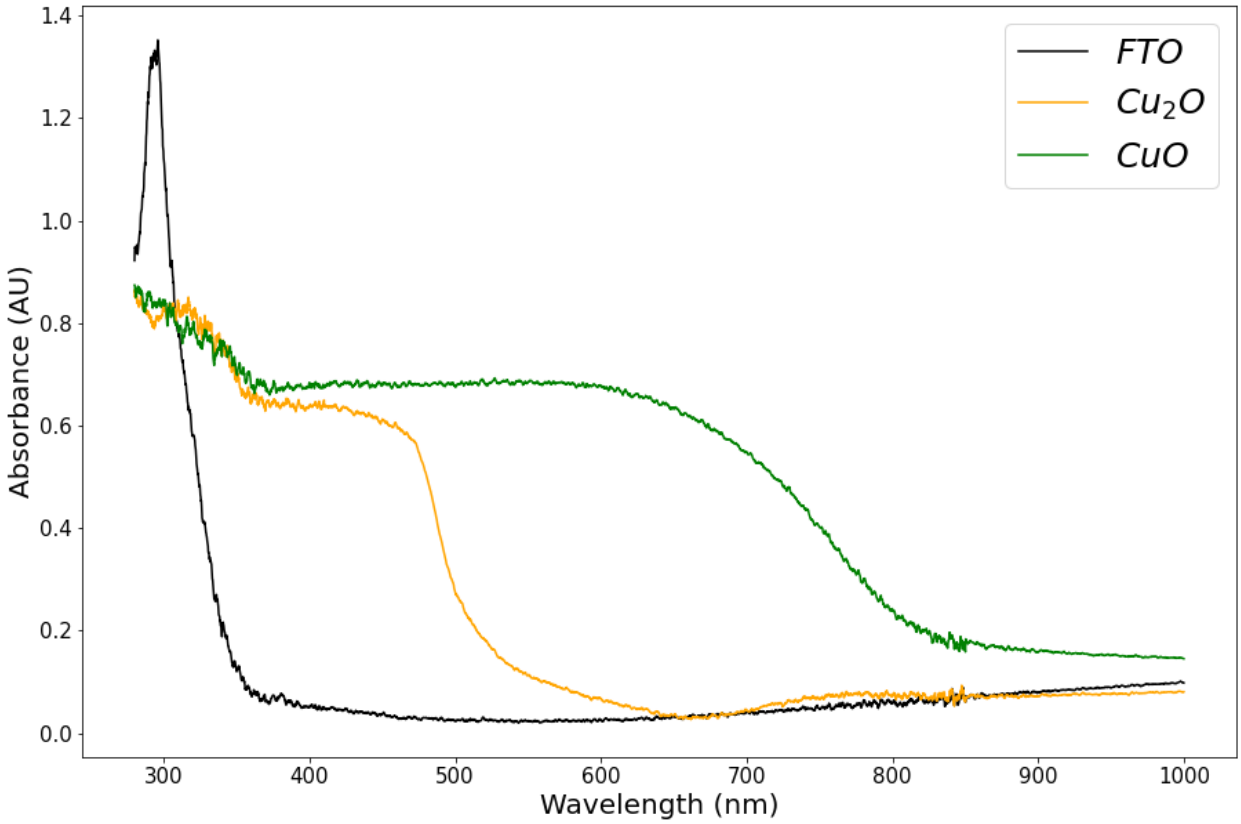

Figure 4.5 UV-vis Absorption of Copper Oxides. 400mC/cm^2 deposition of Cu_2O on FTO (orange) subsequently annealed at 500°C in air to CuO (green). Absorbance measurement is a combination of transmission spectra and reflectance spectra measured with an integrating sphere. CuO, with a smaller band gap of 1.4eV, absorbs more of the visible spectrum than Cu_2O, with a larger band gap of 2.2eV.

The UV-vis absorption spectra of Cu_2O and CuO on FTO demonstrates the significantly smaller band gap of CuO, therefore CuO absorbs a significantly larger portion of the visible spectrum (Figure 4.5). To show the layer thickness of CuO electrodes, SEM images of samples before (Figure 4.6a), and after (Figure 4.6b), annealing at 500°C were taken. There is an increase in thickness as well as roughness after annealing as the CuO unit cell is larger than Cu_2O; oxygen is forced into the film. 400mC cm^{-2} of Cu_2O deposition correspond to film

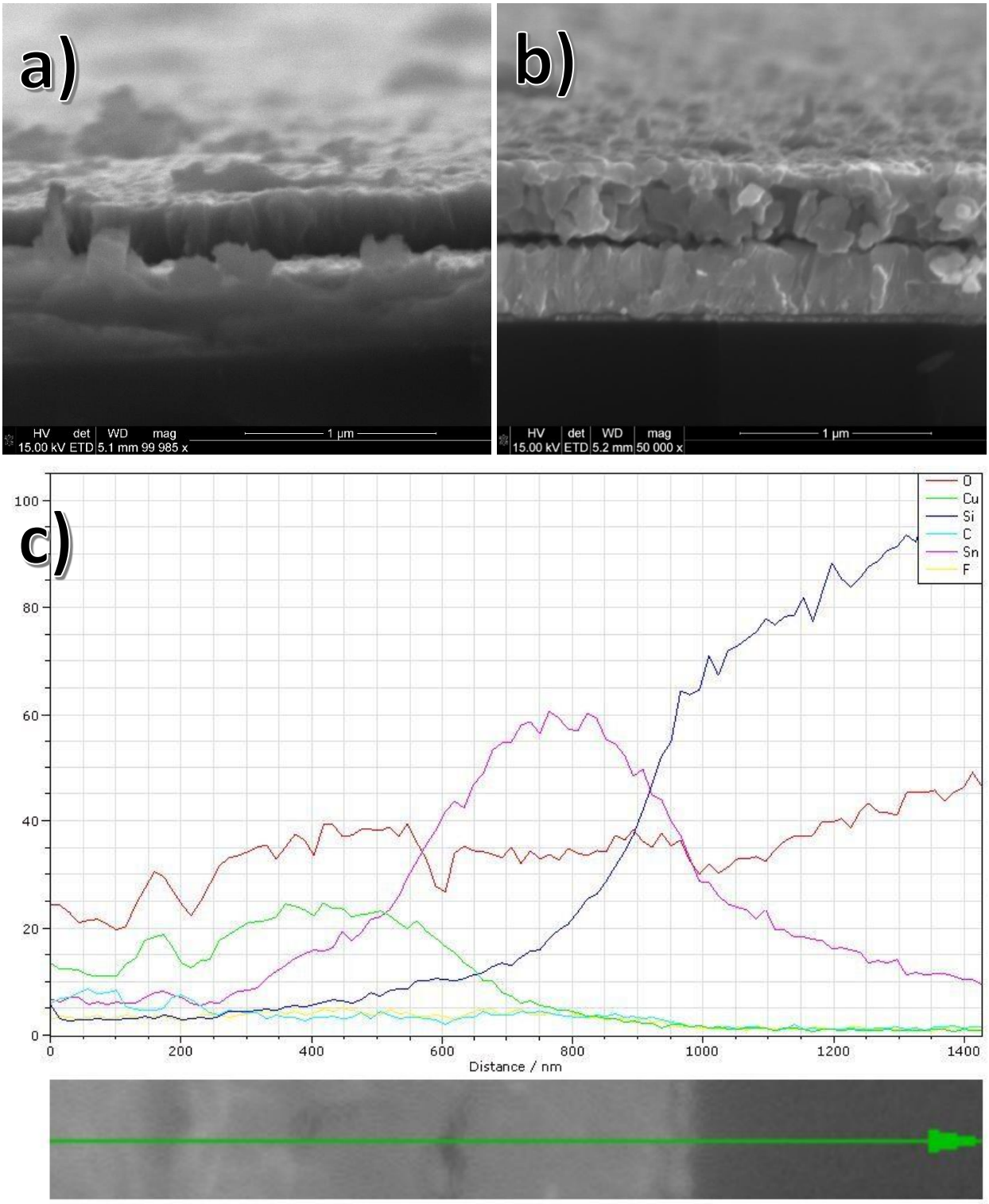

Figure 4.6. Copper Oxide Deposition Thickness: SEM of Cu_2O deposition of 400mC cm^{-2} on FTO before (a) and after annealing at 500°C (b) to CuO with an EDX scanning through the layer (c). The film thickness and film roughness increases upon annealing. Cu_2O is initially around 350nm thick, which increases to around 410nm after annealing.

thickness of about 350nm of Cu_2O, which when annealed, expands to about 410nm. Thus, in future work it is assumed that 1mC cm^{-2} is roughly equivalent to 1nm of CuO film thickness. This is the primary reason for the eventual decision to apply the ALD film after annealing to CuO; the ~30nm film is very likely to crack during the expansion process if deposited before annealing.

The need for catalytic sites suited for HER upon the surface of the electrode led us to turn to platinum, the champion HER electrocatalyst. Depositing sparse platinum across the surface in a uniform manner is necessary to directly compare a variety of electrode compositions without interfering with light absorption of the photoactive layer. The first method used to try to achieve this was galvanic replacement, which only functions on Cu_2O and not CuO. We were aware of ALD pinholes and attempted to use them to our advantage. Galvanic replacement would only occur in the pinholes and ideally would self-limit the reaction once the hole is plugged with platinum. This was not the case as Pt deposited sporadically on the surface, and where it was deposited, there were large islands of Pt in large etching spots.

A sample 100mC cm^{-2} Cu_2O protected by 10nm of TiO_2 was imaged by using reflection microcopy after 1 minute, and 5 minutes of being submerged in the platinum galvanic replacement solution. After 1 minute, sites of platinum deposition were sporadic, small, and sparse (Figure 4.7), but after 5 minutes, there were obviously larger sites of extremely sporadic deposition around the film (Figure 4.8). Most sites of deposition visually had a center speck of platinum, but a noted absence of any copper deposition left around it (Figure 4.8a&c, Figure 4.9). The galvanic replacement had created islands that were separated from any of the cuprous oxide. In particularly egregious cases, especially with thicker Cu_2O films, the deposition etched and reacted the Cu_2O out from under the TiO_2 protection layer, causing

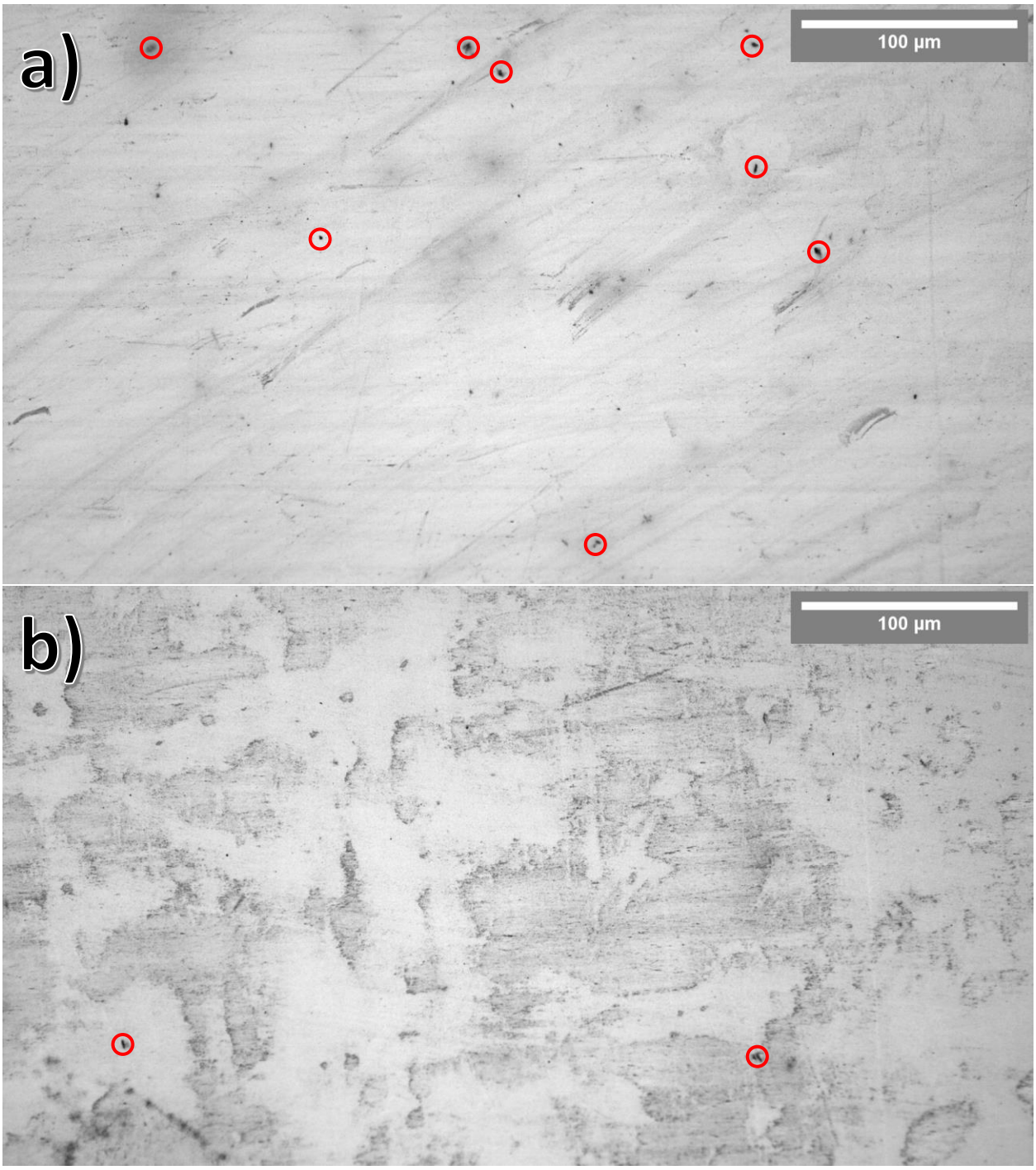

Figure 4.7. 100nm of Cu_2O after 1min of Pt Galvanic Replacement: After electrodeposition of 100mC cm^{-2} of Cu_2O on FTO, 10nm of TiO_2 was deposited via ALD. The samples were then exposed to the platinum galvanic replacement solution for 1minute. A few small, sporadic sites of Pt deposition were observed (a), some examples highlighted in red circles, but most of the surface remained as it was before Pt deposition (b).

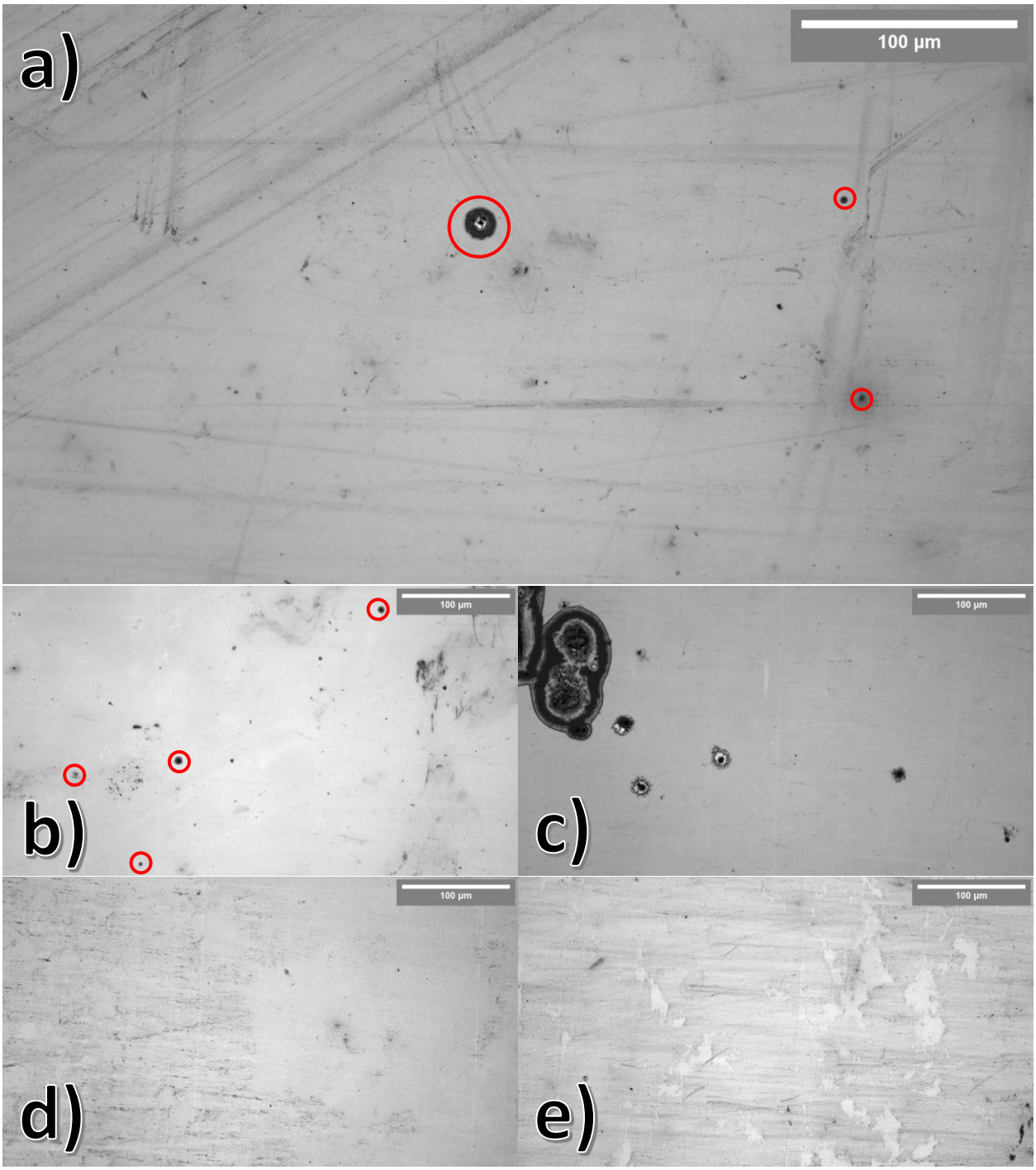

Figure 4.8. 100nm of Cu_2O after 5min of Pt Galvanic Replacement: After electrodeposition of 100mC cm^{-2} of Cu_2O on FTO, 10nm of TiO_2 was deposited via ALD. The samples were then exposed to the platinum galvanic replacement solution for 5 minutes. Most deposition sites increased in size, several highlighted in red circles (a, b). Some deposition sites formed a ring pattern with a Pt island in the center and Cu_2O being etched away around the island (a, c). In a particular case these islands became 10s of µm across and the etching of Cu_2O progressed significantly. In general the deposition was sporadic across the sample and as seen above the Pt sites varied in size significantly across the film's surface. However, most of the film had few to no deposition sites (d, e).

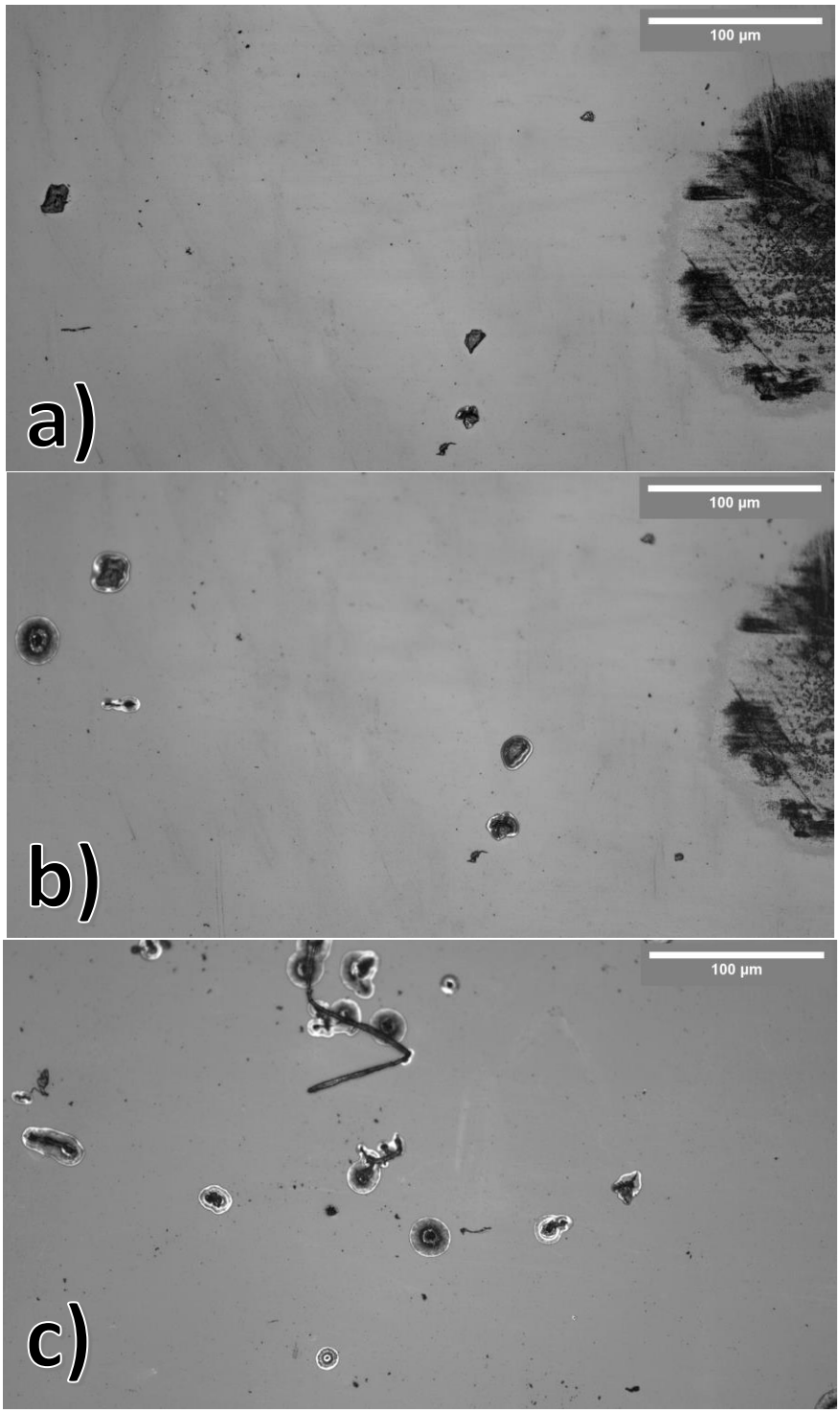

Figure 4.9. 200nm of Cu_2O after 1 & 5mins of Pt Galvanic Replacement: After electrodeposition of 200mC cm^{-2} of Cu_2O on FTO, 10nm of TiO_2 was deposited via ALD. The samples were then exposed to the platinum galvanic replacement solution for 1 minute (a) or 5 minutes (b, c). After additional deposition time, Pt sites already present grow and continue to etch the Cu_2O film, and additional sites appear (a, b). A majority of deposition sites formed a ring pattern with a Pt island in the center and Cu_2O being etched away around the island (c).

it to flake, revealing more of the underlayer to etch and react; these created large islands of Pt (Figure 4.8c, 4.9). This behavior was similarly observed in the work with protection layers in the previous chapter, especially seen in Figure 3.9. Because this method did not create uniformly dispersed platinum islands, did not help to close pinholes, and needed to be done while a protection layer was on a Cu_2O film before annealing, making the protection layer more likely to fail, this approach to platinum deposition was discarded.

The second method used to apply platinum catalytic sites on the surface of the electrode was electrodeposition.[105,140] The deposition was done after the copper was annealed and subsequently protected with 20nm of AZO and 10nm of TiO_2. Though able to provide appropriately dense platinum depositions, the process still produced somewhat sporadic distribution of platinum sites, and the harshly acidic deposition solution increased the chance of protection layer failure before the electrode could ever be used to test photoelectochemical ability. Additionally, though the current is set to be identical between depositions, some electrodes clearly have more platinum sites than others (Figure 4.10). The exact cause of this occurrence is unknown. Unfortunately, due to the catalytic sites varying in density between samples, direct comparisons could not be drawn between differing electrodes. This method too was scrapped after another method became available.

The final method considered to deposit platinum onto the surface was through utilizing a SEM sputter coater; an instrument typically used to increase the image quality of unconductive materials in SEM by reducing sample charging. The sputter coater uses a glow discharge to bombard the target metal on a sample. In this case, a platinum target was placed in the SEM sputterer and the glow discharge was applied between 60s and 300s. A study of the elemental composition of electrodes with sputtered platinum was performed using EDX and XRD to determine necessary time needed to sputter enough platinum to be catalytically active, while avoiding using too much that it coats the surface and interferes

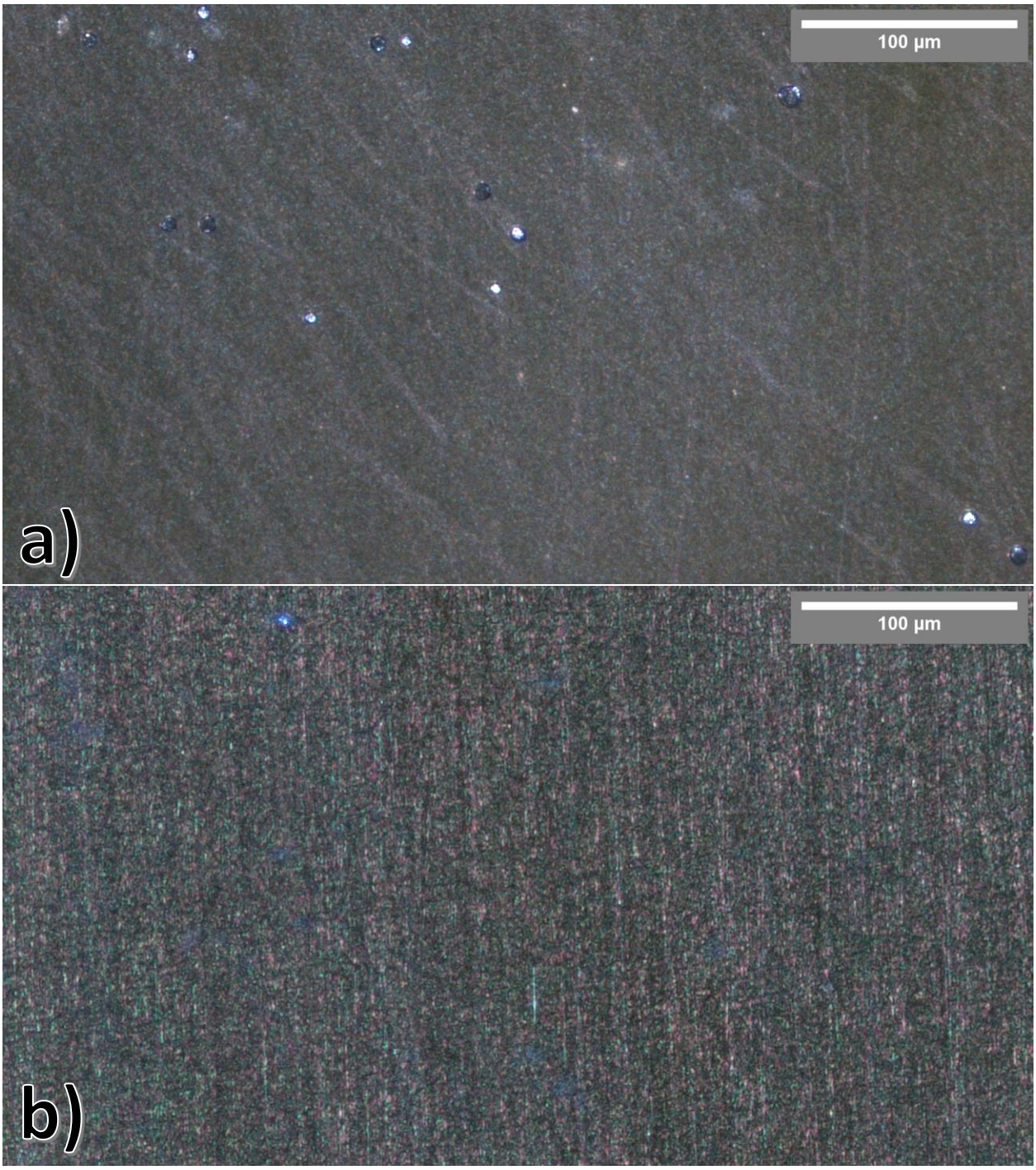

Figure 4.10 Electrodeposition of Pt on 400nm CuO Protected with ALD. 400mC cm^{-2} of Cu_2O was electrodeposited on either FTO (a) or Ni (b), which was then annealed to CuO, and coated with a protection layer of 20nm of AZO and 10nm of TiO_2 by ALD. The platinum electrodeposition occurred in an acidic solution, where -8.5µA cm^{-2} of current was applied for 15 minutes. Some samples had dense but uneven deposition (a), while others had little to no deposition at all (b), though both passed the same current during deposition. Though these are representative samples on FTO and Ni respectively, there was no pattern to which samples had good or bad depositions.

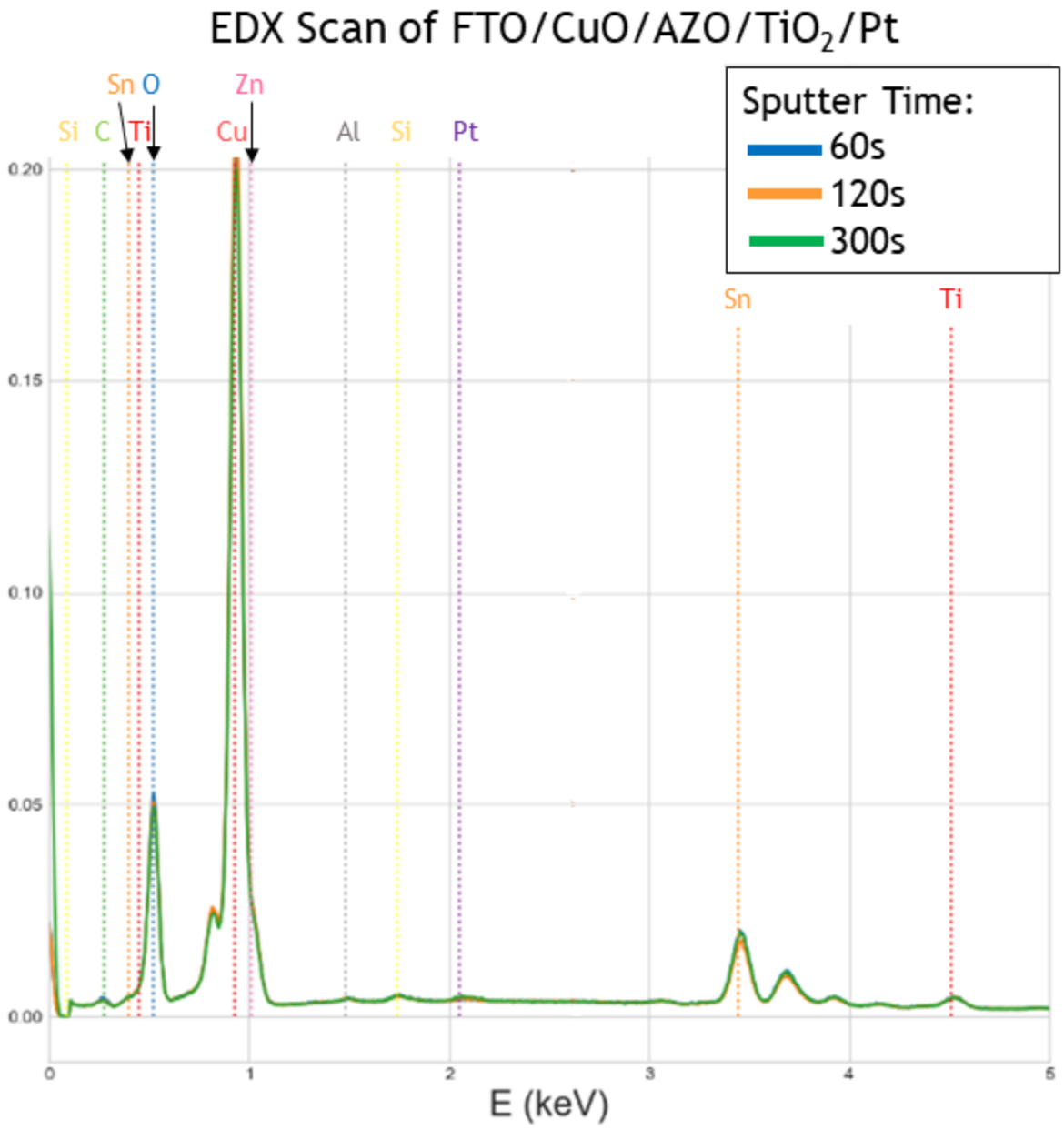

Figure 4.11. EDX of Pt Sputtered on FTO-Backed Electrode. FTO with 400nm of deposited CuO coated in 20nm of AZO and 10nm of TiO_2 was placed in the sputterer in plasma for 60s (blue line), 120s (orange line), or 300s (green line). There is a small but clear signal for Pt at all sputter times, simultaneously peaks for titanium (TiO_2), aluminum, zinc (Al:ZnO), copper (CuO), tin (FTO), and silicon (silica glass) are visible and unchanged between various Pt sputtering times.

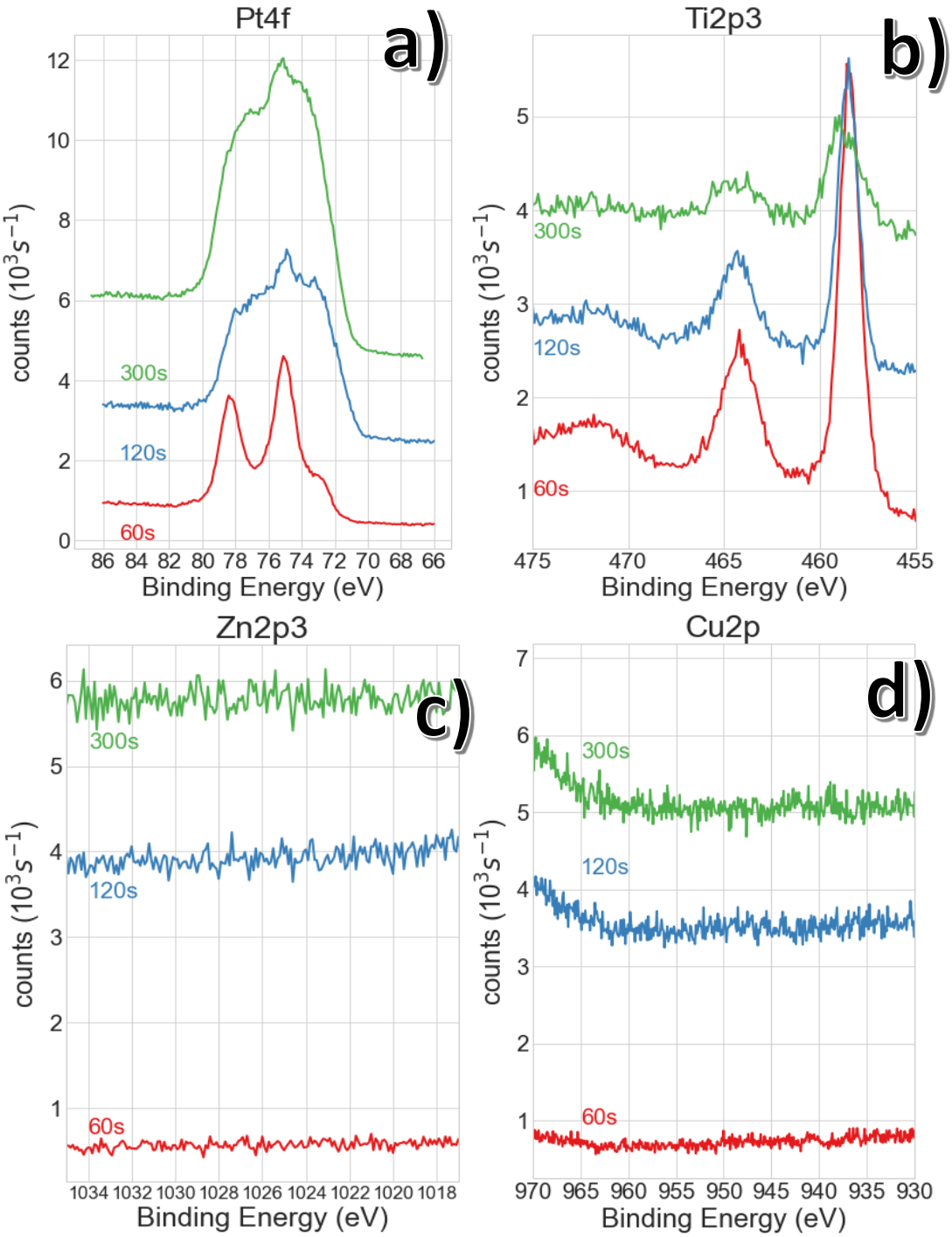

Figure 4.12. XPS of Pt Sputtered on ALD-Protected CuO Electrodes: FTO with 400nm of deposited CuO coated in 20nm of AZO and 10nm of TiO_2 was placed in the sputterer in plasma for 60s (red line), 120s (blue line), or 300s (green line). No signal is observed for zinc (c) or copper (d) in this surface sensitive technique, though titanium in the form of TiO_2 was observed, indicating the 10nm TiO_2 layer provided complete coverage of the surface. Pt signal is present in all time points of sputtering, with a variety of oxidation states of Pt present. As Pt sputtering time reaches 300s, the Ti2p3 signal decreases in intensity, indicating there is too much sputtered Pt that would interfere with the TiO_2-solution interface.

with light absorption of the cupric oxide layer. The EDX (Figure 4.11) of a full electrode on FTO (FTO/400nmCuO/20nmAZO/10nmTiO_2/ sputtered Pt) with varying platinum sputter times show that the Pt peak is quite small though visible; the presence of platinum does not decrease the strength of the other elemental signals. The same samples were also evaluated in XPS; no peaks of Cu of Zn appear in the surface-sensitive technique, demonstrating the completeness of the TiO_2 protection layer (Figure 4.12 c, d). As the time of sputtering increases, the TiO_2 signal decreases slightly between 60s and 120s, and greatly between 120s and 300s, indicative that the platinum starts to coat the surface (Figure 4.12b). The signal of Pt4f orbitals indicate that significant surface platinum is present at all sputtering time points with a variety of oxidation states present due to the plasma deposition process (Figure 4.12a). Because of a desire to get consistent platinum deposition without interfering with the TiO_2-solution interface, 120s of platinum sputtering was chosen for subsequent sample depositions.

We performed an investigation on the presence of ALD pinholes, attempting to mitigate their presence. We sought to reduce the failure rate of protected CuO electrodes during PEC measurements. This experiment adjusted the composition of protection layers and employed UV/O_3 cleaning the surface of the CuO on the electrode before ALD layers were applied. Samples of 300nm of CuO with 20nm of AZO and 10nm of TiO_2 or just the 10nm of TiO_2 were constructed, with half the samples subjected to UV/O_3 cleaning for 30 minutes between CuO annealing and the deposition of the protection layer. The finished electrodes were submerged in 0.5M sulfuric acid for 30s, and immediately rinsed with deionized water. This quick exposure was done to image the beginning of pinhole formation. A magnified image of a pinhole is shown in Figure 4.13. Figure 4.14 a-d show representative images of the surface of each variation in electrode preparation. Each image shows 3-5 points of corrosion in the field of view beginning on the surface, and scanning across the surface of these electrodes, there is no significant difference in the count or density of corrosion centers,

Figure 4.13. Protection Layer Failure Leading to CuO Corrosion. 300mC cm^{-2} of Cu_2O deposition on FTO, annealed to CuO, UV/O_3 cleaned for 30 minutes before a 20nm AZO and 10nm TiO_2 protection layer was applied via ALD. The sample was exposed to 0.5M sulfuric acid for 30 seconds and then imaged in a SEM. As the corrosion begins CuO is carved out beneath the protection layer, originating from a pinhole aberration in the protection layer. Image taken at 13000x magnification with a 15kV SEM beam.

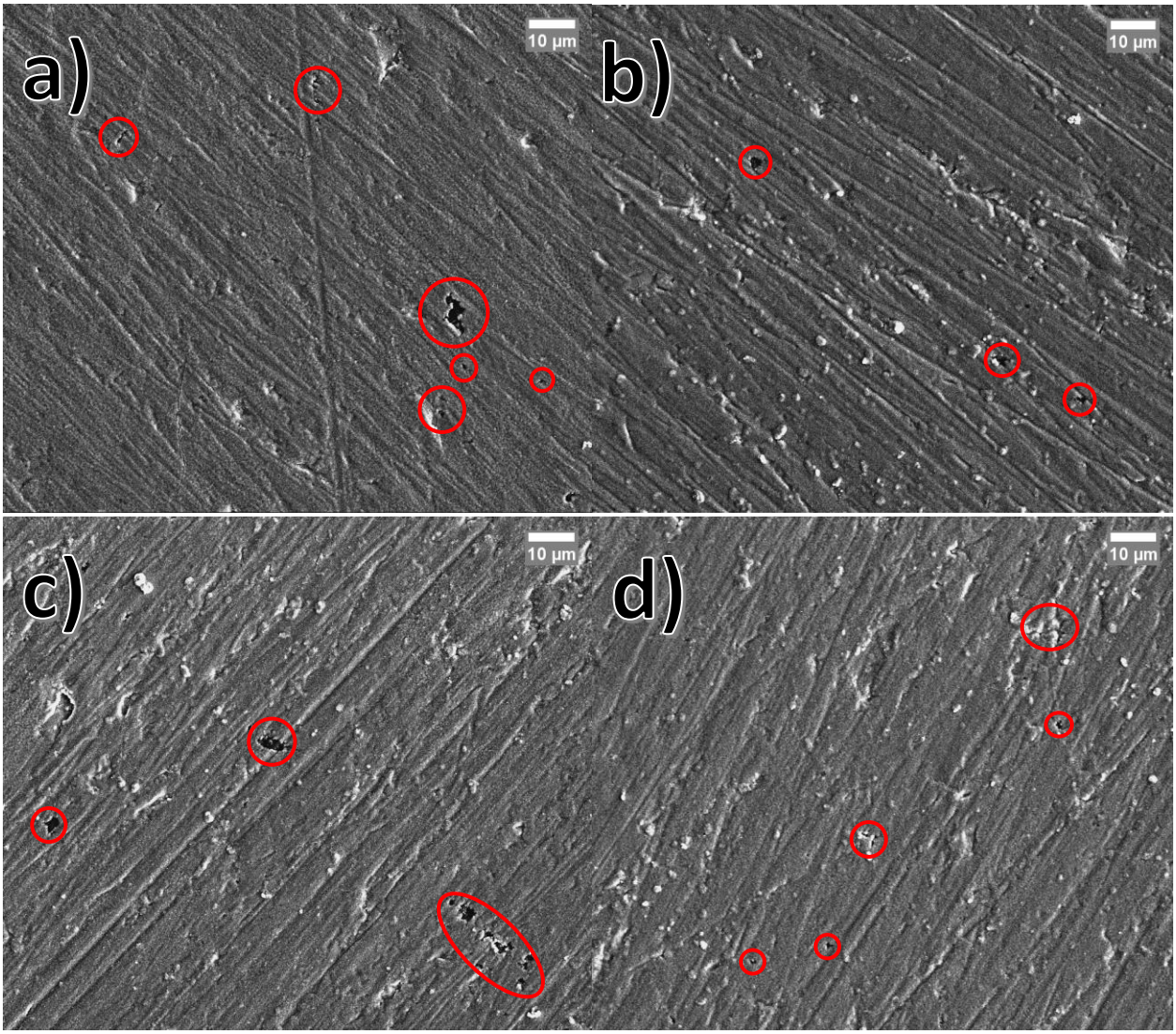

4.14 Protection Layer Failure Regardless of Preparation Method. 300mC cm^{-2} of Cu_2O deposition on FTO, annealed to CuO with a protection layer of 20nm of AZO and 10nm of TiO_2 (a & b) or only 10nm of TiO_2 (c & d) after exposed to 0.5M sulfuric acid for 30s. Sites where CuO corrosion is beginning are highlighted in red. UV/O_3 cleaning samples before ALD of protection layers (b & d) had no impact on the general number of protection failure sites compared to those that were not cleaned before deposition (a & c). Images taken at 2000x magnification with a 15kV SEM beam.

illustrating that there is no significant effect of the method of preparation we pursued upon the presence of pinholes.

In thin (<10nm) layers, pinholes mostly occur because of irregular nucleation to the surface, which generally plagues deposition of oxides on metals, so the traditional methods of adding nucleation layers to combat the problem do not apply.[86] We hypothesized that the addition of 20nm of AZO would behave akin to a buffer layer, modeled after work on Cu_2O; though it increased the chance of the protection layer working for long enough to test the electrode, in this test the observed impact on defect formation was slight.[84] Additionally, to eventually translate this work into 3-dimensional structuring, necessary to overcome CuO's Mott insulator behavior, more layers only increase production costs, manufacturing time, and potential points of failure, thus should be eliminated where possible. In thicker (>10nm) layers, extrinsic defects are due to substrate particle contamination, which can only be truly mitigated in a clean room environment, though never completely eliminated.[88,159] Increasing the thickness of deposition can eventually encase any contamination, however these contaminates can still be displaced later and yield defects.[86] The electronic resistance of the electrode also increases as the protection layer thickness increases, as most protection layers such as TiO_2 or Al_2O_3 are insulating, thus increases the applied voltage needed to generate photocurrent and decreasing energetic efficiency. At the moment there is no clear path demonstrated by the literature on how to address these critical issues for application on CuO photoelectrodes.

4.4.3 Photoelectrochemistry

During initial attempts of photoelectrochemical measurements for CuO photocathodes, we observed that direct deposition of protection layers with ALD onto both the back contact layer and the CuO layer, forms an electronic shunt path (Figure 4.14). Due

to CuO's behavior as a Mott insulator, and Al:ZnO being a transparent conducting oxide, the path of least resistance for electrons avoided CuO entirely, leading to no effect of illumination on observed current. Physical alteration of a Ni electrode by scribing and use of epoxy to isolate the ALD layer from contact with the Ni back restored light impacting observed current, though this electrode did quickly degrade from the repeated physical abrasion.

We considered reverting the choice of protection layer to TiO_2 alone, though as mentioned before, the addition of the 20nm of AZO increased the chance of a constructed electrode's protection layer lasting long enough for a CV measurement to be completed. A thicker layer of TiO_2 cold have been utilized instead, but this would increase the electronic resistance of the protection layer and thus the electrode, increasing necessary applied voltage to generate photocurrent. Adding catalytic sites encourages electron tunneling to the surface, but that begins to become unlikely and ineffective once the TiO_2 gets too thick. The solution we pursued was taping the edge of CuO deposition with Kapton tape before the deposition of the protection layers, such that the protection layer deposition was isolated to only be on top of the CuO layer (Figure 4.15).

Photoelectrochemical measurements of electrode constructions without CuO demonstrate the lack of illumination effects on the ALD layer on Ni or FTO, indicating any photoeffects on CuO electrodes is unique to the CuO layer (Figure 4.16). The presence of the ALD layer of 20nm of AZO and 10nmTiO_2 have minimal effect on the photocatalytic activity of FTO, and neither on FTO nor Ni do the ALD layers interact with 565nm light. The addition of platinum via 120s of sputtering showed catalytic activity more cathodic of -0.2V vs RHE, with similar activity seen on both FTO and Ni and being unaffected by illumination. A large oxidative peak is seen as the scan begins to sweep anodically around -0.3V vs RHE, a peak similar in position and behavior to hydrogen desorption, the process of adsorbed hydrogen

that is not going to be converted to H_2 in this cycle being expunged from the platinum similar in position and behavior to hydrogen desorption, the process of adsorbed hydrogen that is not going to be converted to H_2 in this cycle being expunged from the platinum catalytic sites,

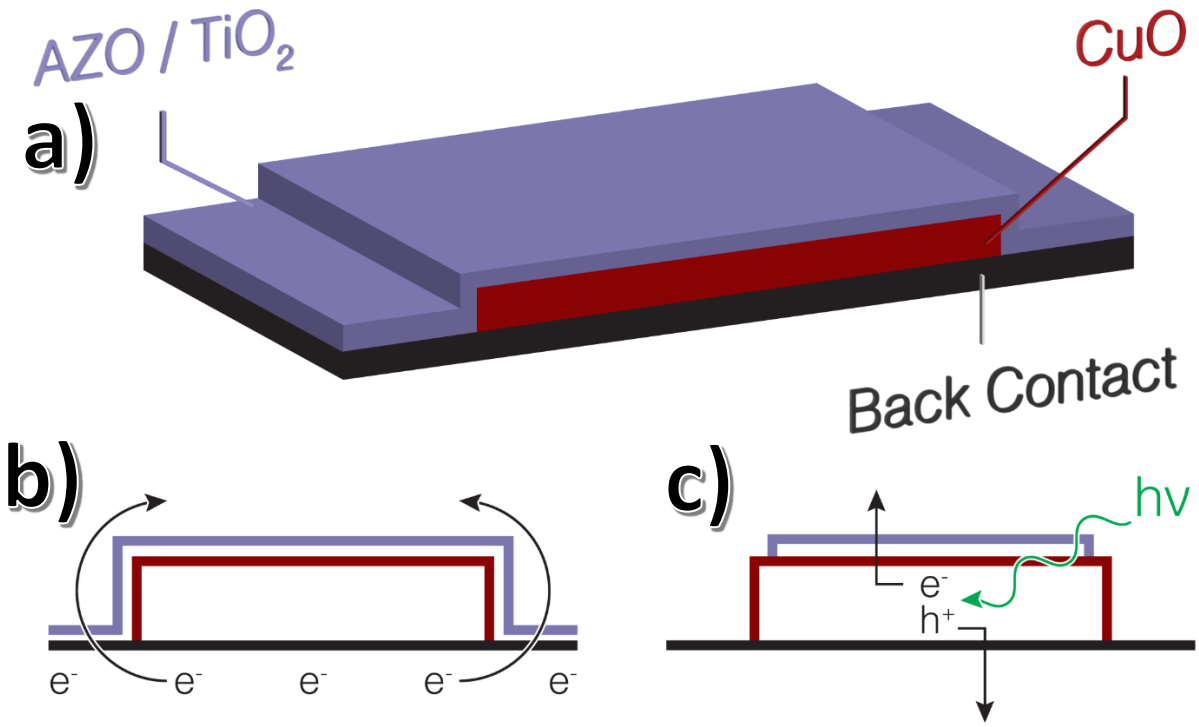

Figure 4.15 Shunt Path Formed by Protection Layer. ALD deposits the TCO protection layer across the entire available surface (purple) (a), allowing a shunt path to form, whereby electrons can flow to the surface without any interaction with the light absorption layer (red) (b). Limiting the deposition area to just the top of the CuO film with Kapton tape results causes only electrons available for reduction to be from the light absorption properties of CuO.

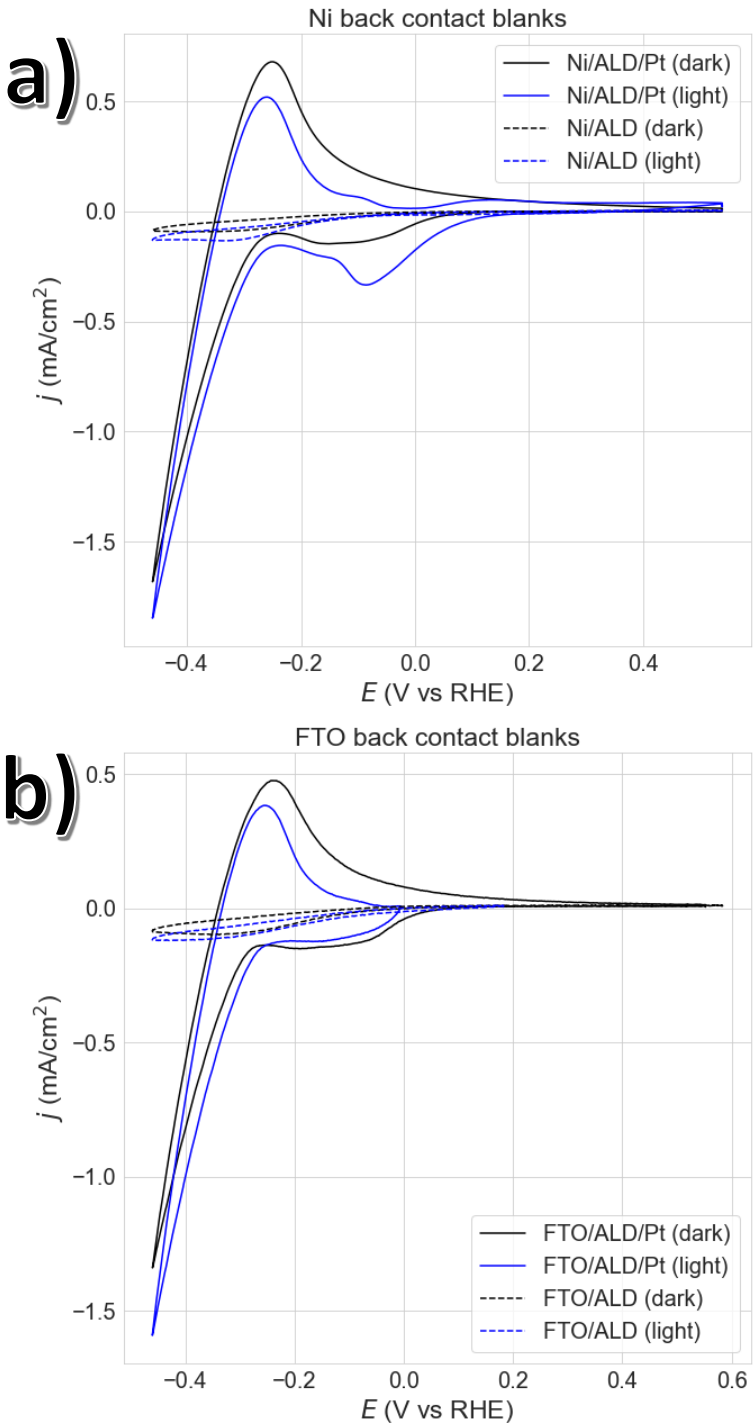

Figure 4.16 FTO and Ni Electrodes Without CuO. Cyclic voltammetry sweep at 20mV/sec in pH 5.8 0.5M sodium sulfate. Electrodes of 20nm of AZO and 10nm of TiO_2 deposited on Ni (a) and FTO (b). Those labelled as having Pt were placed in an SEM sputter coater for 120s. Scans in light are done under 565nm LED with collimating lens. Note the hydrogen desorption peak at -0.3V only present in the samples with Pt, indicative of hydrogen reduction occurring in the cathodic sweep. Illumination does not significantly interact with the ALD layers or Pt catalytic sites.

indicative that the current seen is due to hydrogen ion reduction.[160,161]

Cyclic voltammetry on electrodes prepared with CuO layers were normally scanned to -0.6V vs Ag/AgCl (-0.06V *vs* RHE), or at most -0.8V vs Ag/AgCl (-0.26 V *vs* RHE) when no apparently catalytic activity under illumination was observed initially, if the electrode was stable enough to test that aggressively. In Figure 4.17a the only sample condition with significant current density is the illuminated, protected CuO electrode deposited on a Ni back contact. Additionally, this sample in the cathodic sweep presented the characteristic hydrogen desorption peak present when Pt is reducing hydrogen. Figure 4.17b presents an inset highlighting the lack of current in other samples of protected CuO, whether on Ni or FTO, without or with the presence of sputtered Pt, in illumination and dark. The only significant exception being the protected CuO sample of FTO without Pt, which quickly dissolved in subsequent cycles of testing, indicating most of the current observed in that sample under illumination is photocorrosion.

Subsequent cycling of the exemplary electrode from Figure 4.17a is shown in Figure 4.18, alternating between testing in dark and under illumination. The peak current in at -0.6 V vs Ag/AgCl increases with each subsequent cycle under illumination. After 3 cycles under illumination, the next cycles completed without illumination begin to show signs of a comprimised protection layer, thus the increase in current is an effect of a combination of HER and CuO photodissolution. The same sample, upon being subjected to a chronoamperometry with a current set to 1mA/cm^2, quickly fails (Figure 4.19). Though exchanging the back contact for Ni in this case showed marked improvement on the temporary photocathodic performance of the electrode, it did little to increase its longeveity.

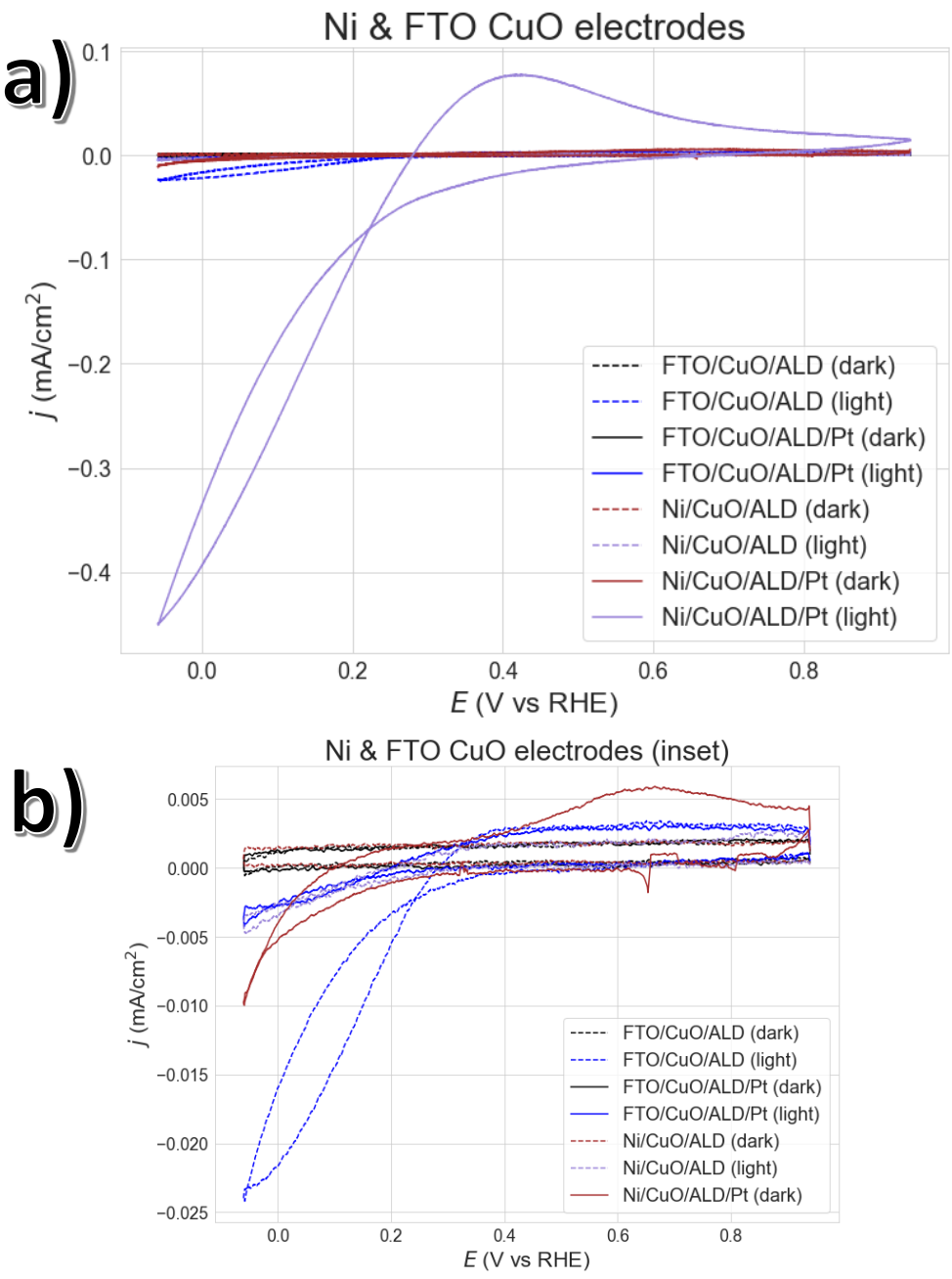

Figure 4.17 Photoelectrochemistry of CuO Electrodes on Ni & FTO. Cyclic voltammetry sweep at 20mV/sec in pH 5.8 0.5M sodium sulfate. ALD protection layers of 20nm of AZO and 10nm of TiO_2 deposited on 300nm of CuO. Those labelled as having Pt were placed in an SEM sputter coater for 120s. Scans in light are done under 565nm LED with collimating lens. Significant current is only observed when light is shown on protected CuO is deposited on Ni, provided with Pt catalytic sites (a). An inset of the same sample set without the illuminated Ni/CuO/ALD/Pt electrode shows the analogous FTO electrode had minimal photocurrent at these potentials (b). The outlier of FTO/CuO/ALD without catalytic Pt began to show signs of CuO photocorrosion; the same sample was used in Figure 4.4 as a clear example of dissolution.

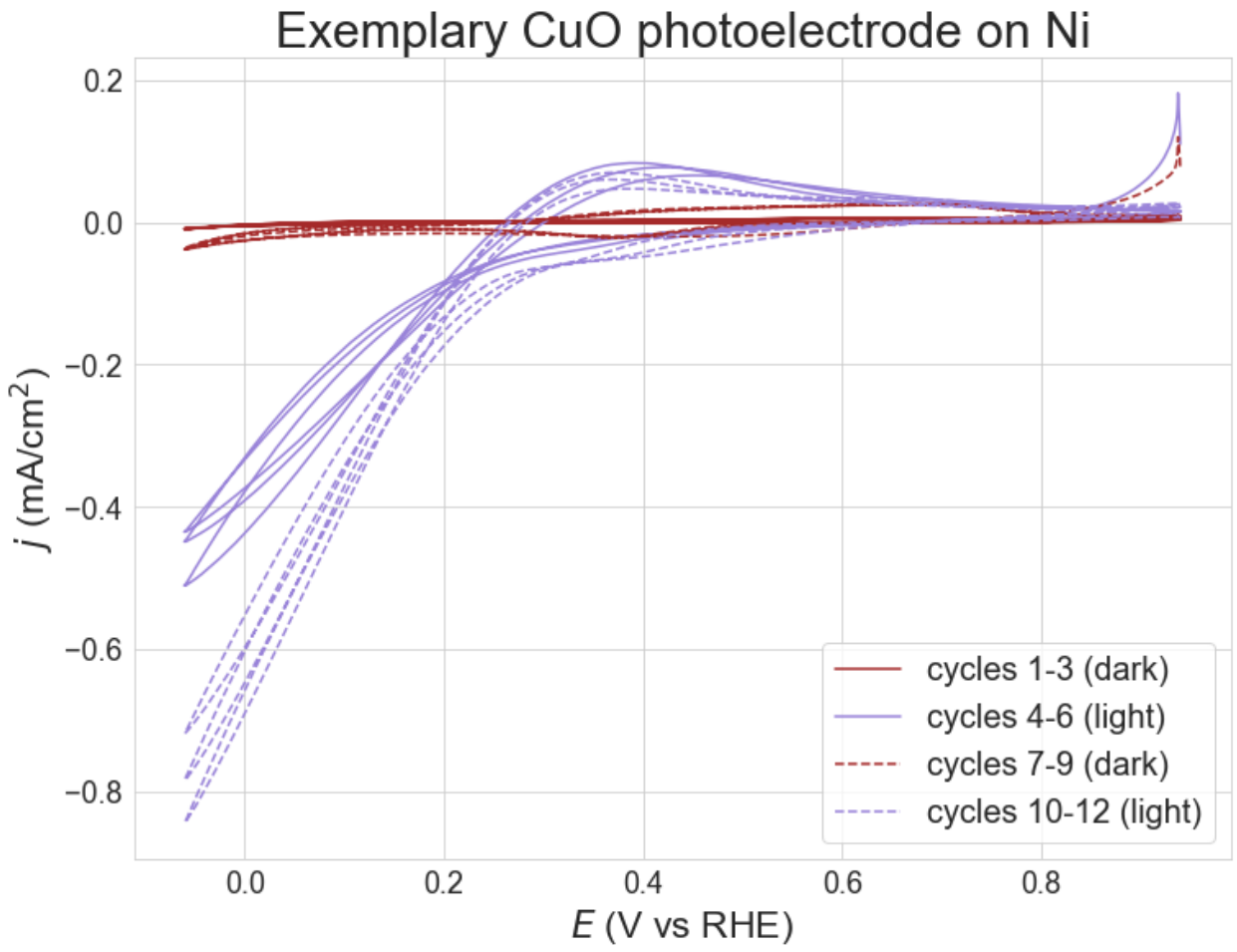

Figure 4.18 Photoelectrochemistry of a Protected CuO Electrode on Ni. Cyclic voltammetry sweep at 20mV/sec in pH 5.8 0.5M sodium sulfate. ALD protection layers of 20nm of AZO and 10nm of TiO_2 deposited on 300nm of CuO, after which Pt was applied in an SEM sputter coater for 120s. Scans in light are done under 565nm LED with collimating lens. Increases in maximum current density is observed in each subsequent cycling under illumination, indicating the beginnings of protection layer failure. The 7^{th}-9^{th} cycles, done without illumination, also begin to demonstrate signs of CuO_x red/ox cycling indicative of corrosion.

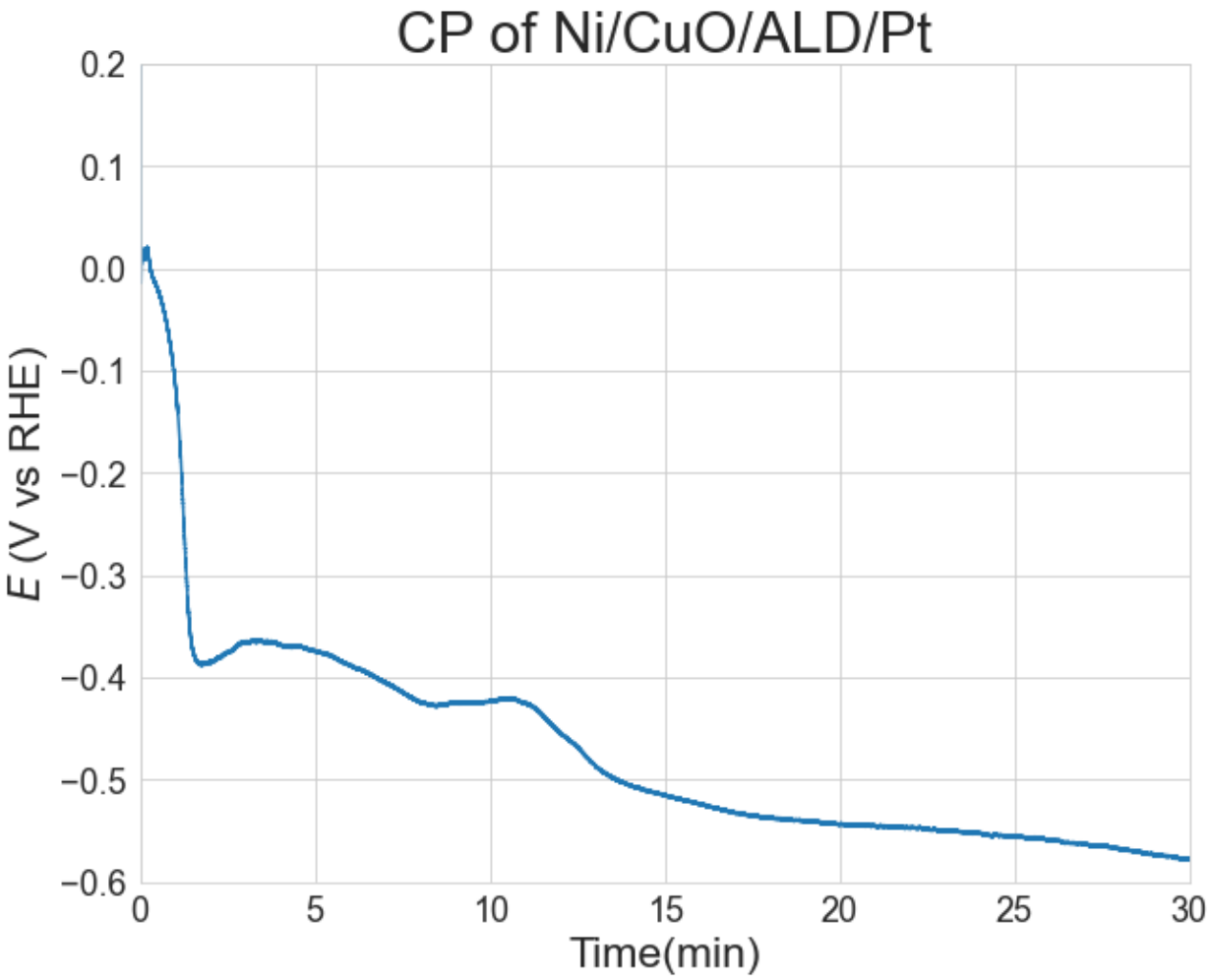

Figure 4.19 Photoelectrochemistry of a Protected CuO Electrode on Ni. Chronopotentiometry with a set current of 1mA cm^{-2}. ALD protection layers of 20nm of AZO and 10nm of TiO_2 deposited on 300nm of CuO, after which Pt was applied in an SEM sputter coater for 120s. Measured under illumination from 565nm LED with collimating lens. The voltage needed to maintain the set current dramatically spiked quickly as the electrode began to fail and increased further once the last of the CuO had been dissolved from the Ni electrode.

Repeating the same manufacturing methods, electrodes were constructed on silver, a metal with a workfunction of 4.7eV. As seen in Figure 4.20, unprotected silver electrodes signal large oxidation and reduction peaks around 0.8V vs RHE. Upon ALD protection of silver, those peaks disappear as no silver is interacting with the solution. Protected CuO on Ag without platinum deposition is only marginally affected by illumination. There is a clear but small photoeffect on protected CuO on Ag with sputtered platinum, but the effect is tiny when compared to the effect when the same electrode is constructed on nickel (Figure 4.21). For direct comparison, the electrode on silver had a current density of -0.14mA/cm^2 at -0.6V vs Ag/AgCl, while the same electrode on Ni at the same potential had a current density of -0.45mA/cm^2. More importantly, the current of the electrode on silver before illumination is much larger than on nickel, the impact of illumination on nickel provides a several fold increase in current rather than a meager 40μA cm^{-2}.

We have shown that when CuO is able to be isolated from the solution, two back contacts, silver and FTO, with workfunctions above the fermi energy of CuO, have minimal photocathodic behavior. However, a back contact with a workfunction almost equal to the fermi energy, nickel, has significant photoactivity. The sample size of electrodes must be large enough during manufacturing to discover exemplary electrodes that are stable long enough to go through electrochemical testing. ALD protection layers are promising in many applications, but are not adequate enough for use in the unique set of circumstances surrounding CuO; specifically, its propensity for self-induced photoreduction, its Mott resistor behavior, and the near indistinguishable overlap of photocorrosion and photocathodic electrochemical signals.

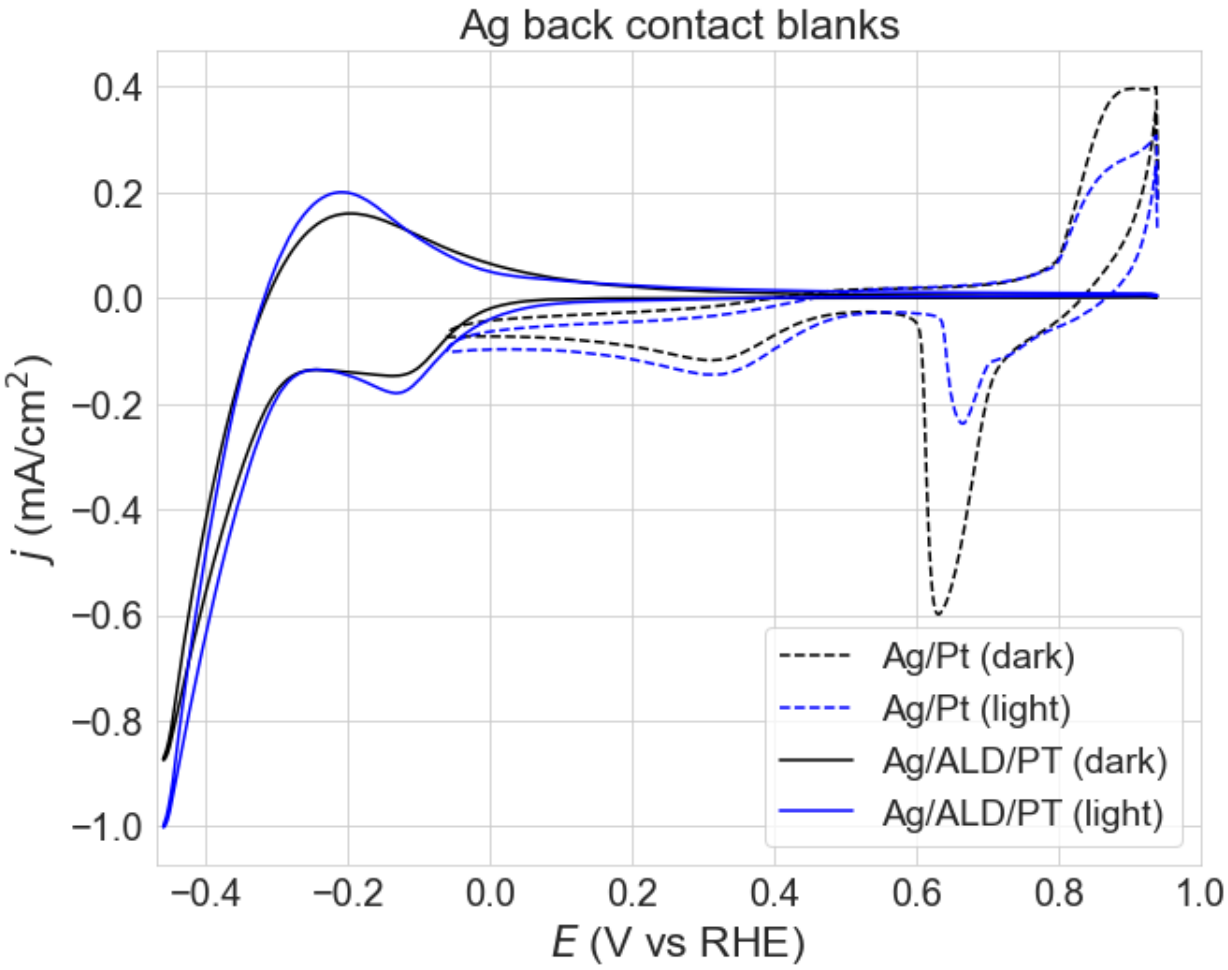

Figure 4.20 Ag Electrodes Without CuO. Cyclic voltammetry sweep at 20mV/sec in pH 5.8 0.5M sodium sulfate. Electrodes of polished silver sputtered with Pt for 120s in an SEM sputter coater. ALD protection layers of 20nm of AZO and 10nm of TiO_2 deposited. Scans in light are done under 565nm LED with collimating lens. The scans of unprotected Ag show large silver oxidation and reduction peaks around 0.8V vs RHE, along with a Pt reduction peak around 0.3V vs RHE. Once ALD layers were applied, the silver red/ox peaks were suppressed as silver was no longer in contact with the solution. The protected electrode with Pt has similar current densities and shape to analogous electrodes on Ni and FTO as seen in Figure 4.15.

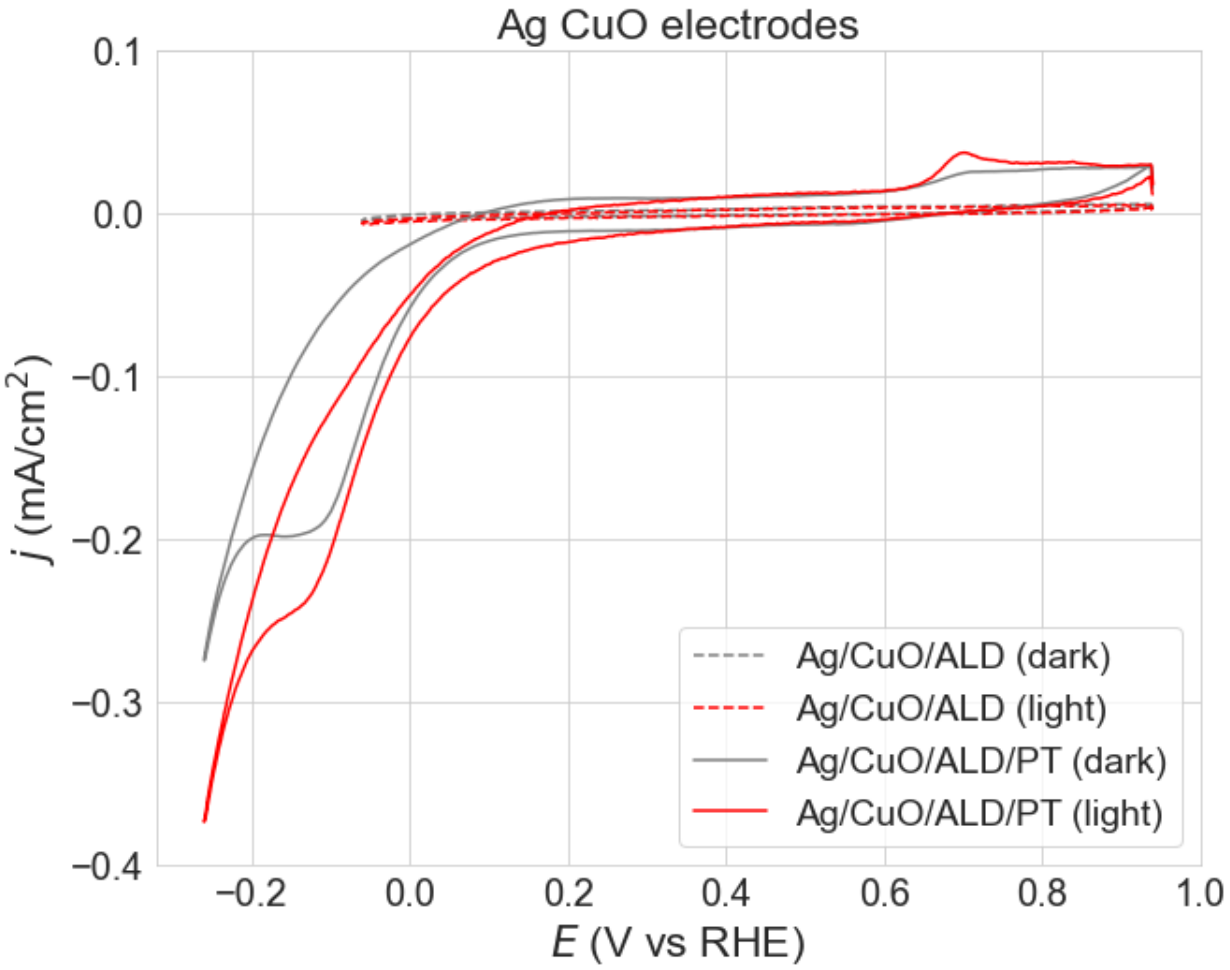

Figure 4.21 Photoelectrochemistry of CuO Electrodes on Ag. Cyclic voltammetry sweep at 20mV/sec in pH 5.8 0.5M sodium sulfate. ALD protection layers of 20nm of AZO and 10nm of TiO_2 deposited on 300nm of CuO. Those labelled as having Pt were placed in an SEM sputter coater for 120s. Scans in light are done under 565nm LED with collimating lens. The effect of illumination on electrodes with Pt is small, with only increasing current 40μA cm^{-2} at 0.00V vs RHE when comparing dark and illuminated samples.

4.5 Conclusion

We presented cupric oxide as potential semiconductor in a photocathode for PEC hydrogen generation from water splitting. The Mott-insulator behavior of CuO was not addressed as we proposed it as a candidate for future three-dimensional structuring. However, to be utilized in a functional electrode, two important factors must be met; separation of CuO from the water in a photoelectrochemical system, and conductor with a workfunction at or below 5.3eV. To be in a hierarchically three-dimensional electrode, ideally the back contact would be a transparent conducting oxide akin to AZO or ITO; but a p-type TCO must be developed for this purpose, and none are readily available for ALD. Atomic layer deposition is theoretically ideal for deposition of both the transparent conductor and protection layers in a particularly tortuous structure. But as demonstrated here, and elsewhere in literature, pinhole defects continue to be a crippling problem plaguing ALD protection layers that have no complete solution, only some methods of mitigation. Until both a p-type TCO and the problem of pinholes are addressed, CuO has no hope of becoming a reasonable photocathode for photoelectrochemical water splitting.

Chapter 5. Conclusion

In this work, we successfully protected AZO from extreme pH environments with ALD-TiO_2. The same protection layer, even after deposition of an AZO buffer layer, did not consistently protect CuO from photodissolution, even in relatively pH neutral environments. The presence of pinholes in the ALD protection layer, even after surface cleaning, caused us to be unable to predict which CuO PEC device replicates would remain stable long enough to perform cursory PEC testing. ALD has been lauded for its ability to deposit thin, conformal films, and it can do so without defects in certain conditions, albeit those conditions are yet to be consistently established. A consistent method for eliminating ALD pinholes has yet to be reported in the literature. The propensity of CuO to rapidly photocorrode in reductive conditions demands that a protection layer be flawless, an expectation not yet predictable with ALD films.

The effects of the workfunction upon CuO PEC device performance shown in Chapter 4 were replicable. Due to the nature of pinholes forming in ALD protection layers, exemplary electrodes were difficult to produce consistently. Many otherwise identical samples with pinholes, the presence of which was impossible to determine until the completed electrode corroded under illumination, hampered efforts to proceed forward. Nevertheless, as clearly demonstrated here, the impact of back contact energetics cannot be ignored in the conceptualization and construction of PEC devices. The relation between the fermi energy of the semiconductor and back contact is just as important as band position and chemical potential at the semiconductor-liquid interface. In not ensuring Ohmic contact at the solid interface, charge separation within the semiconductor can be impeded, which increases energy losses to recombination of electron-hole pairs. This is especially detrimental to a Mott insulator like CuO which already has a propensity for low charge carrier mobility.

We did not get to construct a working hierarchically structured PEC device, as was the intention when this work began. The tortuous nature of the proposed scaffold mentioned in Chapter 1 necessitates the deposition of the protection layer for a light absorber in the to be done with ALD. As stated previously, the workfunction of the back contact must be equal to or lower than the fermi energy of CuO. A current collector within a three-dimensional scaffold must be transparent to minimize parasitic absorption losses. No prevalent TCO has yet been developed with a workfunction deep enough to maintain Ohmic contact with CuO, and for that matter, most p-type semiconductors. A p-type TCO must be developed before a photocathode could be constructed within a tortuous scaffold. As a result of the Mott insulator behavior of CuO, reasonable solar-to-hydrogen conversion efficiencies cannot be reached without three-dimensional structuring.

The scaffold should not be abandoned however, as hematite (α-Fe_2O_3) shares the Mott insulating properties of CuO, is a n-type semiconductor, and is significantly more stable in aqueous environments than CuO. As a photoanode, the band gap of hematite of 2.0eV is appropriate for pairing with a much smaller band gap photocathode. ALD-AZO or ITO could be viable for making Ohmic contact with hematite and any protection layer theoretically should not have to be as uniformly aberration-free. An obstacle to this, likely the subject of future work, is the deposition of hematite. ALD α-Fe_2O_3 cannot yet be directly deposited, and as brought up by Wang et al. any annealing in air needed to convert ALD FeO_x to hematite would cause AZO to become unconductive.[162] Alternative ALD chemistry or resolving the cause of unpredictable behavior of ALD protection layers could make a hierarchically structured earth abundant photoelectrode viable for PEC water splitting.

Bibliography

1. Conti J, Holtberg P, Diefenderfer J, LaRose A, Turnure JT, Westfall L. *International energy outlook 2016 with projections to 2040*. 2016.

2. Sadorsky P. Renewable energy consumption and income in emerging economies. *Energy policy*. 2009;37(10):4021-4028.

3. Lewis NS, Nocera DG. Powering the planet: Chemical challenges in solar energy utilization. *Proceedings of the National Academy of Sciences*. 2006;103(43):15729-15735.

4. Tsao J, Lewis N, Crabtree G. Solar faqs. *US department of Energy*. 2006;

5. Gowrisankaran G, Reynolds SS, Samano M. Intermittency and the value of renewable energy. *Journal of Political Economy*. 2016;124(4):1187-1234.

6. Armand M, Tarascon JM. Building better batteries. *Nature*. 02/06/online 2008;451:652. doi:10.1038/451652a

7. Blankenship RE, Tiede DM, Barber J, et al. Comparing photosynthetic and photovoltaic efficiencies and recognizing the potential for improvement. *science*. 2011;332(6031):805-809.

8. Walker DA. Biofuels, facts, fantasy, and feasibility. *Journal of Applied Phycology*. 2009;21(5):509-517.

9. Barton EE, Rampulla DM, Bocarsly AB. Selective Solar-Driven Reduction of CO2 to Methanol Using a Catalyzed p-GaP Based Photoelectrochemical Cell. *Journal of the American Chemical Society*. 2008/05/01 2008;130(20):6342-6344. doi:10.1021/ja0776327

10. Liang L, Lei F, Gao S, et al. Single Unit Cell Bismuth Tungstate Layers Realizing Robust Solar CO2 Reduction to Methanol. *Angewandte Chemie International Edition*. 2015/11/16 2015;54(47):13971-13974. doi:10.1002/anie.201506966

11. Staykov A, Lyth SM, Watanabe M. Photocatalytic Water Splitting. In: Sasaki K, Li H-W, Hayashi A, Yamabe J, Ogura T, Lyth SM, eds. *Hydrogen Energy Engineering: A Japanese Perspective*. Springer Japan; 2016:159-174.

12. Pinaud BA, Benck JD, Seitz LC, et al. Technical and economic feasibility of centralized facilities for solar hydrogen production via photocatalysis and photoelectrochemistry. *Energy & Environmental Science*. 2013;6(7):1983-2002.

13. Norman MA, Perez WL, Kline CC, Coridan RH. Enhanced Photoelectrochemical Energy Conversion in Ultrathin Film Photoanodes with Hierarchically Tailorable Mesoscale Structure. *Advanced Functional Materials*. 2018;28(29):1800481.

14. Hagfeldt A, Boschloo G, Sun L, Kloo L, Pettersson H. Dye-sensitized solar cells. *Chemical reviews*. 2010;110(11):6595-6663.

15. Shaner MR, Fountaine KT, Ardo S, Coridan RH, Atwater HA, Lewis NS. Photoelectrochemistry of core–shell tandem junction n–p+-Si/n-WO 3 microwire array photoelectrodes. *Energy & Environmental Science*. 2014;7(2):779-790.

16. Walter MG, Warren EL, McKone JR, et al. Solar Water Splitting Cells. *Chemical Reviews*. 2010/11/10 2010;110(11):6446-6473. doi:10.1021/cr1002326

17. Coridan RH, Shaner M, Wiggenhorn C, Brunschwig BS, Lewis NS. Electrical and photoelectrochemical properties of WO3/Si tandem photoelectrodes. *The Journal of Physical Chemistry C*. 2013;117(14):6949-6957.

18. Zhang L, Reisner E, Baumberg JJ. Al-doped ZnO inverse opal networks as efficient electron collectors in BiVO 4 photoanodes for solar water oxidation. *Energy & Environmental Science*. 2014;7(4):1402-1408.

19. Coridan RH, Norman MA, Mehrabi H. Enhanced light absorption in simulations of ultra-thin ZnO layers structured by a SiO2 photonic glass. *Canadian Journal of Chemistry*. 2018;96(11):969-973.

20. George SM. Atomic Layer Deposition: An Overview. *Chemical Reviews*. 2010/01/13 2010;110(1):111-131. doi:10.1021/cr900056b

21. Rajeshwar K. Fundamentals of semiconductor electrochemistry and photoelectrochemistry. *Encyclopedia of electrochemistry*. 2007;6:1-53.

22. Rühle S. Tabulated values of the Shockley–Queisser limit for single junction solar cells. *Solar Energy*. 2016;130:139-147.

23. Grätzel M. Photoelectrochemical cells. *nature*. 2001;414(6861):338.

24. Cao S, Piao L, Chen X. Emerging Photocatalysts for Hydrogen Evolution. *Trends in Chemistry*. 2020/01/01/ 2020;2(1):57-70. doi:https://doi.org/10.1016/j.trechm.2019.06.009

25. Fujishima A, Honda K. Electrochemical Photolysis of Water at a Semiconductor Electrode. *Nature*. 1972/07/01 1972;238(5358):37-38. doi:10.1038/238037a0

26. Tilley SD. Recent advances and emerging trends in photo-electrochemical solar energy conversion. *Advanced Energy Materials*. 2019;9(2):1802877.

27. Sathre R, Scown CD, Morrow WR, et al. Life-cycle net energy assessment of large-scale hydrogen production via photoelectrochemical water splitting. *Energy & Environmental Science*. 2014;7(10):3264-3278.

28. Liu J, Liu Y, Liu N, et al. Metal-free efficient photocatalyst for stable visible water splitting via a two-electron pathway. *Science*. 2015/02/27 2015;347(6225):970-974. doi:10.1126/science.aaa3145

29. Zhai P, Haussener S, Ager J, et al. Net primary energy balance of a solar-driven photoelectrochemical water-splitting device. *Energy & Environmental Science*. 2013;6(8):2380-2389.

30. Sathre R, Greenblatt JB, Walczak K, et al. Opportunities to improve the net energy performance of photoelectrochemical water-splitting technology. *Energy & Environmental Science*. 2016;9(3):803-819.

31. Bolton JR. Solar Fuels: The production of energy-rich compounds by the photochemical conversion and storage of solar energy. *Science*. 1978;202(4369):705-711.

32. Bolton JR, Strickler SJ, Connolly JS. Limiting and realizable efficiencies of solar photolysis of water. *Nature*. 1985;316(6028):495-500.

33. Hu S, Xiang C, Haussener S, Berger AD, Lewis NS. An analysis of the optimal band gaps of light absorbers in integrated tandem photoelectrochemical water-splitting systems. 10.1039/C3EE40453F. *Energy & Environmental Science*. 2013;6(10):2984-2993. doi:10.1039/C3EE40453F

34. Moon C, Shin B. Review on light absorbing materials for unassisted photoelectrochemical water splitting and systematic classifications of device architectures. *Discover Materials*. 2022/05/23 2022;2(1):5. doi:10.1007/s43939-022-00026-2

35. Cheng W-H, Richter MH, May MM, et al. Monolithic photoelectrochemical device for direct water splitting with 19% efficiency. *ACS Energy Letters*. 2018;3(8):1795-1800.

36. Young JL, Steiner MA, Döscher H, France RM, Turner JA, Deutsch TG. Direct solar-to-hydrogen conversion via inverted metamorphic multi-junction semiconductor architectures. *Nature Energy*. 2017;2(4):1-8.

37. Chen S, Wang L-W. Thermodynamic oxidation and reduction potentials of photocatalytic semiconductors in aqueous solution. *Chemistry of Materials*. 2012;24(18):3659-3666.

38. Katz JE, Zhang X, Attenkofer K, et al. Electron small polarons and their mobility in iron (oxyhydr) oxide nanoparticles. *Science*. 2012;337(6099):1200-1203.

39. Iandolo B, Wickman B, Zorić I, Hellman A. The rise of hematite: origin and strategies to reduce the high onset potential for the oxygen evolution reaction. *Journal of Materials Chemistry A*. 2015;3(33):16896-16912.

40. Le Formal F, Tetreault N, Cornuz M, Moehl T, Grätzel M, Sivula K. Passivating surface states on water splitting hematite photoanodes with alumina overlayers. *Chemical Science*. 2011;2(4):737-743.

41. Bak T, Nowotny J, Rekas M, Sorrell CC. Photo-electrochemical hydrogen generation from water using solar energy. Materials-related aspects. *International journal of hydrogen energy*. 2002;27(10):991-1022.

42. Leskela M, Salmi E, Ritala M. Atomic Layer Deposited Protective Layers. *Materials Science Forum*. 2017;879:1086-1092. doi:10.4028/www.scientific.net/MSF.879.1086

43. Ahonen M, Pessa M, Suntola T. A study of ZnTe films grown on glass substrates using an atomic layer evaporation method. *Thin Solid Films*. 1980;65(3):301-307.

44. Ahvenniemi E, Akbashev AR, Ali S, et al. Recommended reading list of early publications on atomic layer deposition—Outcome of the "Virtual Project on the History of ALD". *Journal of Vacuum Science & Technology A: Vacuum, Surfaces, and Films*. 2017;35(1):010801.

45. Suntola TS, Pakkala AJ, Lindfors SG. Apparatus for performing growth of compound thin films. Google Patents; 1983.

46. Aarik J, Aidla A, Kukli K, Uustare T. Deposition and etching of tantalum oxide films in atomic layer epitaxy process. *Journal of Crystal Growth*. 1994/11/01/ 1994;144(1):116-119. doi:https://doi.org/10.1016/0022-0248(94)90019-1

47. Kukli K, Aarik J, Aidla A, et al. Atomic Layer Deposition of Tantalum Oxide Thin Films from Iodide Precursor. *Chemistry of Materials*. 2001/01/01 2001;13(1):122-128. doi:10.1021/cm001086y

48. Tynell T, Karppinen M. Atomic layer deposition of ZnO: a review. *Semiconductor Science and Technology*. 2014;29(4):043001.

49. Puurunen RL. Surface chemistry of atomic layer deposition: A case study for the trimethylaluminum/water process. *Journal of applied physics*. 2005;97(12):9.

50. Groner MD, Fabreguette FH, Elam JW, George SM. Low-temperature Al2O3 atomic layer deposition. *Chemistry of materials*. 2004;16(4):639-645.

51. Ramos FJ, Maindron T, Béchu S, et al. Versatile perovskite solar cell encapsulation by low-temperature ALD-Al 2 O 3 with long-term stability improvement. *Sustainable Energy & Fuels*. 2018;2(11):2468-2479.

52. El-Atab N, Alqatari S, Oruc FB, et al. Diode behavior in ultra-thin low temperature ALD grown zinc-oxide on silicon. *AIP Advances*. 2013;3(10):102119.

53. Lin C, Tsai F-Y, Lee M-H, et al. Enhanced performance of dye-sensitized solar cells by an Al 2 O 3 charge-recombination barrier formed by low-temperature atomic layer deposition. *Journal of Materials Chemistry*. 2009;19(19):2999-3003.

54. Genevée P, Donsanti F, Renou G, Lincot D. Study of the aluminum doping of zinc oxide films prepared by atomic layer deposition at low temperature. *Applied surface science*. 2013;264:464-469.

55. Norman MA, Perez WL, Kline CC, Coridan RH. Enhanced Photoelectrochemical Energy Conversion in Ultrathin Film Photoanodes with Hierarchically Tailorable Mesoscale Structure. *Advanced Functional Materials*. 2018:1800481.

56. Wang C-Y. Comment on “A look at the multiphase mixture model for PEM fuel cell simulations”[Electrochem. Solid-State Lett., 11, B132 (2008)]. *Electrochem Solid-State Lett*. 2009;12(2)

57. Kosola A, Putkonen M, Johansson L-S, Niinistö L. Effect of annealing in processing of strontium titanate thin films by ALD. *Applied Surface Science*. 2003;211(1-4):102-112.

58. Vehkamäki M, Hatanpää T, Hänninen T, Ritala M, Leskelä M. Growth of SrTiO3 and BaTiO3 thin films by atomic layer deposition. *Electrochemical and Solid-state letters*. 1999;2(10):504.

59. Wang A, Chen T, Lu S, et al. Effects of doping and annealing on properties of ZnO films grown by atomic layer deposition. *Nanoscale research letters*. 2015;10(1):1-10.

60. Guillen C, Herrero J. Optical, electrical and structural characteristics of Al: ZnO thin films with various thicknesses deposited by DC sputtering at room temperature and annealed in air or vacuum. *Vacuum*. 2010;84(7):924-929.

61. Alnes ME, Monakhov E, Fjellvåg H, Nilsen O. Atomic layer deposition of copper oxide using copper (II) acetylacetonate and ozone. *Chemical Vapor Deposition*. 2012;18(4-6):173-178.

62. Iivonen T, Hämäläinen J, Marchand B, et al. Low-temperature atomic layer deposition of copper (II) oxide thin films. *Journal of Vacuum Science & Technology A: Vacuum, Surfaces, and Films*. 2016;34(1):01A109.

63. Avila JR, Kim DW, Rimoldi M, Farha OK, Hupp JT. Fabrication of thin films of α-Fe2O3 via atomic layer deposition using iron bisamidinate and water under mild growth conditions. *ACS applied materials & interfaces*. 2015;7(30):16138-16142.

64. Riha SC, DeVries Vermeer MJ, Pellin MJ, Hupp JT, Martinson ABF. Hematite-based photo-oxidation of water using transparent distributed current collectors. *ACS Applied Materials & Interfaces*. 2013;5(2):360-367.

65. Marichy C, Silva RM, Pinna N, Willinger M, Donato N, Neri G. Non-Aqueous Atomic Layer Deposition of SnO2 for Gas Sensing Application. *ECS Transactions*. 2018;86(6):55.

66. Heo J, Hock AS, Gordon RG. Low temperature atomic layer deposition of tin oxide. *Chemistry of Materials*. 2010;22(17):4964-4973.

67. Warner EJ. Atomic Layer Deposition of Tin Oxide and Zinc Tin Oxide: Understanding the Reactions of Alkyl Metal Precursors with Ozone. 2014;

68. Farmer DB, Copel M, Todorov T, et al. Atomic Layer Deposition of Tungsten Oxide Using Nitrogen Dioxide: A Comparative Study with Other Oxygen Sources. *Chemistry of Materials*. 2021;33(7):2267-2273.

69. Liu R, Lin Y, Chou LY, et al. Water splitting by tungsten oxide prepared by atomic layer deposition and decorated with an oxygen-evolving catalyst. *Angewandte Chemie International Edition*. 2011;50(2):499-502.

70. Nandi DK, Sarkar SK. Atomic layer deposition of tungsten oxide for solar cell application. *Energy Procedia*. 2014;54:782-788.

71. Kozodaev MG, Romanov RI, Chernikova AG, Markeev AM. Atomic Layer Deposition of Ultrathin Tungsten Oxide Films from WH2 (Cp) 2 and Ozone. *The Journal of Physical Chemistry C*. 2021;125(39):21663-21669.

72. Diskus M, Nilsen O, Fjellvåg H. Thin films of cobalt oxide deposited on high aspect ratio supports by atomic layer deposition. *Chemical Vapor Deposition*. 2011;17(4-6):135-140.

73. Kim J, Iivonen T, Hamalainen J, et al. Low-temperature atomic layer deposition of cobalt oxide as an effective catalyst for photoelectrochemical water-splitting devices. *Chemistry of Materials*. 2017;29(14):5796-5805.

74. Huang B, Cao K, Liu X, Qian L, Shan B, Chen R. Tuning the morphology and composition of ultrathin cobalt oxide films via atomic layer deposition. *RSC Advances*. 2015;5(88):71816-71823.

75. Weimer MS, Kim IS, Guo P, Schaller RD, Martinson ABF, Hock AS. Oxidation state discrimination in the atomic layer deposition of vanadium oxides. *Chemistry of Materials*. 2017;29(15):6238-6244.

76. Musschoot J, Deduytsche D, Van Meirhaeghe RL, Detavernier C. ALD of vanadium oxide. *ECS Transactions*. 2009;25(4):29.

77. Blanquart T, Niinistö J, Gavagnin M, et al. Atomic layer deposition and characterization of vanadium oxide thin films. *RSC advances*. 2013;3(4):1179-1185.

78. Badot JC, Ribes S, Yousfi EB, et al. Atomic layer epitaxy of vanadium oxide thin films and electrochemical behavior in presence of lithium ions. *Electrochemical and Solid-State Letters*. 2000;3(10):485-488.

79. Zhou Y, King DM, Liang X, Li J, Weimer AW. Optimal preparation of Pt/TiO2 photocatalysts using atomic layer deposition. *Applied Catalysis B: Environmental*. 2010;101(1-2):54-60.

80. Christensen ST, Elam JW, Lee B, Feng Z, Bedzyk MJ, Hersam MC. Nanoscale structure and morphology of atomic layer deposition platinum on SrTiO3 (001). *Chemistry of Materials*. 2009;21(3):516-521.

81. Goulas A, Van Ommen JR. Atomic layer deposition of platinum clusters on titania nanoparticles at atmospheric pressure. *Journal of Materials Chemistry A*. 2013;1(15):4647-4650.

82. Forster M, Potter RJ, Yang Y, Li Y, Cowan AJ. Stable Ta2O5 overlayers on hematite for enhanced photoelectrochemical water splitting efficiencies. *ChemPhotoChem*. 2018;2(3):183-189.

83. Scheuermann AG, Prange JD, Gunji M, Chidsey CED, McIntyre PC. Effects of catalyst material and atomic layer deposited TiO 2 oxide thickness on the water oxidation performance of metal–insulator–silicon anodes. *Energy & Environmental Science*. 2013;6(8):2487-2496.

84. Paracchino A, Laporte V, Sivula K, Grätzel M, Thimsen E. Highly active oxide photocathode for photoelectrochemical water reduction. *Nature materials*. 2011;10(6):456-461.

85. Paracchino A, Mathews N, Hisatomi T, Stefik M, Tilley SD, Grätzel M. Ultrathin films on copper (I) oxide water splitting photocathodes: a study on performance and stability. *Energy & Environmental Science*. 2012;5(9):8673-8681.

86. Zhang Y, Seghete D, Abdulagatov A, et al. Investigation of the defect density in ultra-thin Al2O3 films grown using atomic layer deposition. *Surface and Coatings Technology*. 2011/02/15/ 2011;205(10):3334-3339. doi:https://doi.org/10.1016/j.surfcoat.2010.12.001

87. Gertsch JC, Sortino E, Bright VM, George SM. Deposit and etchback approach for ultrathin Al2O3 films with low pinhole density using atomic layer deposition and atomic layer etching. *Journal of Vacuum Science & Technology A: Vacuum, Surfaces, and Films*. 2021;39(6):062602.

88. Buabthong P, Ifkovits ZP, Kempler PA, et al. Failure modes of protection layers produced by atomic layer deposition of amorphous TiO 2 on GaAs anodes. *Energy & Environmental Science*. 2020;13(11):4269-4279.

89. Gordon RG. Criteria for choosing transparent conductors 25 MR BULLETIN. August; 2000.

90. Ginley DS, Bright C. Transparent conducting oxides. *MRS bulletin*. 2000;25(8):15-18.

91. Ellmer K. Past achievements and future challenges in the development of optically transparent electrodes. *Nature Photonics*. 2012/12/01 2012;6(12):809-817. doi:10.1038/nphoton.2012.282

92. Lee Y, Sun H, Young MJ, George SM. Atomic layer deposition of metal fluorides using HF–pyridine as the fluorine precursor. *Chemistry of Materials*. 2016;28(7):2022-2032.

93. Hu S, Lewis NS, Ager JW, Yang J, McKone JR, Strandwitz NC. Thin-film materials for the protection of semiconducting photoelectrodes in solar-fuel generators. *The Journal of Physical Chemistry C*. 2015;119(43):24201-24228.

94. Chen YW, Prange JD, Dühnen S, et al. Atomic layer-deposited tunnel oxide stabilizes silicon photoanodes for water oxidation. *Nature materials*. 2011;10(7):539-544.

95. Strandwitz NC, Comstock DJ, Grimm RL, Nichols-Nielander AC, Elam J, Lewis NS. Photoelectrochemical behavior of n-type Si (100) electrodes coated with thin films of manganese oxide grown by atomic layer deposition. *The Journal of Physical Chemistry C*. 2013;117(10):4931-4936.

96. Hu S, Shaner MR, Beardslee JA, Lichterman M, Brunschwig BS, Lewis NS. Amorphous TiO2 coatings stabilize Si, GaAs, and GaP photoanodes for efficient water oxidation. *Science*. 2014;344(6187):1005-1009.

97. McDowell MT, Lichterman MF, Spurgeon JM, et al. Improved stability of polycrystalline bismuth vanadate photoanodes by use of dual-layer thin TiO2/Ni coatings. *The Journal of Physical Chemistry C*. 2014;118(34):19618-19624.

98. McDowell MT, Lichterman MF, Carim AI, et al. The influence of structure and processing on the behavior of TiO2 protective layers for stabilization of n-Si/TiO2/Ni photoanodes for water oxidation. *ACS applied materials & interfaces*. 2015;7(28):15189-15199.

99. Choi MJ, Jung J-Y, Park M-J, Song J-W, Lee J-H, Bang JH. Long-term durable silicon photocathode protected by a thin Al 2 O 3/SiO x layer for photoelectrochemical hydrogen evolution. *Journal of Materials Chemistry A*. 2014;2(9):2928-2933.

100. Fan R, Dong W, Fang L, et al. Stable and efficient multi-crystalline n+ p silicon photocathode for H2 production with pyramid-like surface nanostructure and thin Al2O3 protective layer. *Applied Physics Letters*. 2015;106(1):013902.

101. Correa GC, Bao B, Strandwitz NC. Chemical stability of titania and alumina thin films formed by atomic layer deposition. *ACS applied materials & interfaces*. 2015;7(27):14816-14821.

102. Li C, Wang T, Luo Z, Zhang D, Gong J. Transparent ALD-grown Ta 2 O 5 protective layer for highly stable ZnO photoelectrode in solar water splitting. *Chemical communications*. 2015;51(34):7290-7293.

103. Moehl T, Suh J, Sévery L, Wick-Joliat R, Tilley SD. Investigation of (Leaky) ALD TiO2 Protection Layers for Water-Splitting Photoelectrodes. *ACS applied materials & interfaces*. 2017;9(50):43614-43622.

104. Siddiqi G, Luo Z, Xie Y, et al. Stable water oxidation in acid using manganese-modified TiO2 protective coatings. *ACS applied materials & interfaces*. 2018;10(22):18805-18815.

105. Penner RM. Mesoscopic metal particles and wires by electrodeposition. *The Journal of Physical Chemistry B*. 2002;106(13):3339-3353.

106. Dasgupta NP, Neubert S, Lee W, Trejo O, Lee J-R, Prinz FB. Atomic layer deposition of Al-doped ZnO films: effect of grain orientation on conductivity. *Chemistry of Materials*. 2010;22(16):4769-4775.

107. Guziewicz E, Godlewski M, Wachnicki L, et al. ALD grown zinc oxide with controllable electrical properties. *Semiconductor Science and Technology*. 2012;27(7):074011.

108. Moulder JF. Handbook of X-ray photoelectron spectroscopy. *Physical electronics*. 1995:230-232.

109. Sheng W, Gasteiger HA, Shao-Horn Y. Hydrogen oxidation and evolution reaction kinetics on platinum: acid vs alkaline electrolytes. *Journal of The Electrochemical Society*. 2010;157(11):B1529.

110. Lehmann V. *Electrochemistry of silicon: instrumentation, science, materials and applications*. 2002.

111. Kavan L, Tétreault N, Moehl T, Grätzel M. Electrochemical characterization of TiO2 blocking layers for dye-sensitized solar cells. *The Journal of Physical Chemistry C*. 2014;118(30):16408-16418.

112. Sun K, Saadi FH, Lichterman MF, et al. Stable solar-driven oxidation of water by semiconducting photoanodes protected by transparent catalytic nickel oxide films. *Proceedings of the National Academy of Sciences*. 2015;112(12):3612-3617.

113. Sun K, McDowell MT, Nielander AC, et al. Stable solar-driven water oxidation to O2 (g) by Ni-oxide-coated silicon photoanodes. *The journal of physical chemistry letters*. 2015;6(4):592-598.

114. Coridan RH, Nielander AC, Francis SA, et al. Methods for comparing the performance of energy-conversion systems for use in solar fuels and solar electricity generation. *Energy & Environmental Science*. 2015;8(10):2886-2901.

115. Wu Y, Giddings AD, Verheijen MA, et al. Dopant distribution in atomic layer deposited ZnO: Al films visualized by transmission electron microscopy and atom probe tomography. *Chemistry of Materials*. 2018;30(4):1209-1217.

116. Pourbaix M. Atlas of electrochemical equilibria in aqueous solution. *NACE*. 1974;307

117. Xiang C, Weber AZ, Ardo S, et al. Modeling, simulation, and implementation of solar-driven water-splitting devices. *Angewandte Chemie International Edition*. 2016;55(42):12974-12988.

118. Yang Y, Xu D, Wu Q, Diao P. Cu2O/CuO bilayered composite as a high-efficiency photocathode for photoelectrochemical hydrogen evolution reaction. *Scientific reports*. 2016;6(1):1-13.

119. Siavash Moakhar R, Hosseini-Hosseinabad SM, Masudy-Panah S, et al. Photoelectrochemical Water-Splitting Using CuO-Based Electrodes for Hydrogen Production: A Review. *Advanced Materials*. 2021;33(33):2007285.

120. Huang Q, Kang F, Liu H, Li Q, Xiao X. Highly aligned Cu 2 O/CuO/TiO 2 core/shell nanowire arrays as photocathodes for water photoelectrolysis. *Journal of Materials Chemistry A*. 2013;1(7):2418-2425.

121. Zhang Q, Zhang K, Xu D, et al. CuO nanostructures: synthesis, characterization, growth mechanisms, fundamental properties, and applications. *Progress in Materials Science*. 2014;60:208-337.

122. Wadia C, Alivisatos AP, Kammen DM. Materials availability expands the opportunity for large-scale photovoltaics deployment. *Environmental science & technology*. 2009;43(6):2072-2077.

123. Xing H, Lei E, Guo Z, Zhao D, Li X, Liu Z. Exposing the photocorrosion mechanism and control strategies of a CuO photocathode. *Inorganic Chemistry Frontiers*. 2019;6(9):2488-2499.

124. Shaislamov U, Kim H, Yang JM, Yang BL. CuO/ZnO/TiO2 photocathodes for a self-sustaining photocell: Efficient solar energy conversion without external bias and under visible light. *International Journal of Hydrogen Energy*. 2020;45(11):6148-6158.

125. Li Y, Luo K. Flexible cupric oxide photocathode with enhanced stability for renewable hydrogen energy production from solar water splitting. *RSC advances*. 2019;9(15):8350-8354.

126. Tomita R, Pu Z, Kamegawa T, Anpo M, Higashimoto S. Photoelectrochemical properties of copper oxide (CuO) influenced by work functions of conductive electrodes. *Research on Chemical Intermediates*. 2019;45(12):5947-5958.

127. Amrullah A, Gunawan G, Prasetya NBA. The Effect of Cu Ohmic Contact on Photoelectrochemical Property of S-CuO Thin Film Photocathodes. *Jurnal Kimia Sains dan Aplikasi*. 22(6):255-262.

128. Ng KH, Kadir HA, Minggu LJ, Kassim MB. Stability of WO3/CuO heterojunction photoelectrodes in PEC system. Trans Tech Publ; 219-224.

129. Shaislamov U, Krishnamoorthy K, Kim SJ, et al. Highly stable hierarchical p-CuO/ZnO nanorod/nanobranch photoelectrode for efficient solar energy conversion. *international journal of hydrogen energy*. 2016;41(4):2253-2262.

130. Ha J-w, Ryu H, Lee W-J, Bae J-S. Efficient photoelectrochemical water splitting using CuO nanorod/Al2O3 heterostructure photoelectrodes with different Al layer thicknesses. *Physica B: Condensed Matter*. 2017;519:95-101.

131. Turrión M, Bisquert J, Salvador P. Flatband potential of F: SnO2 in a TiO2 dye-sensitized solar cell: an interference reflection study. *The Journal of Physical Chemistry B*. 2003;107(35):9397-9403.

132. Baker BG, Johnson BB, Maire GLC. Photoelectric work function measurements on nickel crystals and films. *Surface Science*. 1971;24(2):572-586.

133. Michaelson HB. The work function of the elements and its periodicity. *Journal of applied physics*. 1977;48(11):4729-4733.

134. Wang Y, Lany S, Ghanbaja J, et al. Electronic structures of C u 2 O, C u 4 O 3, and CuO: A joint experimental and theoretical study. *Physical Review B*. 2016;94(24):245418.

135. Koffyberg FP, Benko FA. A photoelectrochemical determination of the position of the conduction and valence band edges of p-type CuO. *Journal of Applied Physics*. 1982;53(2):1173-1177.

136. Golden TD, Shumsky MG, Zhou Y, VanderWerf RA, Van Leeuwen RA, Switzer JA. Electrochemical deposition of copper (I) oxide films. *Chemistry of Materials*. 1996;8(10):2499-2504.

137. Lowe JM, Yan Q, Benamara M, Coridan RH. Direct photolithographic patterning of cuprous oxide thin films via photoelectrodeposition. *Journal of Materials Chemistry A*. 2017;5(41):21765-21772.

138. Lowe JM, Coridan RH. Mechanistic control of a galvanic replacement reaction on cuprous oxide. *Nanoscale Advances*. 2019;1(4):1343-1350.

139. Reed PJ, Mehrabi H, Schichtl ZG, Coridan RH. Enhanced Electrochemical Stability of TiO2-Protected, Al-doped ZnO Transparent Conducting Oxide Synthesized by Atomic Layer Deposition. *ACS applied materials & interfaces*. 2018;10(50):43691-43698.

140. Liu H, Favier F, Ng K, Zach MP, Penner RM. Size-selective electrodeposition of meso-scale metal particles: a general method. *Electrochimica Acta*. 2001;47(5):671-677.

141. Xing H, E L, Guo Z, Zhao D, Liu Z. Enhancement in the charge transport and photocorrosion stability of CuO photocathode: The synergistic effect of spatially separated dual-cocatalysts and p-n heterojunction. *Chemical Engineering Journal*. 2020/08/15/ 2020;394:124907. doi:https://doi.org/10.1016/j.cej.2020.124907

142. Toe CY, Zheng Z, Wu H, Scott J, Amal R, Ng YH. Photocorrosion of Cuprous Oxide in Hydrogen Production: Rationalising Self-Oxidation or Self-Reduction. *Angewandte Chemie International Edition*. 2018-10-08 2018;57(41):13613-13617. doi:10.1002/anie.201807647

143. Zhang X, Luo Y, Lu K, Lu Q, Gong J, Liu R. Tuning Band Gaps and Photoelectrochemical Properties of Electrodeposited CuO Films by Annealing in Different Atmospheres. *Journal of The Electrochemical Society*. 2020;167(2):026504.

144. Nakaoka K, Ueyama J, Ogura K. Electrochemical/Chemical Deposition and Etching-Photoelectrochemical Behavior of Electrodeposited CuO and Cu2O Thin Films on Conducting Substrates. *Journal of the Electrochemical Society*. 2004;151(10):C661.

145. Wang Y, Jiang T, Meng D, et al. Fabrication of nanostructured CuO films by electrodeposition and their photocatalytic properties. *Applied Surface Science*. 2014/10/30/ 2014;317:414-421. doi:https://doi.org/10.1016/j.apsusc.2014.08.144

146. Chang T-H, Hsu C-Y, Lin H-C, Chang KH, Li Y-Y. Formation of urchin-like CuO structure through thermal oxidation and its field-emission lighting application. *Journal of Alloys and Compounds*. 2015/09/25/ 2015;644:324-333. doi:https://doi.org/10.1016/j.jallcom.2015.04.107

147. Toupin J, Strubb H, Kressman S, Artero V, Krins N, Laberty-Robert C. CuO photoelectrodes synthesized by the sol–gel method for water splitting. *Journal of Sol-Gel Science and Technology*. 2019/01/01 2019;89(1):255-263. doi:10.1007/s10971-018-4896-3

148. Masudy-Panah S, Siavash Moakhar R, Chua CS, et al. Nanocrystal Engineering of Sputter-Grown CuO Photocathode for Visible-Light-Driven Electrochemical Water Splitting. *ACS Applied Materials & Interfaces*. 2016/01/20 2016;8(2):1206-1213. doi:10.1021/acsami.5b09613

149. Masudy-Panah S, Moakhar RS, Chua CS, Kushwaha A, Wong TI, Dalapati GK. Rapid thermal annealing assisted stability and efficiency enhancement in a sputter deposited CuO photocathode. 10.1039/C6RA03383K. *RSC Advances*. 2016;6(35):29383-29390. doi:10.1039/C6RA03383K

150. Kushwaha A, Moakhar RS, Goh GKL, Dalapati GK. Morphologically tailored CuO photocathode using aqueous solution technique for enhanced visible light driven water

splitting. *Journal of Photochemistry and Photobiology A: Chemistry*. 2017/03/15/ 2017;337:54-61. doi:https://doi.org/10.1016/j.jphotochem.2017.01.014

151. Cots A, Bonete P, Gómez R. Improving the Stability and Efficiency of CuO Photocathodes for Solar Hydrogen Production through Modification with Iron. *ACS Applied Materials & Interfaces*. 2018/08/08 2018;10(31):26348-26356. doi:10.1021/acsami.8b09892

152. Gaulding EA, Liu G, Chen CT, et al. Fabrication and optical characterization of polystyrene opal templates for the synthesis of scalable, nanoporous (photo) electrocatalytic materials by electrodeposition. *Journal of Materials Chemistry A*. 2017;5(23):11601-11614.

153. Masudy-Panah S, Siavash Moakhar R, Chua CS, Kushwaha A, Dalapati GK. Stable and efficient CuO based photocathode through oxygen-rich composition and Au–Pd nanostructure incorporation for solar-hydrogen production. *ACS Applied Materials & Interfaces*. 2017;9(33):27596-27606.

154. Chauhan D, Satsangi VR, Dass S, Shrivastav R. Preparation and characterization of nanostructured CuO thin films for photoelectrochemical splitting of water. *Bulletin of Materials Science*. 2006;29(7)

155. Chen JT, Zhang F, Wang J, et al. CuO nanowires synthesized by thermal oxidation route. *Journal of Alloys and Compounds*. 2008/04/24/ 2008;454(1):268-273. doi:https://doi.org/10.1016/j.jallcom.2006.12.032

156. Verma M, Kumar V, Katoch A. Sputtering based synthesis of CuO nanoparticles and their structural, thermal and optical studies. *Materials Science in Semiconductor Processing*. 2018/03/15/ 2018;76:55-60. doi:https://doi.org/10.1016/j.mssp.2017.12.018

157. Li J, Jin X, Li R, et al. Copper oxide nanowires for efficient photoelectrochemical water splitting. *Applied Catalysis B: Environmental*. 2019/01/01/ 2019;240:1-8. doi:https://doi.org/10.1016/j.apcatb.2018.08.070

158. Masudy-Panah S, Radhakrishnan K, Tan HR, Yi R, Wong TI, Dalapati GK. Titanium doped cupric oxide for photovoltaic application. *Solar Energy Materials and Solar Cells*. 2015;140:266-274.

159. Yersak AS, Lee Y-C. Probabilistic distributions of pinhole defects in atomic layer deposited films on polymeric substrates. *Journal of Vacuum Science & Technology A: Vacuum, Surfaces, and Films*. 2016;34(1):01A149.

160. Uluc AV, Mol JMC, Terryn H, Böttger AJ. Hydrogen sorption and desorption related properties of Pd-alloys determined by cyclic voltammetry. *Journal of Electroanalytical Chemistry*. 2014/11/15/ 2014;734:53-60. doi:https://doi.org/10.1016/j.jelechem.2014.09.021

161. Zhan D, Velmurugan J, Mirkin MV. Adsorption/Desorption of Hydrogen on Pt Nanoelectrodes: Evidence of Surface Diffusion and Spillover. *Journal of the American Chemical Society*. 2009/10/21 2009;131(41):14756-14760. doi:10.1021/ja902876v

162. Wang A, Chen T, Lu S, et al. Effects of doping and annealing on properties of ZnO films grown by atomic layer deposition. *Nanoscale research letters*. 2015;10(1):75.

Appendix

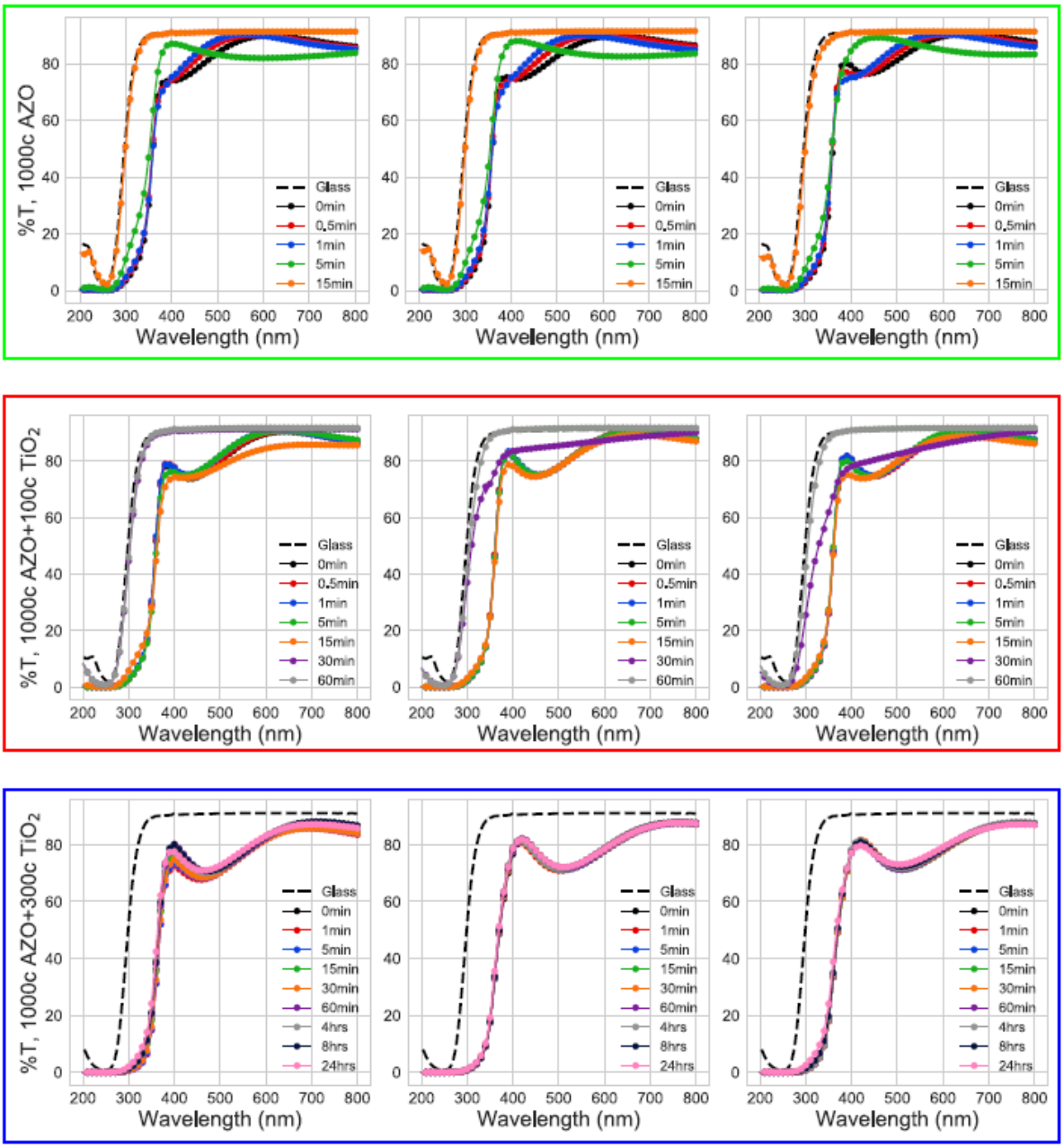

Figure A.1 - Series of transmission UV-Vis measurements for identical (top) 1000c AZO films, (middle) 1000c AZO+100c TiO_2 films, and (bottom) 1000c AZO+300 TiO_2 films exposed to 1 M NaOH, performed in triplicate. The data is shown to communicate the reproducibility of the experiments shown in Chapter 3

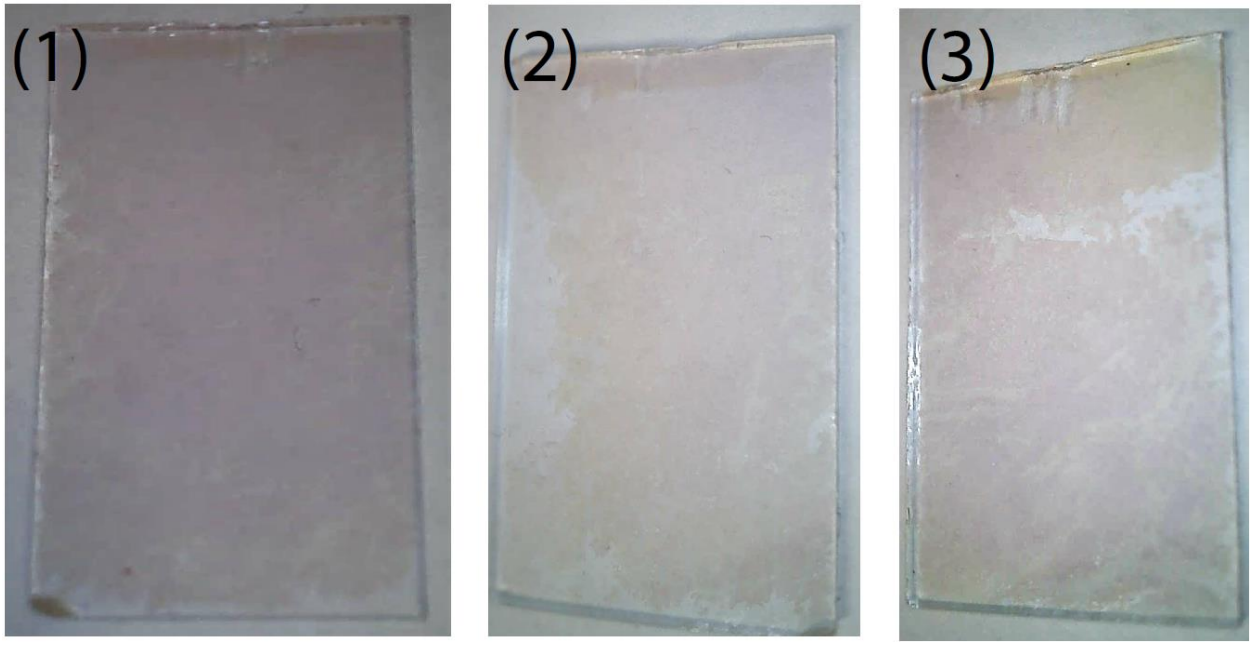

Figure A.2 - 1000c AZO+300c TiO_2 substrates after a 24-hour exposure to 1 M NaOH. The visible etching of the films appears to occur from the edges, where the alkaline conditions can potentially etch the glass substrate from under the ALD-deposited film as the mode of failure. In spite of the visible etching, a majority of the ALD-deposited film persisted after 24 hours.

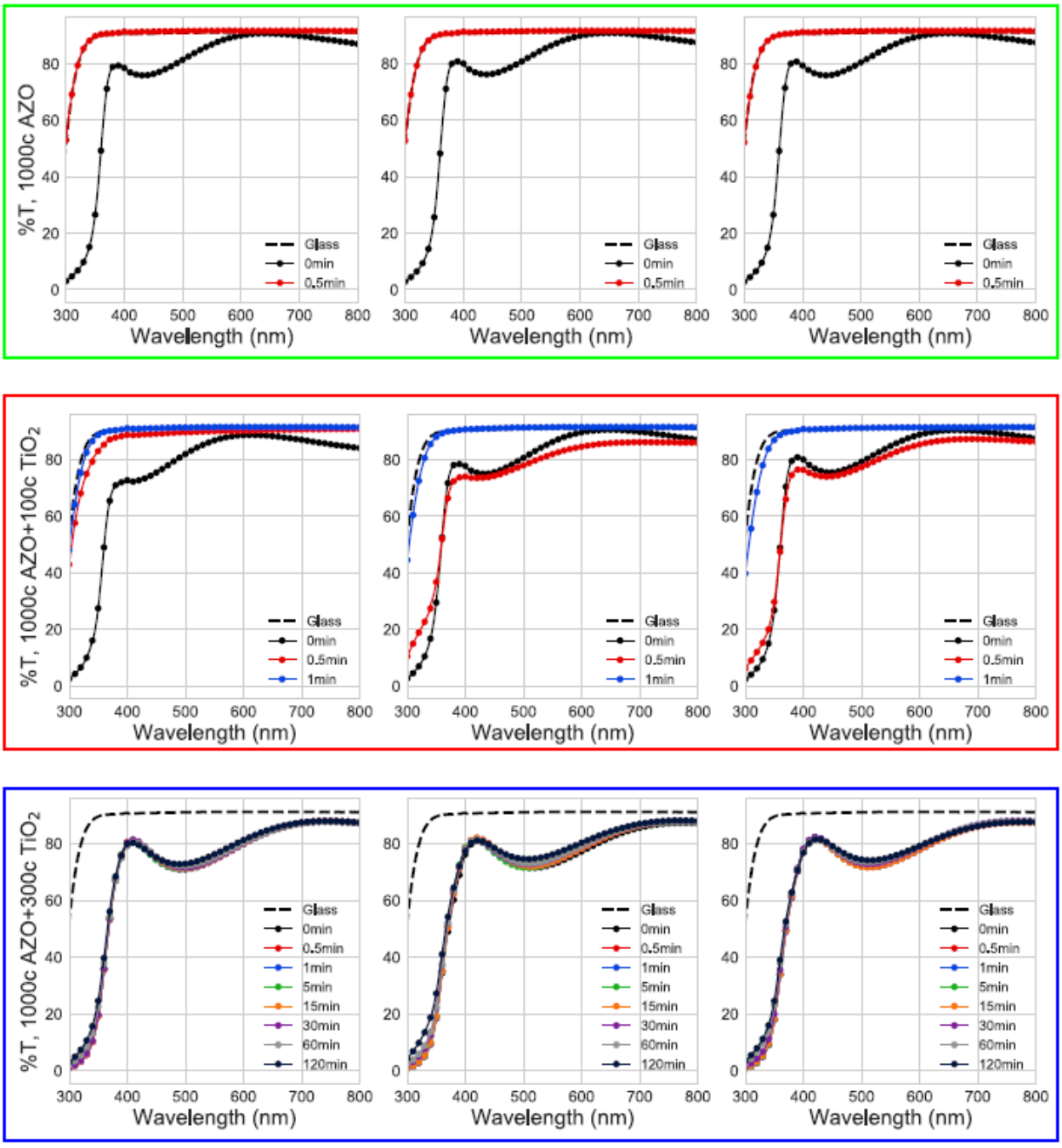

Figure A.3 - Series of transmission UV-Vis measurements for identical (top) 1000c AZO films, (middle) 1000c AZO+100c TiO_2 films, and (bottom) 1000c AZO+300 TiO_2 films exposed to 1 N H_2SO_4, performed in triplicate. The data is shown to communicate the reproducibility of the experiments shown in Chapter 3.